Supported by
Spain Water
and IWHR, China

IAHR
2017

37th IAHR
WORLD CONGRESS
13-18 August, 2017
Kuala Lumpur, Malaysia

ESTUARIES AND SHORE PROTECTION

SIMPLIFIED MODEL TO ESTIMATE IMPACT ON COASTAL WATER RESOURCES AND LOSS OF SHORE LINE LAND DUE TO CLIMATE CHANGE AND SEA LEVEL RISE

ABI OGUNIMILUSI A (1) & GREGORY DE COSTA (2)

(1, 2) Unitec Institute of Technology, New Zealand
rdecosta@unitec.ac.nz

ABSTRACT

This paper presents a review of past to current observations in the study of climate change and sea-level rise. It appraised the relationship between climate change and sea-level rise, and other drivers of the climate system and factors contributing to sea-level rise. It also highlights the various impacts of climate change and sea-level rise which helps in suggesting short to long term strategies for effective coastal management. A model is developed to provide an estimation of present sea-level rise invariably indicating how much land is lost and how much effect it will have on the water table and rivers especially in coastal areas where there is no data available. To obtain these estimates, numerical modelling is carried out using parameters selected during the study. These parameters with the help of a conversion table produced initial data which are then applied to available Wellington region data for scenarios of 0.5m, 1.0m and 1.5m sea-level rise. Model testing is carried out to measure loss of land and effect of on water table, and satisfactory results are obtained and presented here in. This model hopes to aid the decision making process of what adaptation methods can be employed or to implement in certain coastal areas.

KeyWords: Climate change; sea level rise; land loss.

1 INTRODUCTION

It is evident that climate change and sea level change is occurring globally (Bell et al, 2001 & Chen et. al, 2012) and that this threatens coastal habitats round the world. While in some instances, resources such as finance, knowledge, data and skill is available, in most instances we lack one or many of these elements as a vital criterion for accurate forecast and prediction of sea level change and its impact on water resources as well as land surface. The situation at Wellington was analysed and its impact assessed (Tonkin and Taylor, 2013). However as there are many instances and locations where data, software or skill is unavailable and in such instances it is yet required to be simulated, forecasted and predicted in order to mitigate and manage coastal zones subjected to sea level change impacts. Thus, a simplified composite model is needed.

It must be noted here that as mentioned in the title this is a simplified model and hence a simple, easy to use and understand model to estimate some values in instances where there is no data and no scientific skills and technology to use.

1.1 Research gap being addressed

Currently unless there is sufficient data for a given location, it is not possible to arrive at even an estimated value for loss of land / shore line due to climate change. The simplified model developed in this project will provide information on loss of land coupled with effect on water table and rivers especially where data is scarce or unavailable. Its development adopts two approaches, one being a conceptual approach while the other is a mathematical approach. This paper presents the conceptual approach.

The conceptual approach consists of parameters chosen at random to create a hierarchy of events within the climate system. It will provide estimates of how much land will be lost and how much effect climate change and sea-level rise will have on the water table using scenarios of 0.5m, 1.0m, and 1.5m of sea level rise. The model achieved satisfactory results in comparison tests carried out, although it is based on only a few parameters and some assumptions. It hopes to shed some more light onto the climate change phenomenon and help in decision making process of choosing well suited adaptation methods even in situations when data is sparse. (Robert, 2011)

The mathematical approach method proposed to estimate the changes occurring in these areas, initially sea level changes is done using linear regression method. Changes to land and water table in Wellington New Zealand are simulated, modelled and a simple model is developed thereafter using this data to estimate changes. The model is validated using a different data set series. This model could now be used to easily estimate the changes to ground water and land loss in other coastal zones, particularly where data is sparse and technical knowhow on modelling is limited, which is generally the case in most areas.

/ ISSN 1562-6865 (Online) - ISSN 1063-7710 (Print)

2 THE CONCEPTUAL APPROACH MODEL DESIGN

For the purpose of this work, some climate change elements had been highlighted for consideration and Figure 1 provides a visual of these components. (Church et. al, 2001, and Shindell, 2007) Changes in these elements or parameters have an important part to play in the cycle of events resulting in sea-level rise and the apparent loss of land. Variations in these parameters will determine the effect of climate change and sea-level rise on the water table, rivers, land and ultimately was described as the relationship between climate change and sea-level rise for a particular area.

The pyramid in figure also shows the series of events that occurred with climate change residing at the top. As described in literature, climate change resulted in temperature increase while also increasing oceanic temperature causing thermal expansion and altering rainfall patterns to bring about sea-level rise. The pyramid had been derived upon considering all variables that come into play in a climate change scenario. The numbers chosen were derived giving equal weightage across all variables in the horizontal plane.

Sea-level rise on the other hand were affected by local parameters such as local topography, hydrological patterns, storm patterns, localized global average temperature effects and tectonic movements or subsidence. This will result to affect water table, loss of land and effect on rivers.

2.1 Effect on water table

Sea-level rise will affect the local water table by increasing its height, by causing an intrusion of salt water into groundwater and the intensity of these effect will depend on factors such as the nature of the coastal bedrock material, seasonal dryness and tidal changes, hydrological and soil characteristics as shown in Figure 2. Numbers have been assigned to these factors from 1 to 5 based on respective impacts. (Claire, 2015).

2.2 Effect on Loss of land

Sea-level rise will result in loss of land and amount of land lost will also depend on local parameters such as local topography, hydrological patterns and storm patterns with loss of land in relation to the pyramid in Figure 1 and 2. Ultimately it was caused by secondary factors such as flooding, shoreline retreat, and increase in tide levels, inundation of low and wetlands, and effect on land drainage. Numbers have also been assigned to these factors in figure, from 1 to 5 based on respective impacts, (Small, 2003).

2.3 Effect on rivers

Sea-level rise affects rivers by causing an intrusion of salt water into river networks disrupting river ecosystems and flow patterns. (Dragoni et. al, 2008). As shown in Figure 1, this was also a result of secondary factors such as flooding, shoreline retreat, inundation of low and wetlands, and effect on land drainage. Numbers have also been assigned to these factors in Fig 2, from 1 to 5 based on respective impacts.

2.4 Parameterization of conceptual model

One of the objectives of this project was to obtain an estimate of the effect of sea level rise on land and water resources. For the purpose of this model, the following assumptions have been made:

- 90% conversion for all parameters.
- Values were assigned to parameters from a rating scale of 0 -100 or 0-1000 as listed in Table 1.

As shown in Table 1, each parameter has been assigned to a level relative to their position in the pyramid as earlier described in figure. As the cycle of events occurs down the pyramid from one level to the other, there was a conversion rate of 90% and in levels where there were two or more parameters such as in levels 3 and 4. The conversion factor was split evenly among the residing parameters.

2.5 Conversion table

Numerical estimates of resulting effects have been obtained using a conversion table which provides equivalents for each parameter and their respective units of measure. Figure. 2 provided a side-by-side view of the pyramid and a sample conversion table showing relevant parameters.

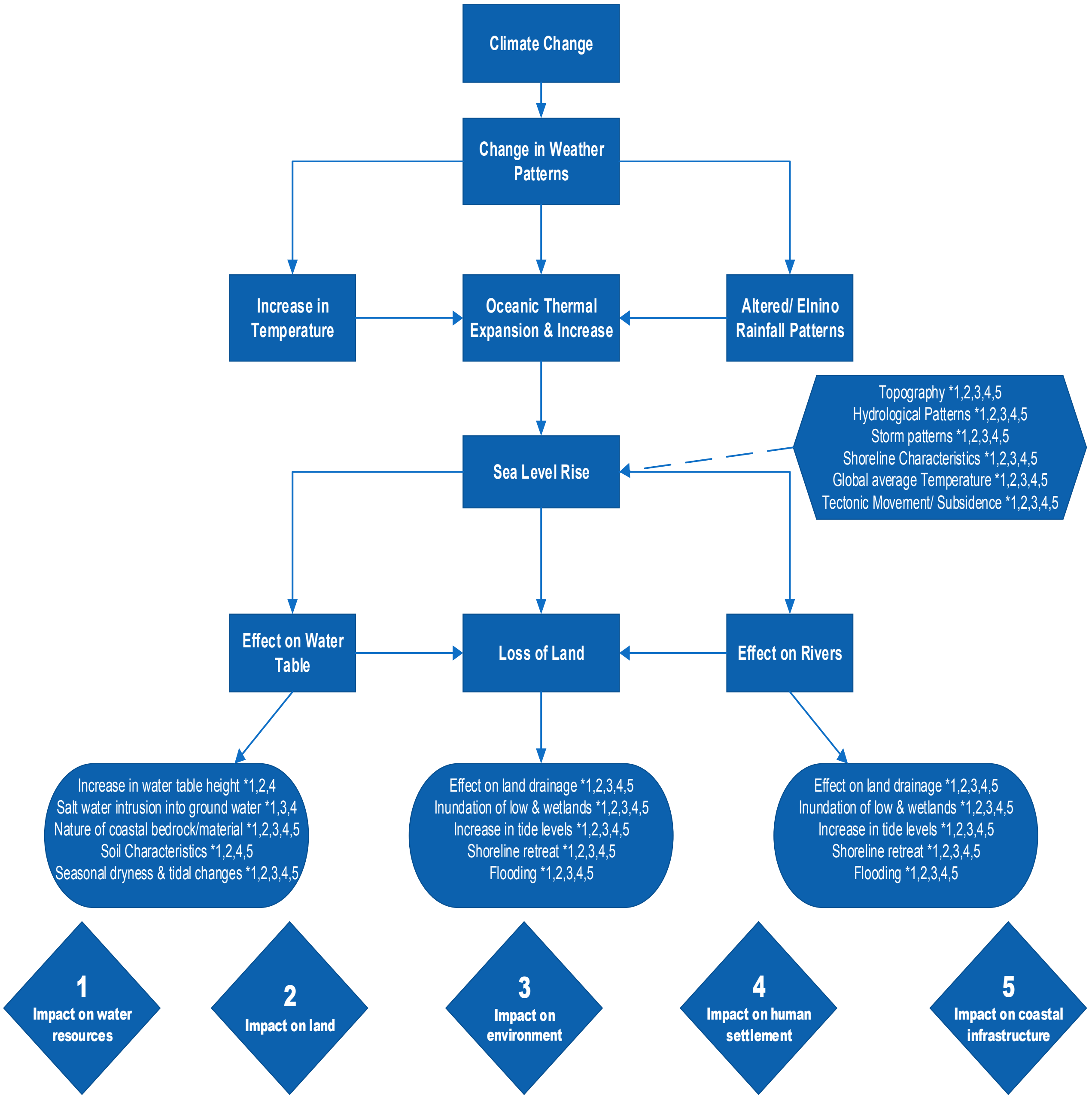

Figure 1. Simplified model showing some components of climate change and sea level rise.

Table 1. Parameters rating scale.

Level	Parameter	Rating
1	Climate Change	0-100
2	Change in Weather Patterns	0-100
3	Increase in Temperature	0-100
3	Oceanic thermal expansion & increase	0-100
3	Altered/Elnino Rainfall Patterns	0-100
4	Sea Level Rise	0-1000
5	Effect on water table	0-1000
5	Loss of land	0-1000
5	Effect on Rivers	0-1000

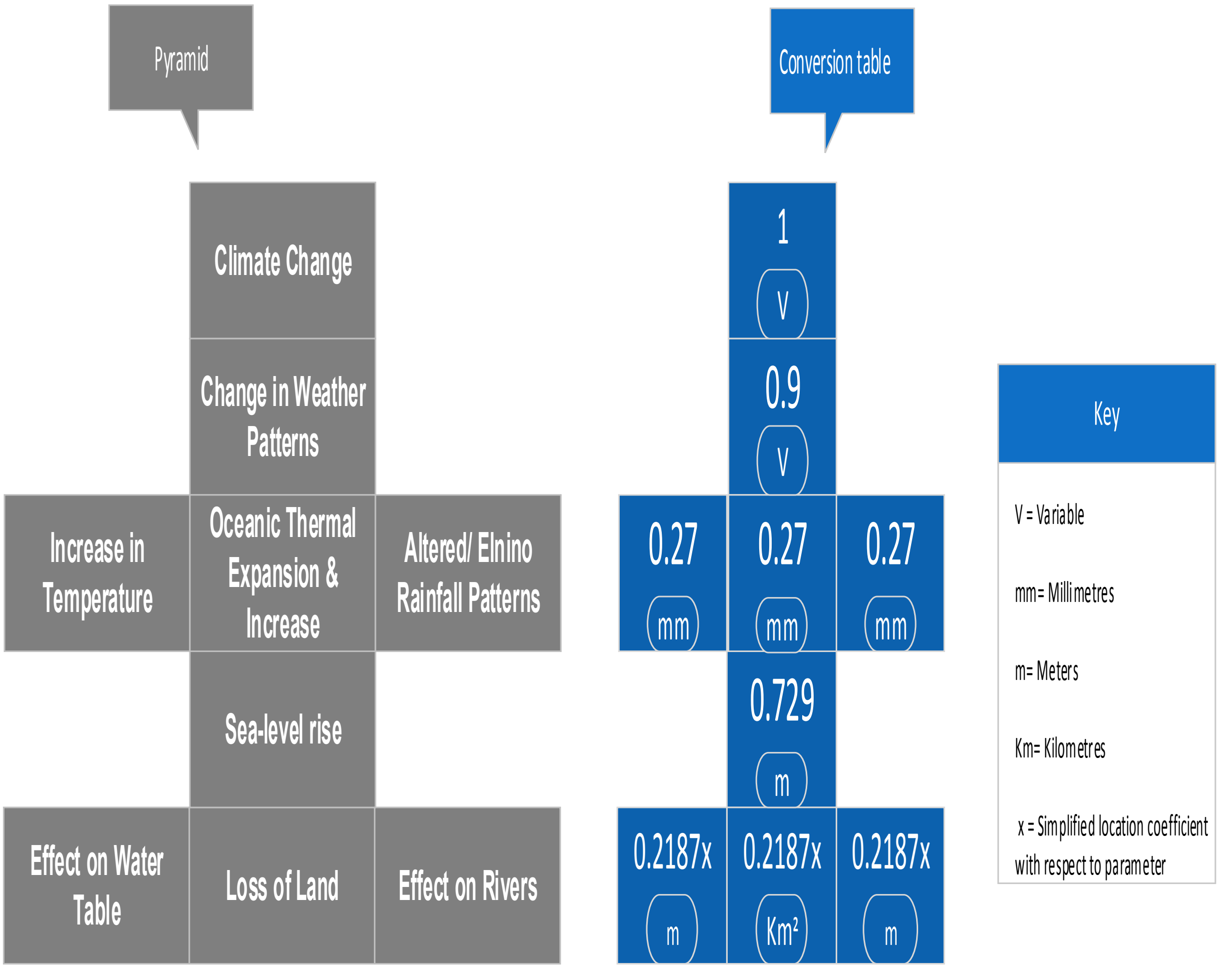

Figure 2. Climate change pyramid and sample conversion table showing relevant parameters.

From the conversion table, Figure 3, a climate change effect rating of 1 (one) on a scale of 1-100 will result in an equivalent land loss of approximately 200cm. At level 1, climate change will produce a 'change in weather patterns' effect of 0.9 at level 2 which also then converts at 90% to 0.81 split equally among the level 3 parameters (Increase in temperature, oceanic thermal expansion & increase, and altered/el-nino rainfall patterns) at 0.27 each.

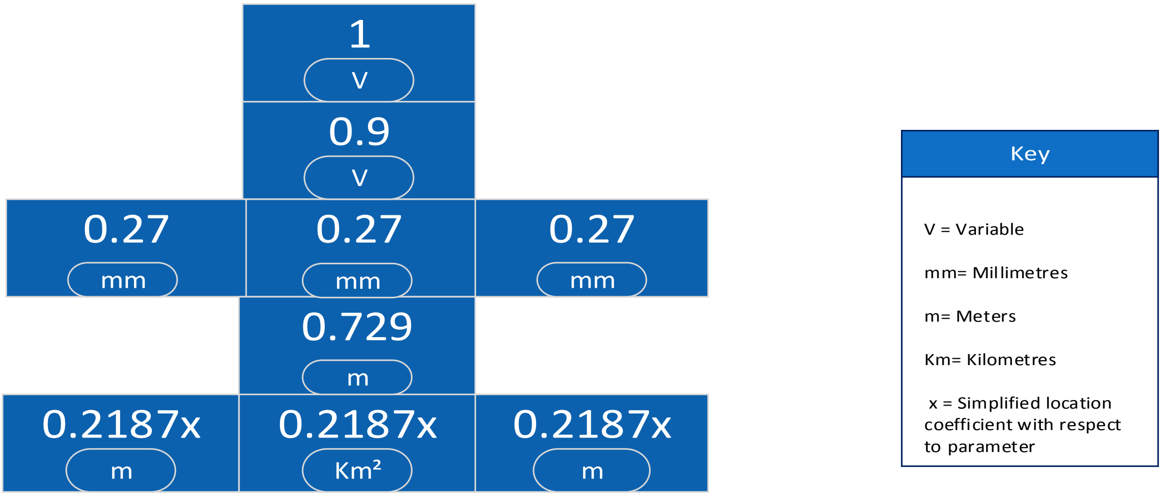

Figure 3. A conversion table showing values obtained from a climate change effect rating of 1.

The sum of estimates obtained for level 3 parameters (0.81) was then converted to 90% to produce a sea-level rise of 0.729 which also converts to 90% of cause of the effects at level 5. The intensity or scale of the parameters at level 5 (effect on water table, loss of land & effect on rivers) will be subsequently determined by a multiple of x, which was the location coefficient with respect to the parameter.

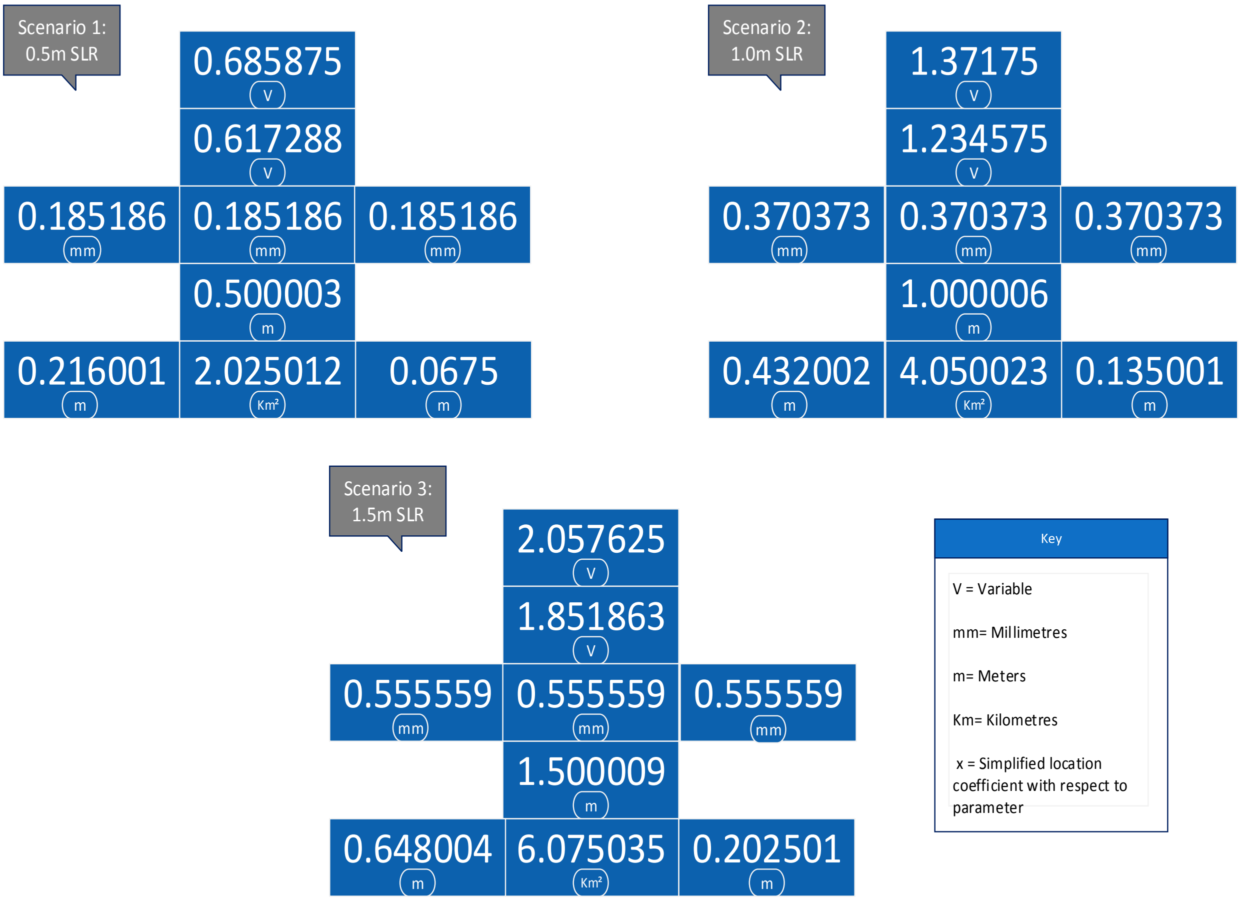

Figure 4. Conversion tables with results obtained from scenarios 1, 2 & 3 of 0.5m, 1.0m, & 1.5m SLR.

2.6 Model testing & results

Using data from Wellington and considering scenarios 1, 2 & 3 of 0.5m, 1.0m & 1.5m sea-level rise with no storm effects, land loss in Km² was calculated for all 3 (three) scenarios as shown in Figure 4.

Considering scenario 1 of 0.5m sea-level rise, climate change occurred at a rate of 0.68 on a scale of 0-100, resulting in an equivalent land loss of 2.02km². Scenario 2 of 1.0m sea-level rise resulted from climate change at a rate of 1.37 on a scale of 0-100, affecting 4.05km² of land while scenario 3 of 1.5m sea-level rise occurred due to climate change at a rate of 2.05 on a scale of 0-100 thereby causing land loss of 6.07km².

Scenario	SLR (m)		Wellington	Model
1	0.5	Loss of land (Km²)	1.14	2.02
2	1.0		4.18	4.05
3	1.5		6.95	6.07
1	0.5	Effect on water table	0.00 - 0.17	0.21
2	1.0		0.39 - 0.61	0.43
3	1.5		0.76 - 0.98	0.65

Figure 5. Comparison of Wellington & Model data.

The summary statistics used were comparative to the data from forecast in Wellington. Figure 5 provides a comparison chart for values obtained from Wellington and those obtained from the model. With a close look at the values for loss of land, we can tell that model values seemed to be within reasonable tolerance of the estimated values for Wellington. Although model estimate (loss of land) for scenario 1 (2.02Km²) is somewhat higher than its equivalent to Wellington value (1.14Km²), adaptation measures provided against the model value will definitely address both estimates but maybe at a slightly higher cost.

Effect on water table (in meters) was also calculated using Wellington values for scenarios 1, 2 & 3 of 0.5m, 1.0m & 1.5m sea-level rise and the results (see table) also showed that model values to be within reasonable tolerance of the estimated values for Wellington. Model values obtained for scenarios 1, 2 & 3 of 0.5m, 1.0m & 1.5m sea-level rise were: 0.21m, 0.43m and 0.65m respectively.

3 DISCUSSION

The simplified model designed, described the theory of climate change resulting in an increase in global temperature thereby giving rise to an increase in sea level. It also shows how sea-level rise coupled with a few other parameters cause loss of land in coastal areas as well as effect on rivers and water table.

A conversion table was also developed to calculate the value for land lost due to climate change and sea-level rise. The model is tested with values obtained from the Wellington region for scenarios 1, 2 and 3 of 0.5m, 1.0m and 1.5m sea-level rise and these provided satisfactory results in comparison with the Wellington data.

Estimates are obtained for loss of land but a few key points are noted during model development which were the assumptions made, such as conversion at 90%, and the assignment of units to parameters. These may in some way affect the reliability or integrity of the model as there are also limitations with regards to parameters, especially when only a few are considered. As stated by Nicholls (2011), thermal expansion accounted for about 25% of the observed SLR since 1960 and about 50% from 1993 to 2003. However, with this model, thermal expansion is the major player accounting for sea-level rise to a large extent. Other dynamic factors or changing coastal processes like changes in inundation area and duration are also not taken into account.

Effect on water table (in meters) is also calculated using Wellington values for scenarios 1, 2 & 3 of 0.5m, 1.0m & 1.5m sea-level rise and the results (see table) also show model values to be within reasonable tolerance of the estimated values for Wellington. Model values obtained. The value for 1, 2 & 3 of 0.5m, 1.0m & 1.5m sea-level rise are: 0.21m, 0.43m and 0.65m respectively.

Predicting sea-level rise impacts as a result of climate change is complex, and simple models are mostly of limited use. However, the simplified conceptual model designed in this project produced satisfactory results in comparison with available data and will help in the decision making process of what adaptation methods to employ or implement in certain coastal areas. Although models like these are based on assumptions of the impact of climate change and a few parameters, they shed some light onto the climate change phenomenon, bringing it to the forefront and encouraging coastal authorities to take necessary action.

REFERENCES

Bell, R.G., Hume, T.M. & Hicks, D.M. (2001). *Planning for Climate Change Effects on Coastal Margins,* A Report Prepared for the Ministry for the Environment as Part of the New Zealand Climate Change Programme. Ministry for the Environment.

Chen, C.C., McCarl, B. & Chang, C.C. (2012). Climate Change, Sea Level Rise and Rice: Global Market Implications. *Climatic Change*, 110(3-4), 543-560.

Church, J.A. (2001). *Changes in Sea Level, Climate Change 2001: The Scientific Basis,* Contribution of Working Group I to the Third Assessment Report of the Intergovernmental Panel.

Claire Marshall, (2015). Global Flood Toll to Triple by 2030, BBC Science & Environment. http://www.bbc.co.uk/news/science-environment-31738394

Dragoni, W. & Sukhija, B.S. (2008). *Climate Change and Groundwater: A Short Review.* Geological Society, London, Special Publications, 288(1), 1-12.

Nicholls, R.J. (2011). Planning for the Impact of Sea-Level Rise. *Oceanography*, 24(2), 144.

Robert, J. Nicholls et al, (2011). Sea-Level Rise and its Possible Impacts Given a 'Beyond 4◦C World' in the Twenty-First Century. *Philosophical Transactions of Royal Society of London A,* 369, 161-181.

Shindell, D. (2007). Estimating the Potential for Twenty-First Century Climate Change, Philosophical Transactions of Royal Society of London A 2675-2694 http://rsta.royalsocietypublishing.org/content/roypta/365/1860/2675.full.pdf

Small, C. & Nicholls, R.J. (2003). A Global Analysis of Human Settlement in Coastal Zones. *Journal of Coastal Research,* 19(3), 584–599.

Tonkin & Taylor Ltd, (2013). Report prepared for Wellington City Council: Sea Level Rise Options Analysis, June 2013. http://wellington.govt.nz/~/media/services/environment-and-waste/environment/files/61579-wcc-sea-level-rise-options.pdf

Proceedings of the 37th IAHR World Congress
August 13 – 18, 2017, Kuala Lumpur, Malaysia

PHYSICAL HYDRAULIC MODELLING FOR THE DEVELOPMENT OF INNOVATIVE COASTAL PROTECTION STRUCTURE IN A 2-D WAVE FLUME

AHMAD HADI MOHAMED RASHIDI(1), MOHAMAD HIDAYAT JAMAL(2), MOHD RADZI ABD HAMID(3) &
SITI SALIHAH MOHD SENDEK(4)

(1,3,4) Research Centre for Coastal and Oceanography, National Hydraulic Research Institute of Malaysia,
Ministry of Natural Resources and Environment, Selangor, Malaysia,
(1,2) Faculty of Civil Engineering & Centre for Coastal and Ocean Engineering,
Universiti Teknologi Malaysia, Johor, Malaysia,
ahmadhadi@nahrim.gov.my; mhidayat@utm.my; radzi@nahrim.gov.my; sitisalihah@nahrim.gov.my

ABSTRACT

NEXC Block is an innovative shore protection structure which is designed to protect the coast from severe erosion during monsoon season. While on a calmer period, the system encourages sediment accumulation thus expands the beach naturally. NEXC Block is placed within Mean Higher High Water and Highest Astronomical Tide water level with sufficient toe protection for stability and efficiency, ensuring minimum adverse impact to existing coastal hydrodynamic. This paper aims to present the development process of NEXC Block in 2-D wave flume facility, where site measurement works are conducted for data validation and monitoring. Model dimension and hydrodynamic parameters are geometrically downscaled to 1:20. Two slope gradient values are used representing actual beach profiles at selected sites. Cohesive-form sediment size is 100µm. Three water levels; Mean Lower Low Water, Mean Sea Level and Mean Higher High Water with two significant wave height values H_s (irregular waves) are used for experiments. Beach profile is measured both before and after each experiment for erosion-accretion and stability analysis. Experiments on exposed beach without structure is also carried out as reference profile. The experiments show that NEXC Block model structure installed with ample toe protection is a fairly stable coastal protection structure. The structure is able to withstand strong wave impact during monsoon where no significant structural movement was detected. However, scouring is prevalent at the toe of structure at unprotected structures. Some parts of NEXC Block and toe protection are exposed during monsoon season but less sediment is found eroded as compared to exposed unprotected beach in maintaining beach stability. Moreover, during a longer calm period, the sediments are found to return back to the beach hence nourishing and expanding the beach naturally.

Keywords: Shore protection; coastal hydraulic; physical model; beach erosion; natural beach accretion.

1 INTRODUCTION

Main function of mostly available coastal protection structures is solely to protect the shoreline from erosion. Some structures such as groin and offshore breakwater are more effective as those systems encourage sediment accumulation at leeside. However, the installations of such systems are very costly and interferes with natural beach hydrodynamic processes. Wave breaking zone and the direction of longshore drift are directly affected hence creating adverse effects such as erosion to the other side of installation. Interference in this dynamic equilibrium leads to a change in sediment supply causing an increase or decrease in local sediment budget, resulting in accretion or erosion, respectively (Ghazali, 2006). In addition, the reflected wave energy back to offshore may cause beach profile changes due to resonant effects (US Army Engineers, 1984).

Seawall type of coastal protection can be considered as shoreline defense applications. Seawall is defined as an armored revetment and an embankment with or without structural crest elements (Allsop, 1986). The protection wall is usually built parallel to the shoreline in order to prevent soil from sliding while offering protection from wave impact (Kamphuis, 2000). The construction material includes concrete, rocks, steel, timber, rubber tyres, and sandbags (Pilkey and Dixon, 1996). The shapes of coastal structures are determined by the use of the structure and generally can be categorised as vertical or nearly vertical, sloping, convex-curved, concave-curve, reentrant, or stepped. Shoreline defense structures, such as seawall and coastal blocks are situated beyond active hydrodynamic zone hence minimising adverse implication towards natural processes.

The aim of this study is to develop an innovative coastal block protection structure with minimum impact to existing coastal hydrodynamic processes. NEXC Block is designed and placed within Mean Higher High Water (MHHW) and Highest Astronomical Tide (HAT) water level to minimize the impact, and installed with sufficient toe protection for stability and efficiency. It protects the beach and acts as a wave breaker during monsoon season, while the system also encourages natural sediment accumulation on calmer period. NEXC Block, or NAHRIM Coastal Erosion Protection and Beach Expansion Block was developed by National

Hydraulic Research Institute of Malaysia in 2015 – 2016. This applied research approach includes conducting research and development using experimental testing and pilot projects at selected sites.

Main objectives of 2D wave flume study include:

a) To determine the ability of NEXC Block as a protection structure against coastal erosion,
b) To assess the efficiency of NEXC Block as a coastal expansion mechanism in laboratory scale,
c) To evaluate and verify the interaction between structures – water level – wave – sediment processes with NEXC Block site installations.

2 PROJECT SITES

Two locations were selected for the proposed NEXC Block pilot project development. The choices of sites were based on the differential exposures towards seasonal monsoon, morphological changes, hydrodynamic impacts and local socio-economic activities. Site A is located in Pantai Batu Lima, Port Dickson, Negeri Sembilan, within Regency Hotel compound which was at present severely eroded. The site is a sandy beach facing Malacca Strait, where wave impact is dominant during Southwest Monsoon (April – July). The bay is a popular attraction for tourism and water sport activities throughout the year.

Whereas Site B is situated at the east coast of Peninsular Malaysia, facing South China Sea. The shoreline is exposed to heavier wave impact during Northeast monsoon (November – February). The sandy beach of Pantai Rhu Muda, Marang, Terengganu is a traditional village community where fishing and small scale fishing related-industry are the main socio-economic activities. The straight coasts off Marang is usually exposed and severely eroded during monsoon but eventually returned to stable state and are naturally nourished during calmer period.

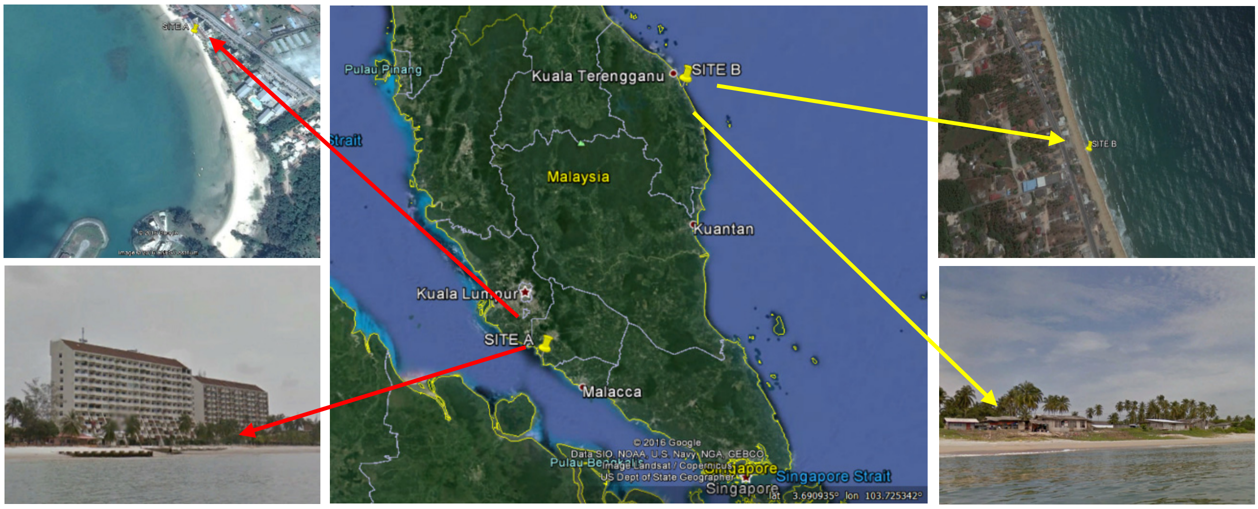

a) Site A: Port Dickson, Negeri Sembilan b) Site B: Marang, Terengganu

Figure 1. Site locations in Negeri Sembilan and Terengganu, Malaysia.

Primary hydraulic data collection works had been conducted at both locations. Water level was measured with reference to the nearest tidal station at each site. Current and wave data were measured at 10m water depth using two ADCP units, approximately 3km from shoreline for a minimum 15 days. Bathymetry survey was done within 3km x 3km area, including sediment sea floor sampling and water quality monitoring. Beach profiling was done on monthly basis within few days after full moon event. Secondary historical wave and wind information were gathered from UKMO database. GIS survey was also conducted to verify existing physical, socio-economy and natural ecosystem at the selected sites. The data and information gathered are later analyzed and used for numerical and experimental studies.

3 EXPERIMENTAL SETUP

Physical tests were conducted using a 50m - 2D wave flume facility located at Hydraulic and Instrumentation Lab, National Hydraulic Research Institute of Malaysia (NAHRIM). Model structure dimension and hydrodynamic parameters were geometrically downscaled to 1:20. Mildly sloping shore 1:15 and steep slope 1:3 were used in representing the actual beach profiles at selected sites. Cohesive-form sediment size is 100µm. Three water levels; Mean Lower Low Water (MLLW) 0.9m, Mean Sea Level (MSL) 1.0m and Mean Higher High Water (MHHW) 1.1m with two significant wave height values H_s (irregular waves) 0.1m and 0.2m were used for experiments. During the study, model structure was placed at a fix location along the flume, approximately at the center of interest study area i.e. in active erosion / accretion zone. Beach profile was measured in the area of interest of 2.5m x 1.5m both before and after each experiment for erosion-accretion and stability analysis. Experiment run-time was 60 minutes referring to the duration of specific water level in each tide cycle. Experiments on empty unprotected beach without structure were also carried out as reference profile. Wave height and period was calibrated both manually and automatically using 3 units of wave probe located along the flume.

a) NEXC Block experiments with slope 1:15 @ WL 0.9m, HS 0.1m

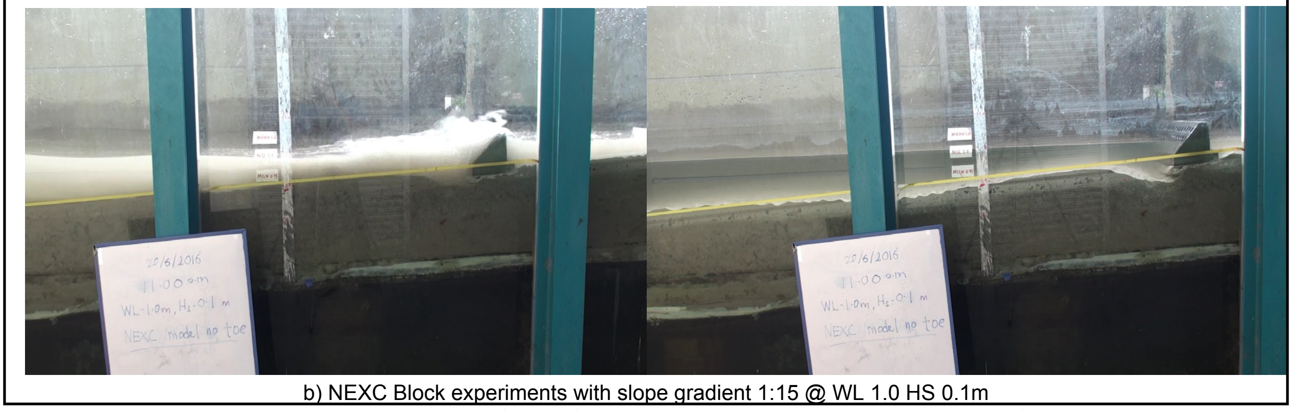

b) NEXC Block experiments with slope gradient 1:15 @ WL 1.0 HS 0.1m

Figure 2. Experimental work in 2D wave flume facility; structure toe aligned to Mean Sea Level water mark.

Interaction between waves and waves-structures due to variation of water levels and wave heights were studied and recorded. The scope of experiments works is simplified as below:

a. Study on beach profile changes on accretion or erosion due to wave actions and sea levels on an exposed / unprotected beach (No Structure) as a control,
b. Study on beach profile changes on accretion or erosion due to wave actions and sea levels with NEXC Block coastal protection structure model.

In flume, the interest study area was marked as 0cm – 250cm with 10cm interval in Y direction (length of flume). Whilst, in X direction the profile was marked from 0cm to 150cm (breadth of flume). Data sample for the first 30cm from both side of walls in the flume was ignored and considered as unstable due to wave reflection effect. A datum or reference point was fixed at the top corner of flume wall. The distance between datum and beach surface was remarked as height in Z-axis at specific points. NEXC Block system was placed at fixed condition along coordinate 0 – 150, 90 – 120 with single layer installation. In this study, the toe of NEXC Block structure was aligned to Mean Sea Level water mark; 1.0m. Beach profile was measured manually each time before and after experiments to compare the differences, associated to erosion or accretion. In this paper, all erosion level was measured at the central of wave flume (x-axis) along the beach profile (y-axis) which was at a cross-section of 70, 30 – 160 (x, y). Figure 2 showed the experimental work conducted in wave flume with various hydrodynamic parameters on a stiff and mild slopes environment. Experiments equilibrium was set at 60 minutes for each case.

→ NEXC Block Model Structure

For the purpose of the study, NEXC Block model structure was geometrically downscaled to 1:10. The dimension of the structure is 12cm in height, 12cm in length and was arranged along the 150cm of flume width as shown in Figure 2. In the experiment, the model was made of reinforced concrete with design face slope of 45°. NEXC Block had two main functions, firstly was to protect the beach from erosion. During high tide and heavy wave impact, erosion is controlled to occur only at the front of installation whereas at the backside, or leeside is fully protected. The uniqueness of the product is for its second function; where it also encourages beach expansion via natural sediments accumulation during calmer period.

The block is designed with hollow slanting cone shape on the surface as in Figure 6. These holes reduce wave impact as it hits the structure along the shoreline. On normal condition, this feature allows water and sediments to pass through the structure during flood tide. However, during ebb tide, water will flow back to the sea but leaving sediments to be trapped at leeside. The process continues over beach cycle period where the beach will be expanded naturally due to sediment accumulation both at front and leeside of the structure installation.

→ Stability of coastal block as a coastal protection structure

The proposed coastal block aims to function as a natural solution to beach erosion and re-nourishment. Based on simple conservative economics, the structure can be used on either semi-permanent to permanent basis, as a contingent on the scope of the re-nourishment project. Coastal blocks work in two ways; firstly, by breaking down the wave energy, therefore lessening erosion impact to the shore. Secondly, it encourages beach expansion or natural nourishment by permitting sea water which contains sediment and sand to pass through the tapered hole. During ebb flow, sediments were trapped behind the structure and were unable to return to the sea. Over the time especially during a calm period, sediments would be accumulated hence expanding the beach naturally. Hence the design of coastal block must be sufficiently stable against overturning and sliding failures. The calculation of wave forces on coastal block was according to EM 1110-2-1100 (Part VI), Goda formula for irregular waves (Goda, 1974; Tanimoto et al., 1976) was used.

Overturning failure is rotation of wall about its toe due to exceeding of moment caused. This is due to overturning forces and resisting forces. Eq. [1] show the factor of safety against overturning and is given by:

$$F_0 = \frac{\sum M_R}{\sum M_0} > 1.5 \qquad [1]$$

where,

$\sum M_R$ = sum of resisting moment about toe
$\sum M_0$ = sum of overturning moment about toe

The factor of safety sliding may be expressed by Eq. [2], where generally a minimum factor of safety of 1.5 is required:

$$FS = \frac{\sum R_V \tan\delta + kc_2B}{\sum R_H} \qquad [2]$$

where,

$\sum R_V$ = sum of the vertical resisting forces
$\sum R_H$ = sum of the horizontal resisting forces
δ = angle of friction between the soil and base slab$k$ = the range between 1/3 to 2/3
c = cohesion of soil$R$ = resistance force B = bottom length of structure

Table 1. Overturning check on coastal block structure at point 0.

Option	Ɵ	Moment at 0		$\frac{\sum M+}{\sum M-}$	Remark
		ΣM+ (kNm)	ΣM- (kNm)		
1	30°	58.2	18.88	3.1	Ok
2	45°	18.1	7.58	2.4	Ok
3	60°	8.74	7.64	1.14	No (redesign 3a)
3a	60°	14.71	7.64	1.9	Ok

Table 2. Sliding check on coastal block structure at point 0.

Angle (°)	ΣR$_V$ (kN)	ΣR$_H$ (kN)	B (m)	FS	Remark
30	68	18.45	1.85	3.7	Ok
45	40.2	15.36	1.2	2.8	Ok
60	31.75	12.34	1.05	2.9	Ok

The result of analysis is given as above. Table 1 showed the moment of acting on coastal block for stability analysis on overturning check. The factor of safety for overturning is more than 1.5. The force of acting on coastal block for stability analysis on sliding check is summarized as shown in Table 2. The stability of coastal block is analyzed using full scale data collected from site and secondary data was used where necessary.

The structure was exposed to both forces from the wave action and lateral earth action specifically active earth pressure. As the block moves away from the backfill, there was a decrease in the pressure on the wall. The decrease continues until a minimum value was reached after which there was no reduction in the pressure and the value will become constant. Coastal block must be designed to withhold wave actions in order to maintain its stability against overturning and sliding failures. Vertical distribution of pressure due to wave force acting on sea block was measured based on wave velocity and state (peak or trough) and water level (Hanbin GU et al., 2003).

4 DISCUSSION ON LABORATORY DATA SAMPLING AND ANALYSIS

Figure 3 depicted the beach profiling on erosion-accretion analysis of selected experiments. No structure experiments as presented in Figure 3a shows that erosion occurred along the unprotected beach. Higher water level led to erosion farther landward. Higher wave magnitude caused greater erosion level or scarp height. Combination of high water and large wave magnitude caused catastrophic impact; total sand loss along the exposed shore.

Rate of erosion is quicker and higher at a steeper slope and higher water levels, until it reaches equilibrium. Data and information from these experiments is used as control and reference to the experiments with proposed coastal structure. Figure 3b illustrated the erosion-accretion profile after experiments with NEXC Block are completed. It is found that with NEXC Block installation, erosion was controlled to occur only at the face of the structure, thus the backside of system is protected. Erosion generally occurred at all water level scenarios MLLW, MSL and MHHW with H_s 0.2m. The protected beach at the backside of installation was found safe with the installation of NEXC Block. The system was also found stable against overturning and sliding failures.

It is also found that lower water level with lower wave magnitude encouraged sediment accumulation at the structure face. This was found in experiment with MLLW at 0.9m and H_s 0.1m. In a longer calm period or outside monsoon season, the accumulation process is repeated until the sediments are returned to the beach and trapped behind the structure installation, resulting in a natural beach nourishment.

Even though erosion was controlled to occur only at the face of the structure, this has led to scouring problem at the toe of structure. Scour was found to be maximum when water level is at the structure face level; within wave breaking zone. Wave impact on structure caused wave overtopping and sediment deposition near structure toe. Higher water level which submerged the structure minimized the impact of toe scouring. However due to higher water level reaching farther landward, it left the area unprotected hence erosion is found more landward. Nevertheless, the structure managed to block and control the sediment from moving farther seaward from land.

The experiments were also expanded by introducing scour protection which was installed at the toe structure to prevent structural failure. From Figure 3c, the analysis showed that sufficient toe protection had increased the stability of NEXC Block installation. Scour at toe structure can be minimized and naturally transferred at the bottom of the scour protector units. Scour protection units can be installed further seaward beyond breaking zone hence minimizing the impact of scour problem. However, an increase in overtopping was expected with this type of installation due to the increase of height breaker. Based on the study, it was also found that steeper beach (slope 1:3) is more vulnerable to erosion as compared to mild 1:15 slope. Erosion depth at similar water level and wave height increased almost double for steeper beach.

Hollow slanting cone shape design at NEXC Block is the main feature that allows sea water to penetrate through structure during flood and ebb flows. Suspended sediments from offshore were carried by water and wave, then penetrated the structure via hollow sections and trapped behind the installation as the water flows back out. Hollow sections on the structure must be designed less than 50% of surface area to ensure optimum sediment entrapment. The design was also able to distribute wave energy evenly during high tide, reducing overtopping and scouring impact.

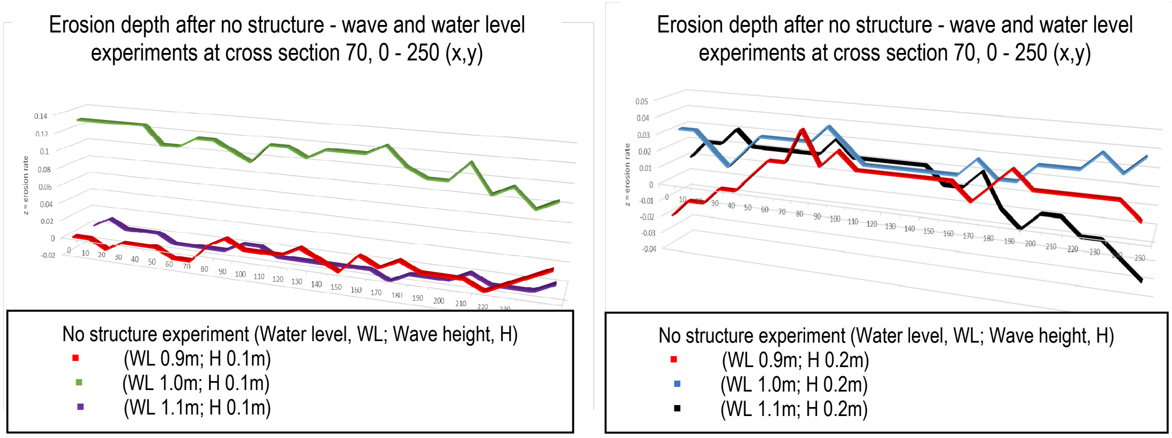

a) Beach profiles at unprotected shores after experiments completed (control)

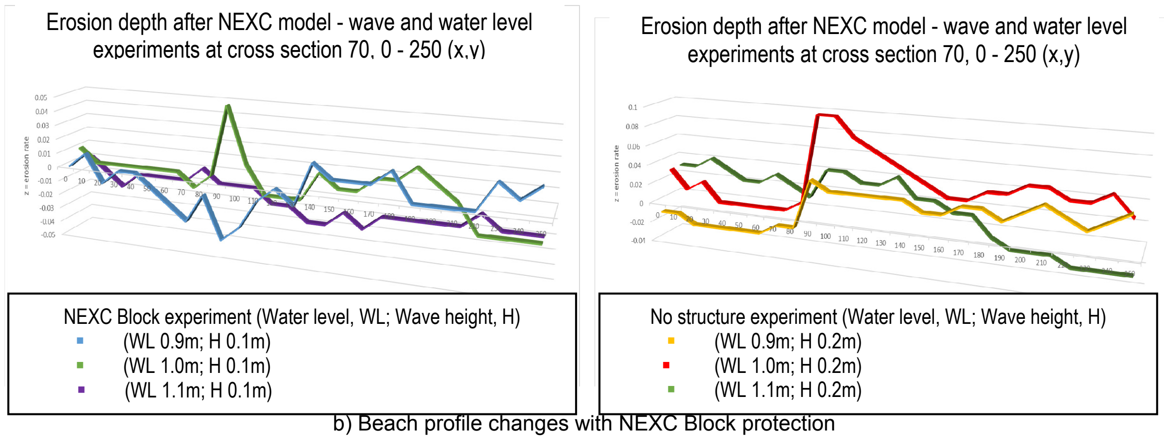

b) Beach profile changes with NEXC Block protection

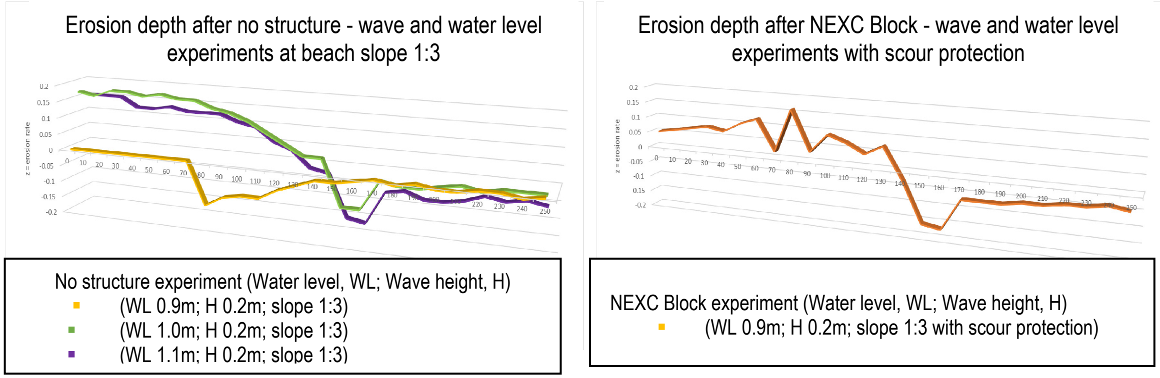

c) Beach profiles with NEXC Block plus scour protection

Figure 3. Analysis of erosion-accretion after experiments completed.
(Y-axis refers to distance of marked beach profile along flume, Z-axis refers to erosion depth).

5 ON SITE MEASUREMENT

Data collection works and beach profile measurement at sites are shown in Figure 4a. The measurements were generally done on monthly basis to monitor continuous beach profile changes throughout the beach cycle period in one year calendar. Measurement was done automatically using Real Time Kinetic device, however in case of no signal or connectivity issues, auto level was used. In Port Dickson, NEXC Block system was installed within the Mean Sea Level to Mean High Higher Water marks. Changes in beach profile in front of the structure were greatly influenced by the high tide event every month. Riprap stone as scour protection as in Figure 4a is normally exposed during full moon and high tide events but the toe area is usually recovered during neap tide. The process is relatively typical for each tidal cycle.

a) Beach profiling at Marang Beach b) Natural beach nourished after monsoon

Figure 4. Beach profile measurement at sites.

However, in Marang Beach, Terengganu the shore is designed to only be exposed to extreme event during northeast monsoon season. The installation of NEXC Block, located within Mean High Higher Water to Highest Astronomical Tide marks was found fairly successful in controlling and limiting the erosion at the face of the installation, whereas the backside area was protected. During northeast monsoon, the beach started to erode and scour impact can be seen as in Figure 4a. However, NEXC Block has managed to block most of back sedimenting from reaching further seaward. The accumulation of sediment at the back of the structure has increase the stability of the system and at the same time expanding the beach naturally. Note that strong toe protection was important in providing ample protection against beach scour. Coastal vegetation was also found to start recovering and regrow as in Figure 4b after monsoon season ended.

Figure 5 showed the analysis carried out to investigate the changes of profile at sites due to NEXC Block installation in 2-dimension. Few transect lines were generated at site referring to lines as per physical experiment conducted in laboratory for calibration and validation. Blue line represented the beach profile right after the installation work in October 2015. Black transect line represented beach profile during monsoon in January 2016. Finally, green line showed the beach profile after extreme water level and high wave events reported in February 2016. Based on the analysis it was proven that water level, wave magnitude and beach profile were the main parameters in determining scour impact at the toe of structure, as per results in the study in 2D wave flume laboratory. The erosion depth at the front of structure, and sediment accumulation at the leeside was recorded continuously during monsoon. Sediment accumulation at both front and back sides were also recorded during calmer period; after monsoon season has ended.

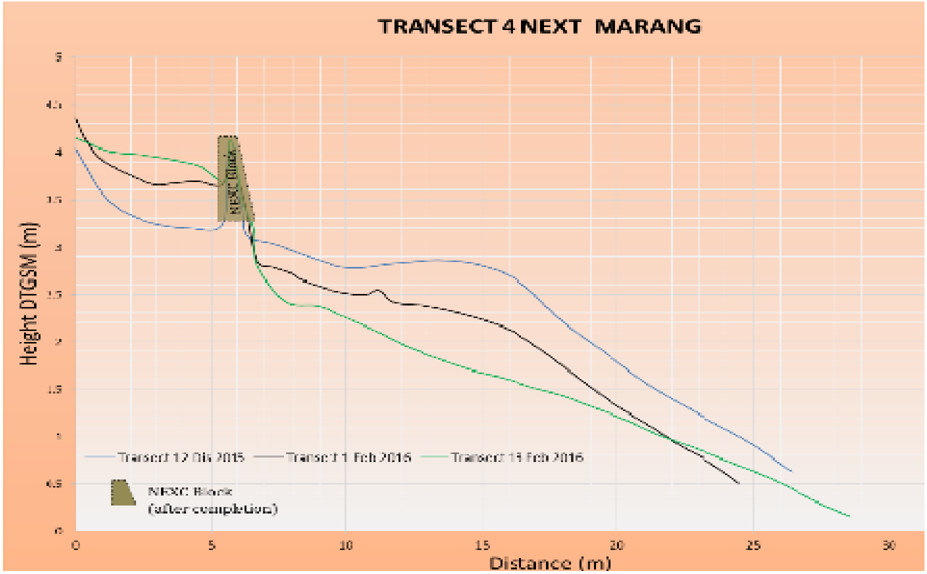

Beach profiling analysis at site

Figure 5. Analysis of beach profile changes.

Figure 6 shows the detail structure of NEXC Block at full scale model. The dimension is 1.2m x 1.2m x 1.2m and weighs approximately 2,500kg each. The various selection of fill materials includes reinforced concrete, concrete waste, recycle items or existing sediment material available at site with HDPE as framework, depending on the proposed site and existing coastal morphological processes. On a sandy beach, concrete structure is proposed, whereas mud-fill modules can be used at a muddy coastline.

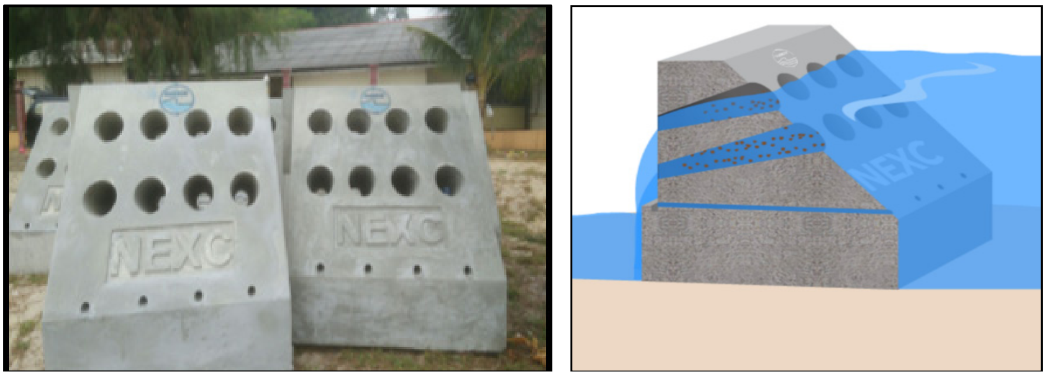

Figure 6. NEXC Block in full scale dimension.

6 CONCLUSIONS

In general, rate of erosion is dependent on wave magnitude and water level. Higher wave breaks earlier and farther from the shoreline as compared to lower wave. However due to wave energy by higher wave, even after breaking, the wave propagates further inland with higher volume. Thus, higher wave causes more erosion as compared to lower wave height, as same goes to water level parameter.

As water level increases, due to less bathymetry effect, the breaking point also moves to a point nearer to the beach thus leads to higher erosion rate. The experiment thus proves that the worst erosion occurs during the combination of high water level and high wave magnitude. This shows the importance of physical experiment in understanding the interaction between waves, water level, sediment and structure, which is related to erosion-accretion processes.

NEXC Block installation is found fairly successful in controlling the erosion within the interest area. Sand loss due to erosion and scour is limited to only at the face of the structure, whereas the backside or leeside of installation is found fairly stable. However, during high water level and high wave event, scouring problem is prevalent. Hence scour protection units is proposed to be combined with NEXC Block installation. In a long-term period, sediments are returned back to the beach hence naturally expanding the beach. Result of experiments in laboratory works in 2D wave flume has been validated using actual site measurement. Hence physical experiment approach is still considered as one of the best approaches in conducting study within coastal zones especially with regards to product development, where the dynamic processes are still found challenging to simulate numerically.

For future work study, focus can be given to improve the efficiency of scour protection. One of the main advantages of NEXC Block is the various selection of fill materials can be used depending on existing coastal morphological processes; such as reinforced concrete, concrete waste, recycle items or existing sediment material available at site with HDPE as framework.

a. NEXC Block installation in Marang, Terengganu b. NEXC Block structure in Port Dickson, Negeri Sembilan

Figure 7. NEXC Block installation at sites.

©2017, IAHR. Used with permission / ISSN 1562-6865 (Online) - ISSN 1063-7710 (Print)

ACKNOWLEDGEMENTS

All staff of Coastal and Oceanography Research Centre and Hydraulic and Instrumentation Laboratory, and National Hydraulic Research Institute of Malaysia is thanked for their assistance and contribution in conducting the experiments. Special acknowledgment also for the research team from Faculty of Civil Engineering, Universiti Teknologi Malaysia for their support. Continuous corporation and assistance from the Drainage and Irrigation Department (DID) of Malaysia, DID state of Negeri Sembilan, DID state of Terengganu and respective local authorities in site installation works as in Figure 7 are highly appreciated. Finally, the Government of Malaysia is also thanked for the approved research grant for related studies. NEXC Block has successfully registered in Industrial Design category MY16000690101 from MyIPO.on January 2016.

REFERENCES

Allsop, N. W. (1986). *Seawall; A Literature Review.* Wallingford, Oxfordshire: Hydraulics Research Limited, 1-168.

Ghazali, N. H. (2006). Coastal Erosion and Reclamation in Malaysia. *Aquatic Ecosystem Health and Management,* 9(2), 237-247.

Goda Y. (1974). New Wave Pressure Formulae for Composite Breakwaters. *Proceedings of the 14th International Coastal Engineering Conference,* 3, 1702-1720.

Hanbin GU, Pengzhi LIN, Yanbao LI, Taiwen HSU & Jianlue HSU. (2003). Wave Characteristics in Front of Vertical Sea-Walls. *International Conference on Estuaries and Coasts, Hangzhou, China*, 389-396.

Hwang, P. A. (1990). Air Bubbles Produced by Breaking Wind Waves: A Laboratory Study. *Journal of Physical Oceanography,* 20, 19-28.

Kamphuis, J. W. (2000). *Introduction to Coastal Engineering and Management.* Singapore: World Scientific Publishing, 1-564.

Pilkey, O. H.; Dixon, K. L. (1996). The Corps and the Shore. *Island Press, Washington D.C.*, 272.

Tanimoto. K., Moto, K., Ishizuka, S. & Goda, Y. (1976). An Investigation on Design Wave Force Formulae of Composite-Type Breakwaters. *Proceedings of the 23rd Japanese Conference on Coastal Engineering*, 11-16.

US Army Engineers. (1984). *Shore Protection Manual Volume 1.* Washington D.C.: Department of the Army, US Army Corps of Engineers, 1-337.

Proceedings of the 37th IAHR World Congress
August 13 – 18, 2017, Kuala Lumpur, Malaysia

THE IMPACT OF SEA LEVEL RISE ON TIDES AND STORM SURGES AROUND COAST OF TAIWAN

WEN-CHENG LIU(1), WEI-CHER HUANG(2) & ZHE-YONG ZHOU(3)

(1, 3) Department of Civil and Disaster Prevention Engineering, National United University, Miaoli, Taiwan,
wcliu@nuu.edu.tw; robin1008ll@yahoo.com.tw
(2)Ph. D. Program in Materials and Chemical Engineering, National United University, Miaoli, Taiwan,
D0412002@nuu.edu.tw

ABSTRACT

In this study, a two-dimensional advanced circulation model (ADCIRC) is used to simulate tides and storm surges around Taiwan's coast. The model was calibrated and verified with the observed tides and storm surges at four tidal gauge stations, which are the Taipei Tamsui, Taichung Harbor, Kaohsiung Harbor, and Hualien Harbor for historical typhoon events. The results showed a reasonable agreement between the simulated and the observed tidal levels and surge tides. The validated model was then used to assess the impact of sea level rise (SLR) on tides and surge heights. Four typical typhoon events under present sea-level condition, SLR 0.87m, and SLR 1.9m were used for model simulations. The simulated results showed that SLR increased tides and surge heights significantly at the Taichung Harbor, while there was a little influence at the Taipei Tamsui, Kaohsiung Harbor, and Hualien Harbor. The timing of the tide would arrive earlier by around 3.5 hrs. The maximum increases of water level range from 0.092m and 0.137m under SLR 0.87m, while they range from 0.192m and 0.248m under SLR 1.9m at the Taichung Harbor.

Keywords: Advanced circulation model (ADCIRC); sea level rise; tide; storm surge; Taiwan's coast.

1 INTRODUCTION

Mean sea level rise (SLR) is one of the most discussed issues of climate change. SLR will apparently affect coastal regions worldwide by posing dangers such as beach erosion, salt water intrusion into groundwater systems, coastal flooding, imbalance of ecosystems, and infrastructure damage (Craft et al., 2009; Almas et al., 2012; Tang et al., 2013). The SLR have been predicted by many scientists and researchers by means of hydrological, climatological, and/or dynamical models (Zuo and Oerlemans, 1997; Gregory and Orelemans, 1998; Raper and Braithwaile, 2006). The recent projections of global SLR in the Intergovernmental Panel on climate Change (IPCC) Fifth Assessment Report revealed that the possible increase was in the range of 0.26-0.98m by 2100 compared to 1986-2005 (Church et al., 2013; Bittermann et al., 2013). Church and White (2006; 2011) projected that the present global SLR is approximately 1.9mm/year and this might be expected to accelerate over the present century. Rahmstorf (2007) estimated the SLR will increase 0.2-2m for the year 2011. Scientists also suggested that a 1-5m rise in sea level by 2100 is more realistic when several reasons including melting of ocean glacier, ice sheet disintegration, and thermal expansion of ocean water was taken into account (Pfeffer, 2008; Bahar et al., 2009; Grinsted et al., 2010).

SLR over the last century has significant changes on the global tides, but the global tidal models have the limitation to reproduce these changes because of the coarse resolution used in the models (Muller et al., 2011). However, the SLR has a large impact on regional tides that have been reported due to the high-resolution grids implemented in the models (Pickering et al., 2012; Ward et al., 2012; Pelling et al., 2013). Recently, Bilskie et al. (2014) applied SWAN+ADCIRC (Simulating Waves Nearshore + Advanced CIRCulation) code to project the land use/land cover and sea level rise scenarios in the Mississippi and Alabama coast. The results showed that the response of storm surge and coastal flooding to SLR is dynamic and very sensitive to changes in the land use/land cover. Lopes and Dias (2014) highlighted that tidal current magnitude increased with mean SLR. The tidal wave propagation would be significantly changed as mean SLR. Zao et al. (2014) investigated the influence of SLR on storm surge around the Changjiang Estuary. They found that the surges are not very sensitive to the SLR and the variations in elevation could attribute to the changes in tides. Luz Clara et al. (2015) applied the Model for Applications at Region Scales (MARS) to probe the changes on tides in the Patagonian Continental Shelf. The modeling results revealed that the tidal characteristics were changed with SLR as a result of the speed of tidal wave, the deformation on Rossby radius, the energy dissipation by bottom friction, and the resonant properties in the basin. Arns et al. (2015) used Mike21-FM to investigate the impact of SLR on storm surge water levels in the northern part of the German Bight based on 65 extreme events occurred between 1970 and 2009. They found that the water level residuals in the study area were mainly caused by nonlinear changes in the tidal constituents. Bilskie et al. (2016) investigated the tropic cyclone-driven storm surge inundation under sea level rise with geomorphic changes along the northern Gulf of Mexico using coupled SWAN+ADCIRC. The analyses of modeling results suggested that the interaction between storm surge and SLR is nonlinear in time. SLR would increase the time of inundation, causing an earlier arrival of peak surge.

The tides and storm surges modulated by the SLR in the coastal regime of Taiwan were not yet investigated using numerical model with high-resolution meshes. The main objective of this study is to investigate the influence of SLR on tides and storm surges around coast of Taiwan with ADCIRC-2D (Advanced Circulation Model for Oceanic, Coastal and Estuarine Waters) model.

2 MATERIALS AND METHODS

2.1 Storm surge model

The advanced storm surge and circulation model, Advanced Circulation (ADCIRC) (Luettich et al., 1992) was used to simulate the response of water levels and currents along the Taiwan coast. The barotropic dynamics are dominant and baroclinic effects are assumed to be relatively small during typhoon events. Therefore, the two-dimensional, depth-integrated model (ADCIRC-2DDI) was used in the present study. The two-dimensional version of ADCIRC solves the depth-integrated, nonlinear momentum and continuity equations in the time domain. ADCIRC utilizes the finite-element method, which provides the flexibility to resolve the complex geometry and bathymetry of coasts. However, the finite element solution to the shallow water equations induces spurious terms and numerical instability. Hence, to reformulate the governing equations into a form that provides a stable solution in the finite element representations becomes necessary. The ADCIRC-2DDI adopts the Generalized Wave Continuity Equation (GWCE) combined with the momentum conservation equations, to eliminate this issue (Westerink et al., 1994). The model is forced by surface elevation at open boundary, zero land boundary flux, variable spatial and temporal free surface wind, and atmospheric pressure. It handles wetting-drying characteristics in low-lying areas. Numerous applications of the model by the US Army Corps of Engineers and other institutions have been reported in the literature (Dietrich et al., 2011; Bhaskaran et al., 2014).

2.2 Typhoon model

The storm surge is mainly driven by the wind stress and pressured field. There are several approaches to simulate wind stress and pressure field for a typhoon. To simplify the numerical calculation, the pressure fields and wind fields are derived from the independent formulas. The atmospheric pressure field for the cyclone was calculated using the equation expressed below (Holland, 1980):

$$p_a = p_c + \Delta p \cdot \exp[-(\frac{r}{r_m})^{-B}],\ \ \Delta p = p_e - p_c\ ,\ r > 0 \tag{1}$$

where P_c is the ambient pressure or environmental pressure; $\triangle P$ is the pressure drop or pressure deficit; r is the radius, which is the distance from the typhoon center; r_m is the radius of maximum wind speed; and B is the shape parameter, which can be estimated by the following empirical relationship (Jakobsen and Madsen, 2004).

$$B = 0.1397(\Delta p)^{0.288}\ ,\ r > 0 \tag{2}$$

When r equals zero, P_a is set to P_c and maximum wind speed is set to be zero.

Although typhoons possess different shapes, they can be expressed as a circular storm on the ocean. The circular typhoon model of Jelesnianski (1965) is widely used in many tropical cyclone surge models. This model that is used to calculate the wind field is described as follows:

$$W = \frac{r}{r_m + r}(U_w i + V_w j) + W_m \frac{1}{r}(\frac{r}{r_m})^{3/2}(ai + bj),\ \ 0 < r \le r_m \tag{3}$$

$$W = \frac{r_m}{r_m + r}(U_w i + V_w j) + W_m \frac{1}{r}(\frac{r_m}{r})^{1/2}(ai + bj),\ \ r > r_m \tag{4}$$

$$a = -r_\lambda \sin\theta - r_\varphi \cos\theta,\ \ b = r_\lambda \cos\theta - r_\varphi \sin\theta$$

where *(I, j)* are unit vectors in longitude and latitude; U_w, V_w are the components of the translation velocity of the cyclone center; W_m is the maximum wind; r_λ and r_φ are the components of the vector *r*; and θ is the inflow angle of range 0-30°.

2.3 Model implementation

The computational domain in the Asian marginal seas and the western Pacific Ocean includes the region within the longitudes 117°E to 125°E and the latitudes 21°N to 28°N. The Digital Terrain Model (DTM) bathymetric data were obtained from the Global Topography data bank of the University of California, San Diego, and from the Ocean Data Bank of the National Science Council, Taiwan. Figure 1a illustrates the bathymetric map and the locations of the tidal gauge stations on the east coast of Taiwan, respectively. In Figure 1a, location A is Taipei Tamsui; location B is Taichung Harbor; location C is Kaohsiung Harbor and location D is Hualien Harbor. In order to save computational time and fit the coastline, coarse grids were generated in coastal seas, whereas fine grids were used in shallow areas close to the coastline. The modeling domain consisted of 74,124 unstructured triangular elements and 37,639 nodes (Figure 1b). To fit the raw bathymetric data and simply define the open boundary conditions at corner points, rectangular area (see Figure 1b) was adopted in the modeling domain. Based on the model grids generated on the coastal ocean around Taiwan, a time step of Δt= 20 seconds was adopted in simulations to guarantee model stability.

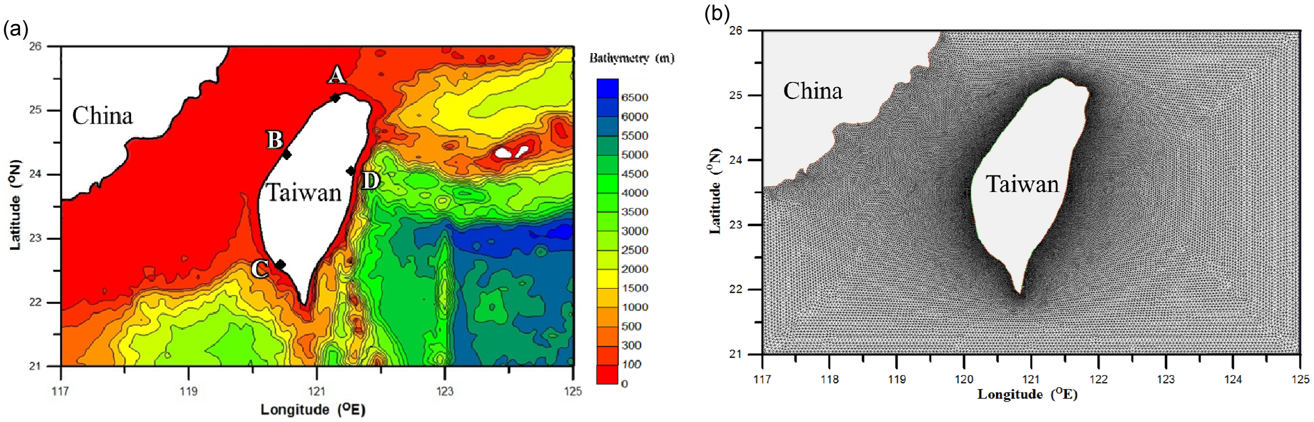

Figure 1. (a) Bathymetric map and locations of tidal gauge stations along the coast of Taiwan, and (b) an unstructured grid in the modeling domain for the simulation.

2.4 Model performance

The model is quantitatively assessed by three criteria that were adopted to compare the predicted results and the observational data. They are the mean absolute error (MAE), root mean square error (RMSE), and Skill. These criteria are defined by the following equations:

$$MAE = \frac{1}{N}\sum_{i=1}^{N}\left|(Y_m)_i - (Y_o)_i\right| \qquad [5]$$

$$RMSE = \sqrt{\frac{1}{N}\sum_{i=1}^{N}[(Y_m)_i - (Y_o)_i]^2}\ , \qquad [6]$$

$$Skill = 1 - \frac{\sum_{i=1}^{N}\left|(Y_m)_i - (Y_o)_i\right|^2}{\sum_{i=1}^{N}\left[\left|(Y_m)_i - \overline{Y_o}\right| + \left|(Y_o)_i - \overline{Y_o}\right|\right]^2} \qquad [7]$$

where *N* is the total number of data; Y_m is the predicted water level; Y_o is the observational water level; and $\overline{Y_o}$ is the mean value of observational water level. A skill value of 1.0 means perfect performance of model, excellent for skill between 0.65 and 1, very good for skill in the range of 0.5-0.65, good for skill in the range of 0.2-0.5, and poor for skill less than 0.2 (Chen et al., 2016).

3 MODEL CALIBRATION AND VALIDATION

Several sets of observational data were used to determine the model's accuracy and to validate its predictive abilities and capabilities. Four typhoon events, Tyohoon Mindule (2004), Typhoon Namadol (2004), Typhoon Longwang (2005), and Typhoon Kaemi (2006), were used for model calibration. Three typhoon events, Typhoon Wipha (2007), Typhoon Jangmi (2008) and Typhoon Fanapi (2010), were used for model validation. Figure 2 illustrates the tacks of seven typhoons, which cover the categorized paths, 1, 2, 3, 4, 6, and 9. Table 1 also shows the periods, landfall date, path, and intensity of these seven typhoon events.

The model results for the tidal simulation and storm tide in terms of water level during typhoon events for model calibration are shown in Figure 3 for Typhoon Mindulle (typhoon path 6). Figure 3 reveals that the model reasonably simulated both the spatial and temporal patterns of the tide and the storm surge. Since the simulated wind fields were used to force the model, slight differences between the model simulation and the observations at some stations can be found. Overall, the model results agree well with the observations. Table 2 shows the model performance between the computed and observed water levels for model calibration. The maximum MAE and RMSE values are 0.16 m and 0.24 m, respectively, at the Taichung Harbor for Typhoon Longwang. However, the model Skill reaches 0.99.

Figure 4 presents the model validation results for tide and storm surge tide in terms of water level for Typhoon Jangmi (2008) (typhoon path 2). The model results could not really capture the observed water level at the Hualien Harbor during storm surge. It might be the reason that the typhoon model could not reflect the observed wind stress at the Hualien Harbor. However, the results of the model simulation closely match the observations at the Taipei Tamsui, Taichung Harbor, and Kaohsiung Harbor. Table 3 presents the model performance between the computed and observed water levels for model validation. It shows that the maximum MAE and RMSE values are 0.18 m and 0.24 m respectively, at the Taichung Harbor for Typhoon Jangmi, but the model Skill also reaches 0.99.

From the model calibration and validation procedures, the horizontal eddy viscosity parameter was set to 5.0 m^2/s. A constant minimum bottom friction coefficient of $C_{f\min}$=0.003, break depth of H_{break}=10m, and two dimensionless parameters of α=10 and β=1/3 were used. The parameters used in this study are in the reasonable ranges that can be found in Luettich et al. (1992).

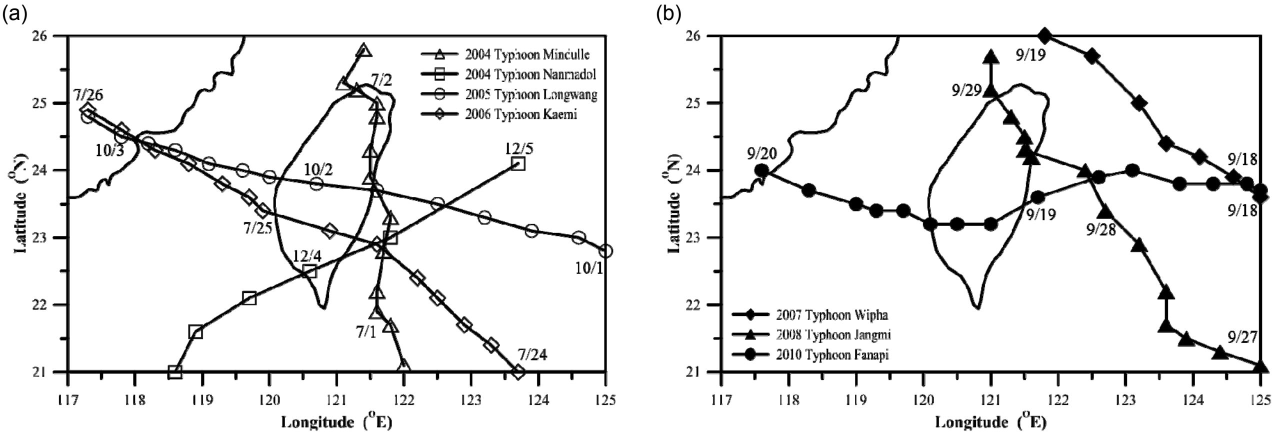

Figure 2. Tracks of typhoon events for (a) model calibration and (b) model validation.

Table 1. The period, landfall date, path, and intensity of seven typhoon events used for model calibration and validation.

Typhoon event	Model calibration				Model validation		
	Typhoon Mindulle	Typhoon Nanmadol	Typhoon Longwang	Typhoon Kaemi	Typhoon Wipha	Typhoon Jangmi	Typhoon Fanapi
Period (month/ day /year)	6/28/2004~ 7/4/2004	12/3/2004~ 12/4/2004	9/30/2005~ 10/3/2005	7/23/2006~ 7/26/2006	9/17/2007~ 9/19/2007	9/26/2008~ 9/29/2008	9/17/2010~ 9/20/2010
Landfall date	7/1/2004	12/4/2004	10/1/2005	7/24/2006	9/18/2007	9/28/2008	9/19/2010
Path	6	9	3	3	1	2	4
Intensity	Middle	Middle	Strong	Middle	Middle	Strong	Middle

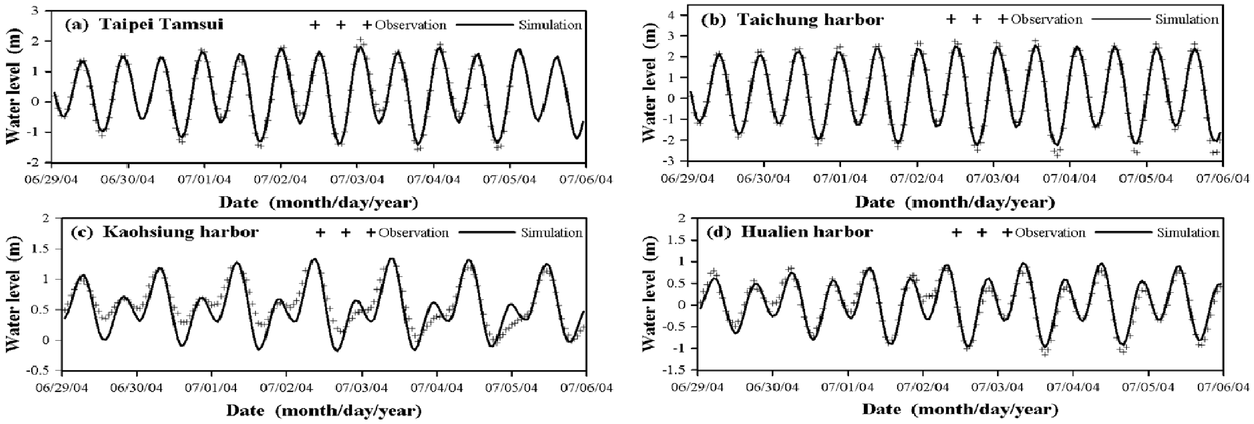

Figure 3. Comparison of model results of water level with observations for model calibration with Typhoon Mindulle (2004) (typhoon path 6).

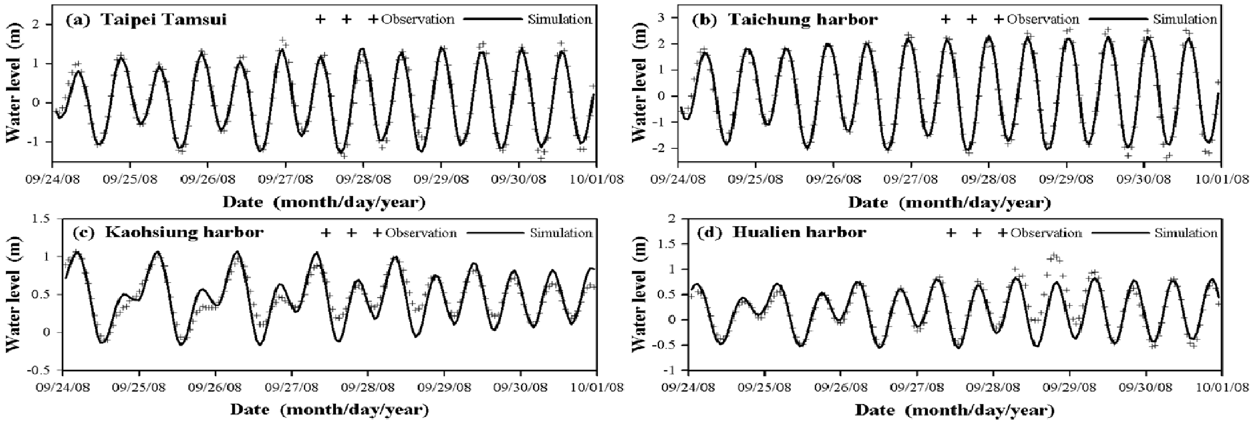

Figure 4. Comparison of model results of water level with observations for model validation with Typhoon Jangmi (2008) (typhoon path 2).

Table 2. Mean square error (MAE), root mean square error (RMSE), and skill of the difference between the computed and observed water levels for model calibration.

Gauge station	Mindulle (2004)			Nanmadol (2004)			Longwang (2005)			Kaemi (2006)		
	MAE (m)	RMSE (m)	Skill	MAE (m)	RMSE (m)	Skill	MAE (m)	RMSE (m)	Skill	MAE (m)	RMSE (m)	Skill
Taipei Tamsui	0.13	0.17	0.99	0.13	0.16	0.99	0.12	0.14	0.99	0.12	0.15	0.99
Taichung Harbor	0.16	0.20	1.00	0.15	0.19	0.99	0.16	0.24	0.99	0.16	0.22	0.99
Kaohsiung Harbor	0.16	0.20	0.91	0.08	0.10	0.97	0.08	0.09	0.96	0.13	0.17	0.94
Hualien Harbor	0.13	0.16	0.98	0.09	0.11	0.97	0.08	0.09	0.99	0.08	0.10	0.99

Table 3. Mean square error (MAE), root mean square error (RMSE), and skill of the difference between the computed and observed water levels for model validation.

Gauge station	Wipha (2007)			Jangmi (2008)			Fanapi (2010)		
	MAE (m)	RMSE (m)	Skill	MAE (m)	RMSE (m)	Skill	MAE (m)	RMSE (m)	Skill
Taipei Tamsui	0.12	0.16	0.99	0.13	0.17	0.99	0.17	0.20	0.98
Taichung Harbor	0.18	0.23	0.99	0.18	0.24	0.99	0.16	0.21	0.99
Kaohsiung Harbor	0.08	0.10	0.95	0.10	0.13	0.95	0.12	0.15	0.92
Hualien Harbor	0.11	0.15	0.95	0.13	0.19	0.95	0.10	0.12	0.96

4 MODEL APPLICATIONS AND DISCUSSION

The validated model was then used to investigate the influence of sea level rise on tides and surges around the coast of Taiwan. However, the projections of SLR for 21st century vary widely, ranging from several centimeters to more than a meter. According to the different reports from literature (Rahmstorf et al., 2007; Katsman et al., 2008), two relative sea level rise scenarios over the next century were selected. The sea level rises, 0.87m and 1.90m, were used in the model simulations.

Four typhoon events, Typhoon Mindulle (2004), Typhoon Nanmadol (2004), Typhoon Longwang (2005), and Typhoon Jangmi (2008), served as the case study because the tracks of these typhoons are close to four tidal gauge stations, Taipei Tamsui, Taichung Harbor, Kaohsiung Harbor, and Hualien Harbor (see Figure 5).

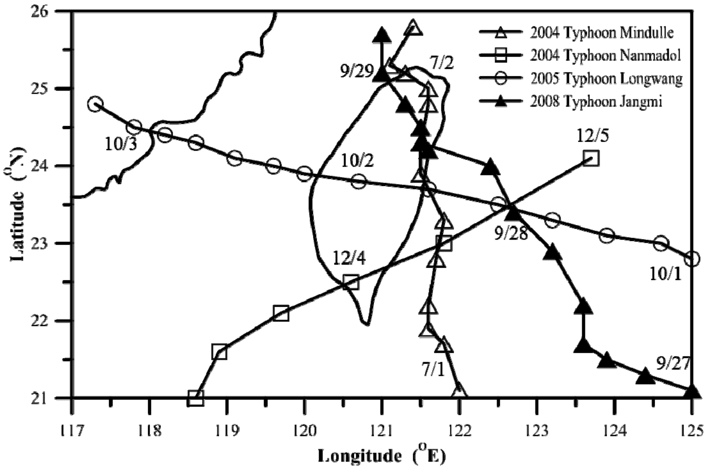

Figure 5. Tracks of Typhoon Mindulle (2004), Typhoon Nanmadol (2004), Typhoon Longwang (2005), and Typhoon Jangmi (2008) served as model simulation to investigate the influence of sea level rise on tide and storm surge.

4.1 The effect of sea level rise on tides

Figure 6 presents the water level at present condition and difference of water level between present condition and sea level rise. It shows that the water level at the Taipei Tamsui, Taichung Harbor, Kaohsiung Harbor, and Hualien Harbor increases as a result of sea level rise. The notable difference of water level between present and sea level rise, 0.87m and 1.90m is the Taichung Harbor. There are no notable effects of sea level rise on tides at the Kaohsiung Harbor and Hualien Harbor. Table 4 shows the maximum differences of water level between present and sea level rise of 0.87m and 1.90m at tidal gauge stations. The maximum increases of water level are in the range of 0.092m and 0.137m under sea level rise of 0.87m, while they are in the range of 0.192m and 0.248m under sea level rise of 1.9m at the Taichung Harbor.

Zao et al. (2014) selected three gauge stations at the continental shelf which the water depth was less than 100m to investigate the effect of sea level rise on tides. They found that sea level rise significantly affected and increased the water level. The predicted results were similar with the literature reported by Zao et al. (2014). However, the water depths reach 3000 m and 6000 m at the Kaohsiung Harbor and Hualien Harbor, respectively. The change of sea level rise on water level is not notable. The bottom friction and topography would cause different patterns of water level due to sea level rise.

Arns et al. (2015) documented that attributed effects were changes in phase lags of individual constituents leading to a different tidal modulation, thus additionally increasing tidal water levels due to sea level rise. Howard et al. (2010) investigated the effect of high SLR values up to 5m on the tide and surge at the Thame Estuary grid box (Southend) using the UK operational model. They found the primary effect was the timing of the tide, with earlier arrival of high water by around 1 h and effect on water level of less than 10cm. We found that a phase shift and the timing of water level would earlier arrival of high tide by around 3.5 hours appeared at the Taichung Harbor due to sea level rise. It revealed that water level increased resulting in the increasing tidal wave propagation in the coastal areas.

4.2 The effect of sea level rise on surges

Figure 7 illustrates the time-series surge height during typhoon events and difference of surge height induced by sea level rise, 0.87m and 1.9m. It shows that the surge height at the Taipei Tamsui, Taichung Harbor, Kaohsiung Harbor, and Hualien Harbor increases due to sea level rise. The obvious discrepancy of surge height induced by sea level rise can be found at the Taichung Harbor, while there is not notable difference exhibited at the Kaohsiung Harbor and Hualien Harbor. Table 5 indicates the maximum differences of surge height induced by sea level rise of 0.87m and 1.90m at tidal gauge stations. The maximum increases of surge height induced by sea level rise of 0.87m are in the range of 0.059m and 0.149m, while surge height induced by sea level rise of 1.9m are in the range of 0.071m and 0.133m at the Taichung Harbor.

Zao et al. (2014) and Arns et al. (2015) reported that the increase in water depth caused a decrease in surge heights. The nonlinear terms of bottom friction and wind stress and topography affected surge heights induced by sea level rise. The water depth at the Taichung Harbor is shallower than that at the Taipei Tamsui, Kaohsiung Harbor, and Hualien Harbor. Therefore, the surge height induced by sea level rise obviously increases at the Taichung Harbor. There is minor effect of sea level rise on surge height at the Kaohsiung Harbor and Hualien Harbor (see Figure 7). The peak of water level and surge height near shore could experience a significant increase which would cause danger to coastal safety in future sea level rise. Atkinson et al. (2013) also demonstrated that as storm intensity and SLR values increased, causing the increasing of coastal flooding. The topography also controlled the coastal flooding. However, not all geographic regions are equally at risk to future flood level increases.

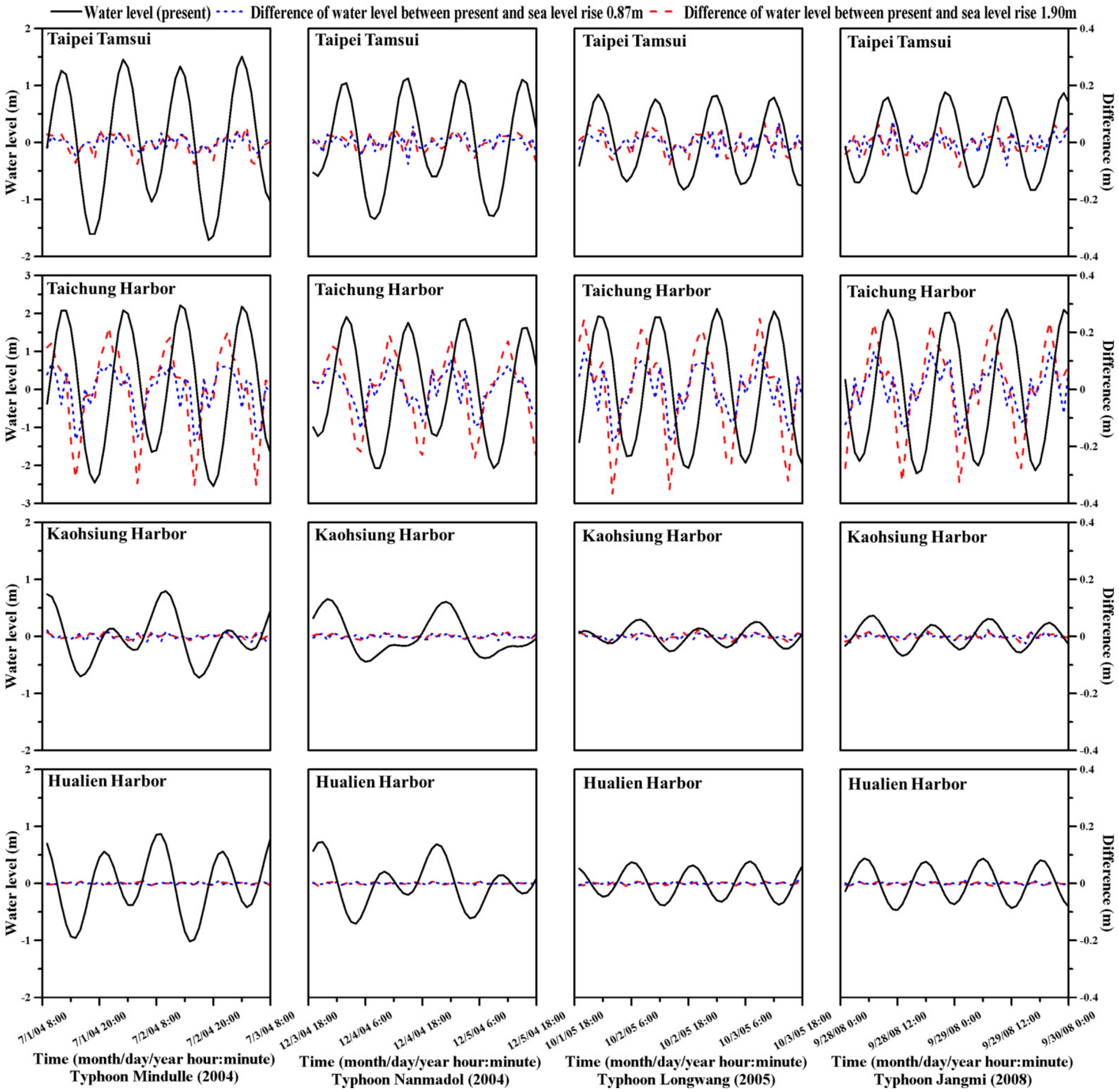

Figure 6. Time-series water level and difference of tide induced by sea level rise at the Taipei Tamsui, Taichung Harbor, Kaohsiung Harbor, and Hualien Harbor. The changes caused by sea level rises drawn in blue (+0.87m) and red (+1.9m). The black lines represent time-series water level for the present condition (baseline). Columns from left to right are Typhoon Mindulle (2004), Typhoon Nanmadol (2004), Typhoon Longwang (2005), and Typhoon Jangmi (2008).

Table 4. Maximum difference of water level between present condition and sea level rise of 0.87m and 1.9m.

Gauge station	Maximum difference induced by sea level rise of 0.87m (m)				Maximum difference induced by sea level rise of 1.9m (m)			
	Mindulle (2004)	Nanmadol (2004)	Longwang (2005)	Jangmi (2008)	Mindulle (2004)	Nanmadol (2004)	Longwang (2005)	Jangmi (2008)
Taipei Tamsui	0.039	0.055	0.069	0.074	0.057	0.052	0.07	0.07
Taichung Harbor	0.092	0.108	0.137	0.133	0218	0.192	0.248	0.237
Kaohsiung Harbor	0.021	0.014	0.017	0.023	0.016	0.015	0.024	0.023
Hualien Harbor	0.013	0.008	0.010	0.012	0.008	0.006	0.008	0.007

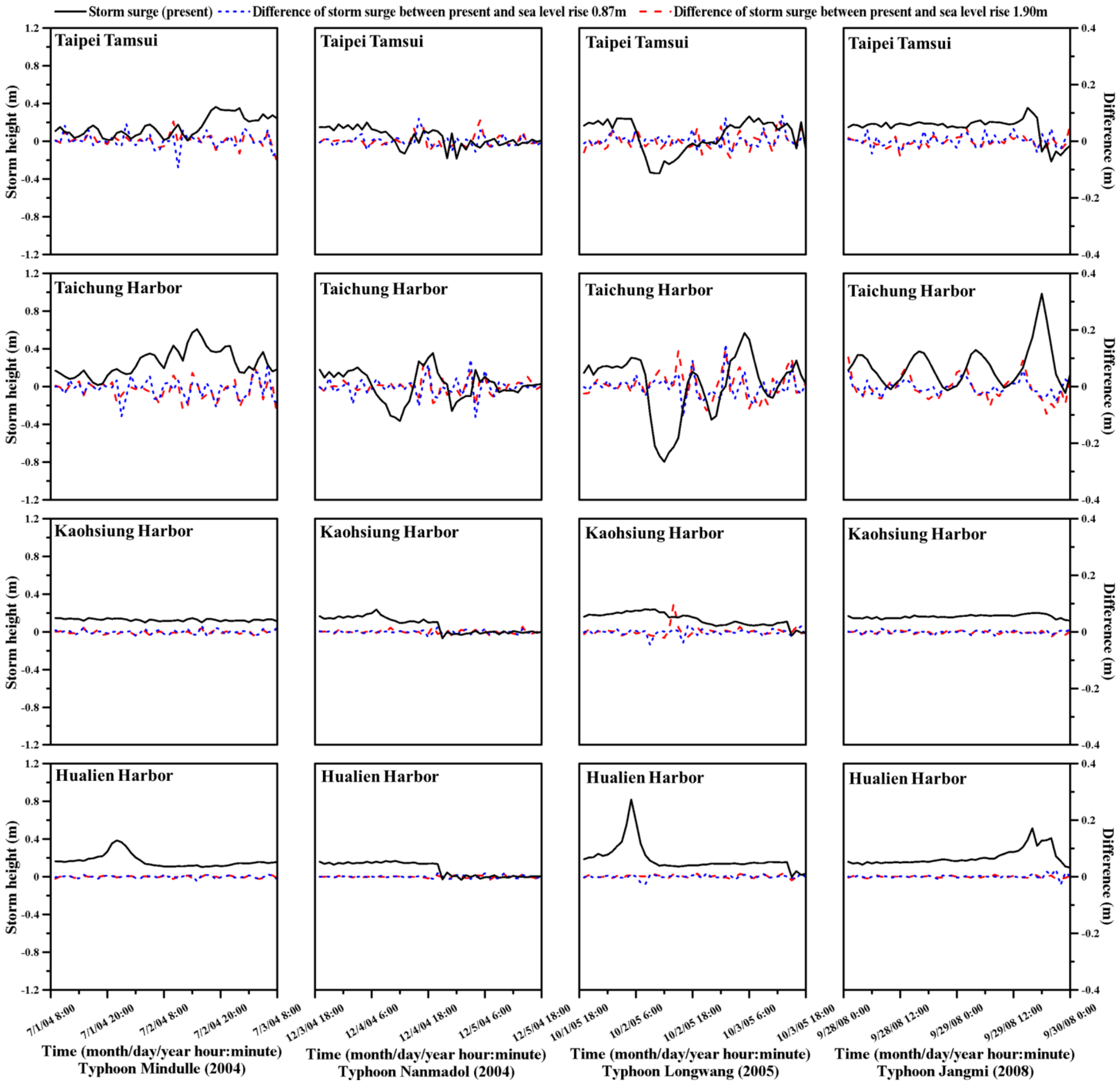

Figure 7. Time-series surge height and difference of surge induced by sea level rise at the Taipei Tamsui, Taichung Harbor, Kaohsiung Harbor, and Hualien Harbor. The changes caused by sea level rises drawn in blue (+0.87m) and red (+1.9m). The black lines represent time-series surge height for the present condition (baseline). Columns from left to right are Typhoon Mindulle (2004), Typhoon Nanmadol (2004), Typhoon Longwang (2005), and Typhoon Jangmi (2008).

Table 5. Maximum difference of surge height between present condition and sea level rise of 0.87m and 1.9m.

Gauge station	Maximum difference induced by sea level rise of 0.87m (m)				Maximum difference induced by sea level rise of 1.9m (m)			
	Mindulle (2004)	Nanmadol (2004)	Longwang (2005)	Jangmi (2008)	Mindulle (2004)	Nanmadol (2004)	Longwang (2005)	Jangmi (2008)
Taipei Tamsui	0.062	0.08	0.091	0.045	0.07	0.074	0.078	0.058
Taichung Harbor	0.083	0.096	0.149	0.059	0.071	0.082	0.133	0.104
Kaohsiung Harbor	0.022	0.016	0.023	0.012	0.015	0.021	0.099	0.012
Hualien Harbor	0.009	0.013	0.013	0.026	0.008	0.01	0.012	0.010

5 CONCLUSIONS

A high-resolution two-dimensional, unstructured grid, hydrodynamic model (ADCIRC) was used to simulate tide and storm surge in the coastal sea of Taiwan. A global ocean tidal model developed by the Oregon State University, TOPEX/Poseidon Global Inverse Solution (TPXO), was applied to specify the ocean boundaries of ADCIRC for driving tidal propagation in the sea. A typhoon model was used for simulating wind stress and pressure field. Four typhoon events, Typhoon Mindule (2004), Typhoon Namadol (2004), Typhoon Longwang (2005), and Typhoon Kaemi (2006), were used for model calibration. Three typhoon events, Typhoon Wipha (2007), Typhoon Jangmi (2008), and Typhoon Fanapi (2010), were used for model validation. The results reveal reasonable agreement between model simulations and the observational data with respect to tide and surge tide.

The validated model was applied to investigate the effect of sea level rise on tides and surges using four typhoon events. According to the different reports from literature, two sea level rise scenarios, 0.87m and 1.90m, were used in the model simulations. The simulated results from the model indicate that the water level and surge height at the Taipei Tamsui, Taichung Harbor, Kaohsiung Harbor, and Hualien Harbor increase due to sea level rise. The remarkable difference of water level and surge height induced by sea level rise is the Taichung Harbor, because the water depth is less than 100m at the Taichung Harbor. The timing of water level would have earlier arrival of high tide by around 3.5 hours at the Taichung Harbor because the sea level rises. It showed that the increase in water level results in the increasing of the tidal wave propagation in the coastal areas.

ACKNOWLEDGEMENTS

This study was supported by the Ministry of Science and Technology (MOST), Taiwan, under grant no. 105-2625-M-239-001-MY2. Prof. Luettich, R. and Research Technician Fulcher, C. provided the source code of ADCIRC model were highly appreciated. We would also like to thank Mr. Chen, W.B. for providing the guidance.

REFERENCES

Almas, A.J. & Hygen, H.O. (2012). Impacts of Sea Level Rise toward 2100 on Buildings in Norway. *Building Research and Information,* 40(3), 245-259.

Arns, A., Wahl, T., Dangendorf, S. & Jensen, J. (2015). The Impact of Sea Level Rise on Storm Surge Water Levels in the Northern Part of the German Bight. *Coastal Engineering,* 96, 118-131.

Atkinson, J., Smith, J. M. & Bender, C. (2013). Sea-Level Rise Effects on Storm Surge and near Shore Waves on the Texas Coast: Influence of Landscape and Storm Characteristics. *Journal of Waterway,* 139(2), 98-117.

Bahar, D.B., Dyurgerov, M. & Meier, M.F. (2009). *Sea-Level rise from Glaciers and Ice Caps: A Lower Bound,* Geophysical Research Letters, 36, L03501.

Bhaskaran, P.K., Gayathri, R., Murty, P.L.N., Bonthu, S. & Sen, D. (2014). A Numerical Study of Coastal Inundation and its Validation for Thane Cyclone in the Bay of Bengal. *Coastal Engineering,* 83, 108-118.

Bilskie, M.V., Hagen, S.C., Medeiros, S.C. & Passeri, D.L. (2014). *Dynamics of Sea Level rise and Coastal Flooding on a Changing Landscape,* Geophysical Research Letters, 41(3), 927-934.

Bilskie, M.V., Hagen, S.C., Alizad, K., Medeiros , S.C., Passeri , D.L., Needham, H.F. & Cox, A. (2016). Dynamic Simulation and Numerical Analysis of Hurricane Storm Surge under Sea Level rise with Geomorphologic Changes along the Northern Gulf of Mexico. *Earth's Future,* 4(5), 177-193.

Bittermann, K., Rahmstorf, S., Perrette, M. & Vermeer, M. (2013). Predictability of Twentieth Century Sea-Level Rise from Past Data. *Environmental Research Letters,* 8(1), 014013.

Chen, W., Chen, K, Kung, C., Zhu, D.Z., He, L., Mao, X., Ling, H. & Song, H. (2016). Influence of Sea Level Rise on Saline Water Intrusion in the Yangtz River Estuary, China. *Applied Ocean Research,* 54, 12-25.

Church, J.A., Clark, P.U., Cazenave, A., Gregory, J.M., Jevrejeva, S., Levermann, A., Merrifiled, M.A., Miline, G.A., Nerem, R.S., Nunn, P.D., Payne, A.J., Pfeffer, W.T., Stammer, D. & Unnikrishnan, A.S. (2013). *Sea Level Change, Climate Change 2013: The Physical Science Basis,* Contribution on Working Group I to the Fifth Assessment Report of the Intergovernmental Panel on Climate Change. Cambridge University Press, Cambridge, United Kingdom and New York, NY, USA, 1140.

Church, J.A. & White, N. (2006). A 20th Century Acceleration in Global Sea-Level Rise. *Geophysical Research Letters,* 33, 1-4.

Church, J.A. & White, N. (2011). Sea-Level rise from the Late 19th to the Early 21 Century. *Surveys in Geophysics,* 32, 585-602.

Craft, C., Clough, J., Ehman, J., Joye, S., Park, R., Pennings, S., Guo, H. & Machmuller, M. (2009). Forecasting the Effects of Accelerated Sea-Level rise on Tidal Marsh Ecosystem Services Source. *Frontier in Ecology and the Environment,* 7(2), 73-78.

Dietrich, J.D., Zijlema, M., Westerink, J.J., Holthuijsen, L.H., Dawson, C., Luettich, R.A., Jensen, R.E., Smith, J.M., Stelling, G.S. & Stone, G.W. (2011). Modeling Hurricane Waves and Storm Surge using Integrally-Coupled, Scalable Computations. *Coastal Engineering,* 58(1), 45-65.

Grinsted, A., Moore, J.C. & Jevrejeva, S. (2010). Reconstructing Sea Level from Paleo and Projected Temperatures 200 to 2100 AD. *Climate Dynamics,* 34*(*4), 461-472.

Gregory, J.M. & Oerlemans, J. (1998). Simulated Future Sea-Level rise due to Glacier Melt based on Regionally and Seasonally Resolved Temperature Changes. *Nature,* 391, 474-476.

Holland, G.J. (1980). An Analytic Model of the Wind and Pressure Profiles in Hurricanes. *Monthly Weather Review,* 108(8), 1212-1218.

Howard, T., Lowe, J. & Horsburgh, K. (2010). Interpreting Century-Scale Changes in Southern North Sea Storm Surge Climate Derived from Coupled Model Simulations. *Journal of Climate,* 23, 6234-6247.

Jakobsen, F. & Madsen, H. (2004). Comparison and Further Development of Parametric Tropical Cyclone Models for Storm Surge Modelling. *Journal of Wind Engineering and Industrial Aerodynamics,* 92(5), 375-391.

Jelesnianski, C.P. (1965). A Numerical Calculation of Storm Tides Induced by a Tropical Storm Impinging on a Continental Shelf. *Monthly Weather Review,* 93(6), 343-358.

Katsman, C.A., Hazeleger, W., Drijfhout, S.S., van Oldenborgh, G.J. & Bugers, G. (2008). Climate Scenarios of Sea Level rise for the Northeast Atlantic Ocean: A Study including the Effects of Ocean Dynamics and Gravity changes Induced by Ice Melt. *Climatic Change,* 91(3), 351-374.

Lopes, C.L. & Dias, J.M. (2014). Influence of Mean Sea Level rise on Tidal Dynamics of the Ria de Aveiro Lagoon, Portugal. *Journal of Coastal Research,* SI 70, 574-579.

Luettich, R.A., Westerink, J.J. & Scheffner, N.W. (1992). *ADCIRC: An Advanced Three-Dimensional Circulation Model for Shelves, Coasts and Estuaries, Report I: Theory and Methodology of ADCIRC-2DDI and ADCIRC-3DL,* US Army Corps of Engineers, Technical Report DRP-92-6.

Luz Clara, M., Simionato, C.G., D'Onofrio, E. & Moreira, D. (2015). Future Sea Level Rise and Changes on Tides in the Patagonian Continental Shelf. *Journal of Coastal Research,* 31(2), 519-535.

Muller, M., Arbic, B.K. & Mitrovica, J.X. (2011). Secular Trends in Ocean Tides: Observation and Model Results. *Journal of Geophysical Research,* 116, 1-19.

Pelling, H.E., Mattias Green, J.A. & Ward, S.L. (2013). Modelling Tides and Sea-Level Rise: To Flood or Not to Flood. *Ocean Modelling,* 63, 21-29.

Pfeffer, W.T., Harper, J.T. & O'Neel, S. (2008). Kinematic Constraints on Glacier Contributions to 21-Century Sea-Level Rise. *Science,* 321, 1340-1343.

Pickering, M.D., Wells, N.C., Horsburgh, K.J. & Green, J.A.M. (2012). The Impact of Future Sea-Level Rise on the European Shelf Tides. *Continental Shelf Research,* 35, 1-15.

Rahmstorf, S. (2007). A Semi-Empirical approach to Projecting Future Sea-Level Rise. *Science,* 315, 368-370.

Raper, S.C.B. & Braithwaite, R.J. (2006). Low Sea Level Rise Projections from Mountain Glaciers and Icecaps under Global Warming. *Nature,* 439, 311-313.

Tang, H.S., I-Jy Chien, S., Temimi M., Blain, C.A., Qu, K., Zhao, L.H. & Kraatz, S. (2013). Vulnerability of Population and Transportation Infrastructure at the East Bank of Delaware Bay due to Coastal Flooding in Sea-Level Rise Conditions. *Natural Hazards,* 69, 141-163.

Ward, S.L., Green, J.A.M. & Pelling, H.E. (2012). Tides, Sea-Level Rises and Tidal Power Extraction on the European Shelf. *Ocean Dynamics,* 62(8), 1153-1167.

Westerink, J.J., Luettich, R.A., Blain, C.A. & Scheffner, N.W. (1994). *ADCIRC: An Advanced Three-Dimensional Circulation Model for Shelves, Coasts and Estuaries,* Report 2: Users' Manual for ADCIRC-2DDI. Technical Report, DRP-94, U.S. Army Corps of Engineers.

Zao, C., Ge. J. & Ding, P. (2014). Impact of Sea Level Rise on Storm Surges around the Changjiang Estuary. *Journal of Coastal Research,* SI68, 27-34.

Zuo, Z. & Oerlemans, J. (1997). Contribution of Glacier Melt to Sea-Level Rise since AD 1865: A Regionally Differentiated Calculation. *Climate Dynamics,* 13(12), 835-845.

Proceedings of the 37th IAHR World Congress
August 13 – 18, 2017, Kuala Lumpur, Malaysia

A PRELIMINARY STUDY ON THE IMPACTS OF THE THREE GORGES PROJECT ON SALTWATER INTRUSION IN THE YANGTZE ESTUARY

XIN YAN(1), ZHAOHUA SUN(2) & JUNQIANG XIA(3)

(1,2,3) State Key Laboratory of Water Resources and Hydropower Engineering Science, Wuhan University, Wuhan, China,
yanxinxiaowanzi@163.com; Lnszh@126.com; xiajq@whu.edu.cn

ABSTRACT

In recent years, saltwater intrusion is becoming a serious problem in Yangtze River Estuary. Among the impact factors, riverine discharge process into the sea determines the duration and intensity of saltwater intrusion. The Three Gorges Project (TGP) controls half of the total runoff of the Yangtze River Basin. Since the operation of the TGP, it has drawn much attention if the regulation of discharge changes the regime of saltwater intrusion in the Yangtze River Estuary. Based on the measurements pre- and post- the dam, the impacts of the TGP on saltwater intrusion have been investigated quantitatively, and the results indicate that: (1) owing to the discharge increment caused by the TGP operation in drought season since 2003, on mean annual scale, extreme situation of saltwater intrusion is weakened, and the peak of chlorinity which often occurs in February decreases by 28%; (2) the annual mean frequency of saltwater intrusion in September and October increases 0.8 and 1.5 respectively; (3) the critical discharge of restraining severe saltwater intrusion at Datong is 12000 m^3/s, and the released discharge of TGP should be regulated reasonably to avoid severe saltwater.

Keywords: Saltwater intrusion; river discharge; statistical analysis; three gorges project.

1 INTRODUCTION

The characteristics of saltwater intrusion are more complicated in the Yangtze River Estuary because of the complex topography. Shanghai is very sensitive to the change of upstream-riverine discharge. The saltwater intrusion in February, 2014, sustained 19 days, which caused the drinking water crisis of 2 million people. Saltwater intrusion is affected by river discharge, tide, estuary shape, sea level, etc (Savenijie 1993; Xiao and Sheng et al., 1998). Saltwater intrusion of the Yangtze River Estuary often occurs when the river discharge from upstream is low. Although the water resources of the Yangtze River is rich, its spatial distribution is uneven in flood and dry season, and low flow in dry season is common. As half of the discharge is controlled by the TGP, saltwater intrusion in the Yangtze River Estuary is inevitably influenced by the TGP to some degree.

Many researches about TGP and saltwater intrusion have been reported. Some studies reveal the characteristics of saltwater intrusion in the Yangtze River Estuary (Tang and Xu et al., 2011). Chen and Xu (2011) assumed that the water storage of the TGP would make saltwater intrusion in advance, and intensity, duration, and frequency of saltwater intrusion would increase. Then, some empirical models and numerical calculations of forecasting saltwater intrusion are proposed (Chen and Zhu et al., 2013; Zheng and Xiao et al., 2014; Tao and Ge., 2016). Sun and Liu (2008) thinks that the TGP is helpful for dampening saltwater intrusion. Although many scholars have studied on the relationship between saltwater intrusion and the TGP, there still exists some controversies, and did not put forward specific quantitative relationship between the water release of TGP, discharge into the sea, and the saltwater intrusion in the Yangtze River. Therefore, further work based on observational data pre- and post- the TGP should be done to evaluate the impacts of TGP on saltwater intrusion.

This paper is to find out how the TGP affects the saltwater intrusion in the Yangtze River estuary, and how to dampen it by regulating the water release of TGP. Therefore, there are four points that we need to figure out: (1) the characteristics of the saltwater intrusion in the Yangtze River estuary pre- and post- the TGP; (2) the characteristics of discharge at Datong Hydrological Station and Yichang Hydrological Station pre- and post- the TGP, as shown in Figure 1a, and the relationship between them; (3) the connection between river runoff at Datong and saltwater intrusion in the Yangtze River estuary, and determine the specific critical discharge at Datong to dampen severe saltwater intrusion; (4) the response relationship of discharge between Yichang and Datong, and how to regulate the water release at the TGP for relieving the serious saltwater intrusion. We achieved our aim by analyzing daily observed river discharge of Yichang and Datong over the period of 1950~2015, the chlorinity data of Dongfengxisha Reservoir from 2009 to 2014, and the hydrological data of TGP from 2003 to 2015, combining with the data from the available literature. The method used is mainly statistical analysis and correlation analysis.

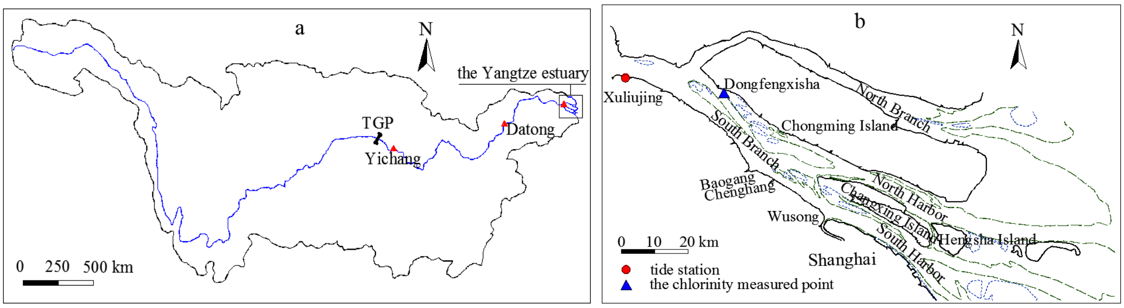

Figure 1. (a) The location of TGP, Yichang and Datong, (b) topography around the Yangtze River Estuary and location of Xuliujing and Dongfengxisha.

2 STUDY SITES AND DATA

We divide the time of TGP into three phases, before the TGP (phase-1: 1950~2002), the impounding test (phase-2: 2003~2007), and the formal impounding (phase-3: 2008~2015). Since the water level of the Three Gorges Reservoir in 2008 and 2009 are close to 175 m, we put it into phase-3. Two hydrological stations were selected as study sites. Yichang hydrological station (111°17′ E, 30°42′ N), locating 44 km below the TGP, is the first hydrological station downstream of the TGP. The correlation coefficient of discharge at Yichang and TGP reaches 0.99, and the lag time is in a day. Thus, its river discharge is used as the presentation of the TGP. Datong hydrological station (117°37′ E, 30°46′ N), locating 1221 km downstream TGP and 642 km upstream to East China Sea, is the last hydrological station downstream the Yangtze River without influence of tidal current and serves as the controlling station for the measurements of the Yangtze River water into the sea. It needs about six days when the discharge at Datong arrives at the Yangtze River Estuary (Chen, 2014). The correlation coefficient of their discharge reaches 0.96, and the discharge of the two stations shows well consistency. Thus, we use discharge at Datong to represent the river runoff into East China Sea. According to the Standard of Surface Water Environmental Quality in the People's Republic of China (《GB3838-2002》), water is not potable, when the value of chlorinity reaches 250 mg/L (salinity value equals 0.48‰). Considering the historical measured data and literatures, if chlorinity in the Yangtze River Estuary is equal or greater than 250 mg/L for ten consecutive days, saltwater intrusion is severe, and this would influence people's lives, agriculture and industry badly. Also, the discharge which can prevent severe saltwater intrusion is defined as the critical discharge for restraining saltwater intrusion.

Data of daily river discharge at Yichang and Datong from 1950 to 2015 were collected on the websites of Changjiang Water Resources Commission of the Ministry of Water Resources (http://www.cjw.gov.cn/). The water level and discharge data of TGP from 2003 to 2015 were collected from China Three Gorges Corporation (http://www.ctgpc.com.cn/sxjt/sqqk/index.html). The chlorinity data (2009~2014) were collected from the observation of Dongfengxisha Station (DFXS) (see in Figure 1a and Figure 1b).

3 CHARACTERISTICS OF SALTWATER INTRUSION PRE AND POST THE TGP

In Figure 2, the x-axis is year, and y-axis is annual frequency and total numbers of days of saltwater intrusion at Chenghang Reservoir in each year. The annual frequency represents times of saltwater intrusion in a year, because each time may last more than one day, therefore total numbers of days means how many days saltwater intrusion occurs in a year. The two values help us to find out the trend of saltwater intrusion in recent years.

Compared the data pre- and post- TGP, the frequency and days of saltwater intrusion have considerable fluctuation before the TGP (frequency: from 0 in 1995 to 13 in 2001; days: from 0 in1995 to 79 in 2002), but this fluctuation is relatively flattened after the impounding of TGP since 2003. Although the maximum days of saltwater intrusion in each year declines by 13%, as a whole, the number of days annually increases from 33.7 (1994~2002) to 41.9 (2003~2015). It means that the operation of TGP may be helpful to avoid extreme case of saltwater intrusion, but also increases the possibility of saltwater intrusion in each year.

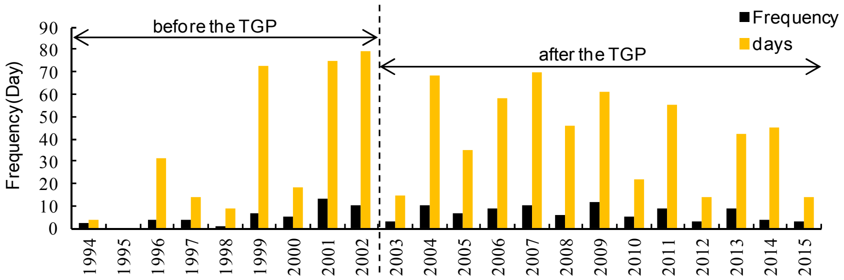

Figure 2. Annual frequency and total number of days of saltwater intrusion in the Chenghang Reservoir from 1994 to 2015 (Liu, 2016).

Figure 3 (a) shows the time of saltwater intrusion, and it reveals that saltwater intrusion often occurs when the river discharge of Datong is minimum. Then, we extract the data of drought season to analyze the characteristics of saltwater intrusion before and after TGP, and add up September and October because of the impounding of TGP, as shown in Figure 3 (b). The result indicates that saltwater intrusion is ahead of time, and the multi-year average days of saltwater intrusion in September, October and November increases by 100%, 50%, 100%, and the rest of the several months decrease orderly by 13% (December), 8% (January), 6% (February), 10% (March), and 19% (April). Therefore, it shows that the every-year impounding of TGP increases the possibility of saltwater intrusion in September, October and November, but deceases the days of saltwater intrusion from December to April of the next year. Also, February and March are the worst period of saltwater intrusion in the Yangtze River Estuary.

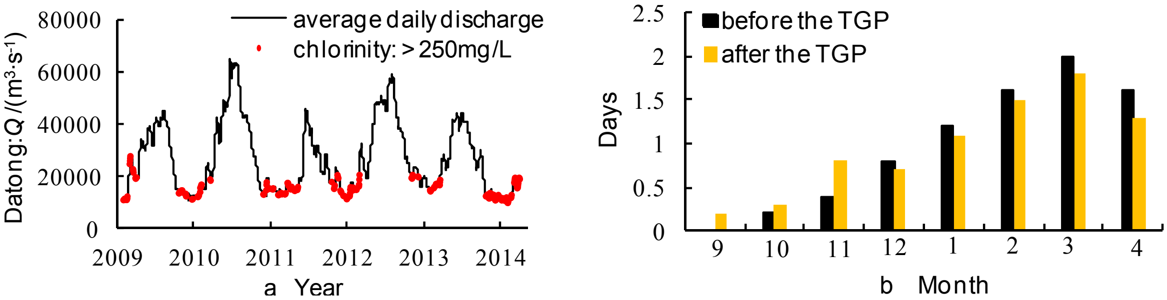

Figure 3. (a) The main period of saltwater intrusion in the Yangtze River estuary, (b) the comparison of saltwater intrusion during the dry season in each month before (1998~2003) and after (2003~2009) TGP (Tang 2011).

During the drought season (see in Figure 4), the peak of chlorinity decreases by 28% (February) and 39% (March), but increases by 79% (October) and 64% (November). Thus, the operation of TGP effectively decreases the intensity of saltwater intrusion in drought season, but increases in the impounding period of TGP.

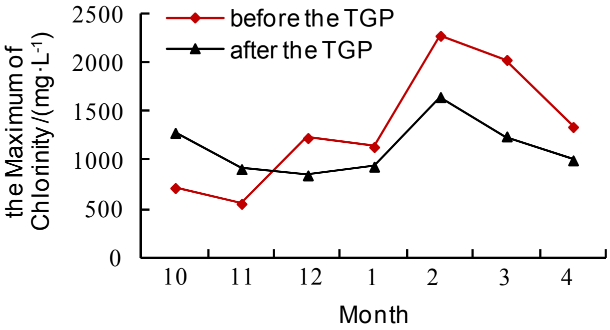

Figure 4. Multi-year maximum of chlorinity in each month during drought season before (1998~2003) and after (2003~2009) the TGP (Tang and Xu et al., 2011).

4 CHANGES OF DISCHARGE AT YICHANG, DATONG AND THE INTERVAL OF THEM PRE AND POST THE TGP

4.1 Changes of annual mean discharge at different stations

Comparing the average daily discharge of Yichang and Datong pre- and post- the TGP (shown in Figure 5 a, b, and c), we found that the peak in flood season is cut down after the TGP. With the operation of TGP, the annual mean discharge at Yichang and Datong reduce respectively by 8% and 5% (pre- the TGP: Yichang is 13840 m^3/s, Datong 28681 m^3/s; post- the TGP: Yichang is 12745 m^3/s, Datong 27312 m^3/s). Relatively, the annual mean discharge coming from the interval of Yichang to Datong decreases by 2%, and this change is less than that at Yichang and Datong. Zhao and Tang et al (2012) indicates that the change of discharge is caused by climate change. According to the reduction ratio of annual mean discharge at Yichang, Datong and the interval between them, it can be deduced that the impact of climate change on annual runoff is more severe in the upstream of Yichang. In addition, because the discharge of Datong is composed of the discharge from Yichang and the interval, the change of annual mean discharge at Datong is mainly influenced by Yichang.

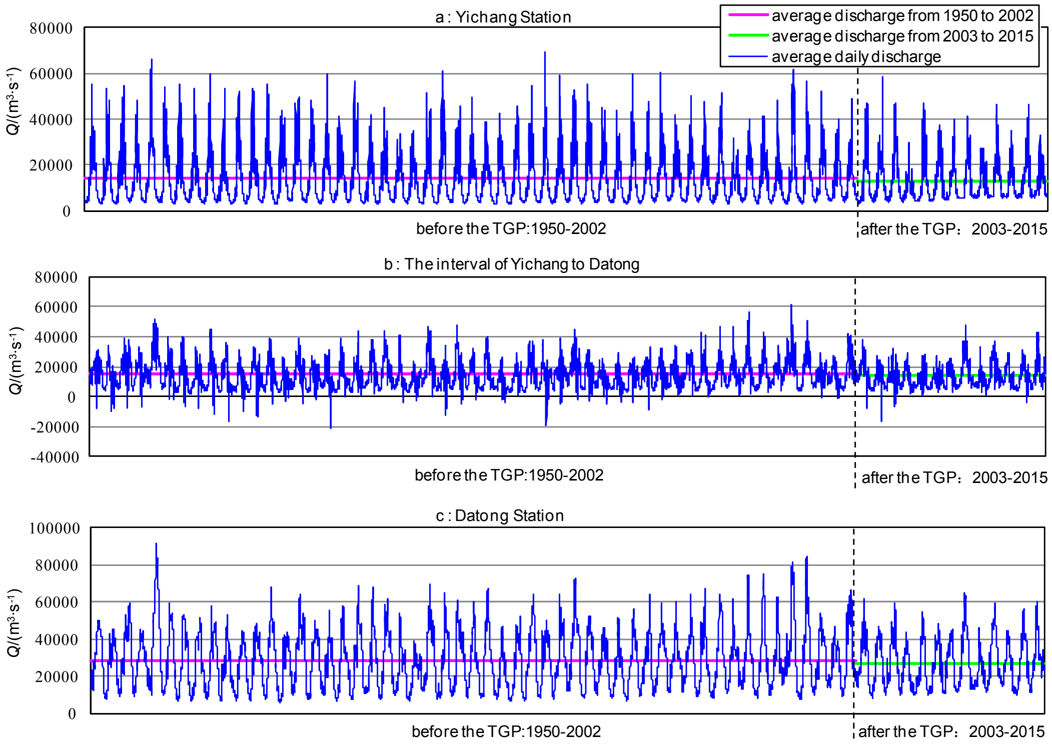

Figure 5. Average daily discharge of (a) Yichang, (b) the interval of Yichang to Datong, (c) and Datong.

4.2 Changes of monthly mean discharge at Yichang Station

As shown in Figure 6a, and 6b, the monthly mean discharge in three phases are different. Comparing to phase-1, discharge increases from January to March during phase-2, and April is almost the same as before, but decreases in other months. With the formal impounding in phase-3, the discharge increases by 39% (January), 53% (February), 43% (March), 21% (April), 8% (May) and 5% (December), and decreases by 8% (June), 11% (July), 13% (August), 19% (September), 39% (October) and 9% (November). In addition, the maximum of increased discharge is in February, and the biggest decrease takes place in September and October, which is the result of water storage.

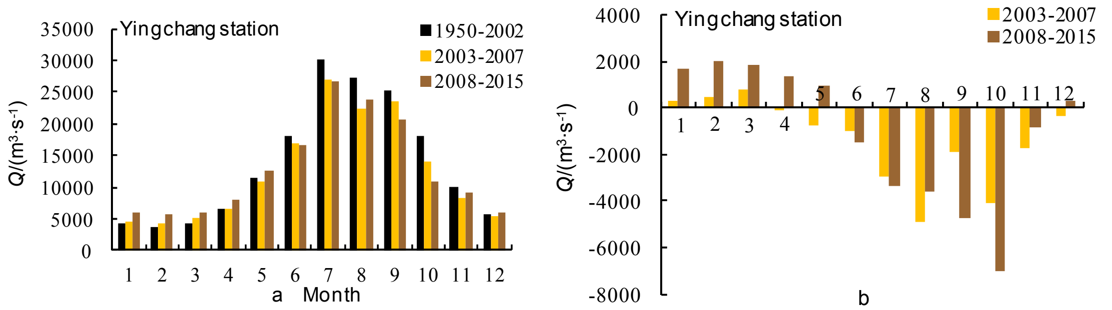

Figure 6. Change of monthly mean discharge at Yichang: (a) the monthly mean discharge in three periods (1950~2002, 2003~2007, 2008~2015), (b) the variation of monthly mean discharge compared to pre- the TGP.

4.3 Changes of monthly mean discharge at Datong Station

Influenced by TGP, the monthly mean discharge changes a lot since 2003 at Datong (see in Figure 7a, b). In phase-3, discharge increases by 20% (January), 15% (February), 20% (March), 4% (June) and 15% (December), but decreases by 2% (April), 6% (May), 9% (July), 8% (August), 14% (September), 25% (October) and 12% (November). The biggest decline also takes place in the period of impounding, September and October, and the maximums of increased discharge are in January and March. Comparing Figure 6b and Figure 7b, it reveals that the change of discharge in each month is different between Yichang and Datong.

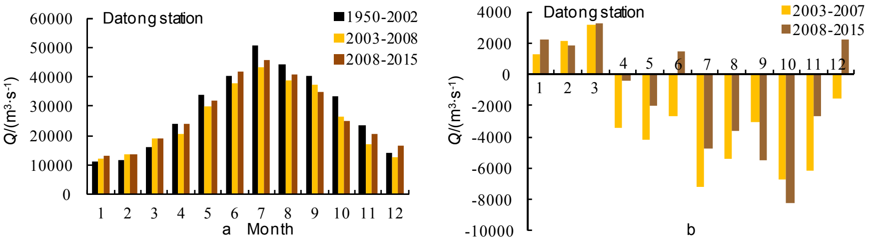

Figure 7. Change of monthly mean discharge at Datong: (a) the monthly mean discharge in three periods (1950~2002, 2003~2007, 2008~2015), (b) the variation of monthly mean discharge compared to pre- the TGP.

4.4 Changes of monthly mean discharge of the interval of Yichang to Datong

Since Datong is far away from Yichang, discharge coming from the interval influences Datong's discharge greatly. As shown in Figure 8, compared to phase-1, the discharge coming from the interval in phase-3 increases by 8% (January), 12% (March), 13% (June) and 23% (December), and keeps the same as phase-1 in August, but decreases by 3% (February), 10% (April), 13% (May), 7% (July), 5% (September), 8% (October) and 14% (November). The maximum of increased discharge is in June.

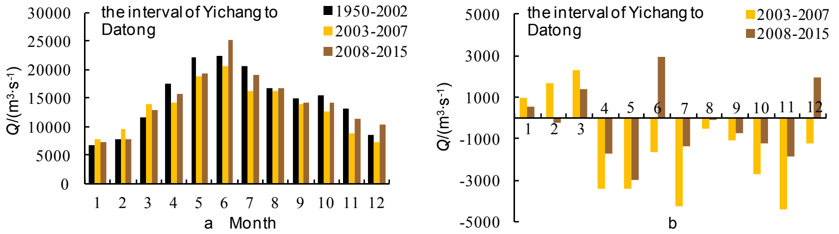

Figure 8. Change of monthly mean discharge coming from the interval of Yichang and Datong: (a) the monthly mean discharge in three periods, (b) the variation of monthly mean discharge compared to pre- the TGP.

The observed daily river discharges at Yichang and Datong show considerable discharge change during the period of phase-2 (2003~2007), and phase-3 (2008~2015), compared to phase-1 (1950~2002). (1) Due to climate change, the annual mean discharge at Yichang, Datong and the interval decline respectively by 8%, 5%, and 2%. Also, the change of discharge at Datong is mainly affected by Yichang. (2) Seasonality of discharge is still obvious, but the distribution of discharge in a year is changing with the operation of TGP. Due to the water storage in September and October, downstream runoff at Yichang and Datong decreases dramatically. Furthermore, the change of discharge at Yichang and Datong is not identical, and the reason is probably the discharge coming from the interval of Yichang to Datong.

5 DETERMINATION OF CRITICAL DISCHARGE FOR RESTRAINING SALTWATER INTRUSION

Many scholars have studied on the subject of discharge for saltwater controlling, but there exist some controversies (Mao and Shen et al., 2004; Chen and Xu et al., 2011; Chen 2014; He and Ding et al., 2006; Liu 2016). Therefore, it is necessary to determine the specific value of critical discharge for restraining saltwater intrusion by analyzing the observed data, considering previous studies.

Generally, saltwater intrusion in the Yangtze River Estuary is mostly affected by Yangtze River discharge and the external tide. As shown in Figure 9a, when the average daily discharge at Datong is lower than 30000 m^3/s, saltwater intrusion begins to occur, and exacerbates once it is less than 20000 m^3/s. With the decreasing of river discharge at Datong, the possibility of chlorinity over 250 mg/L at DFXS increases. It is figured out that chlorinity is in negative correlation with river discharge. Even under the same discharge of Datong, there are different values of chlorinity, and the reason is the change of tide. Tidal range can represent tidal intensity, and we analyzed the characteristic of tidal range at XLJ changing with lunar date (see in Figure 9b). It shows that the fluctuation pattern of tidal range has distinct regularity.

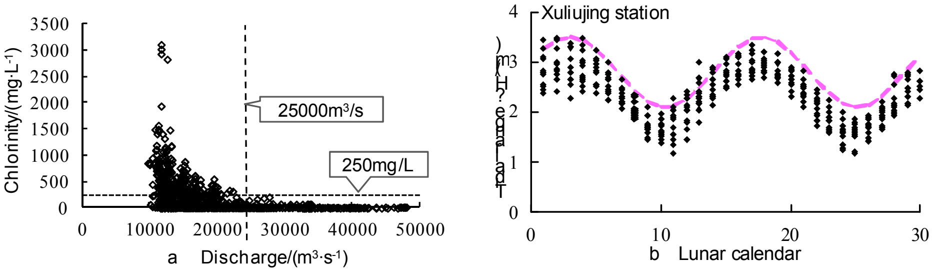

Figure 9. (a) Relationship between average daily discharge at Datong and chlorinity at Dofengxisha (DFSX), (b) change of tidal range at Xuliujing (XLJ) in 2009 with lunar calendar.

If we fixed river discharge, chlorinity is only impacted by tidal range (neglect other secondary factors). Therefore, in order to reduce the influence of discharge, we divided the discharge of Datong into many intervals (see in Figure 10). It reveals that when the discharge of Datong is in the interval of 14000~15000 m^3/s, the probability of saltwater intrusion increases to 44%, and when the discharge is in the interval of 11000~12000 m^3/s, the probability increases to 65%, and when the discharge is in the interval of <10000 m^3/s, DFXS will be in high possibility of saltwater intrusion. If we define 12000 m^3/s as the critical discharge for restraining saltwater, it means that chlorinity would be over 250 mg/L for ten days in one tidal cycle (15 days × 65% ≈ 10 days). The result is the same as the definition of severe saltwater intrusion mentioned in part-1 "Study sites and data". Thus, combining the results of other studies and our data analysis, we take 12000 m^3/s at Datong as the critical discharge for restraining saltwater after TGP.

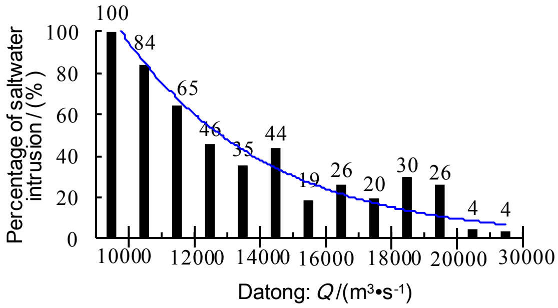

Figure 10. Possibility of chlorinity at Dongfengxisha (DFSX) over 250 mg/L in different discharge intervals.

6 DISCUSSIONS

6.1 Change of discharge at Datong and its impact on saltwater intrusion after the impoundment of the TGP

From the analysis above in section-2, the intensity of saltwater intrusion in drought season is cut down since the impounding of TGP, but the time distribution of saltwater intrusion is broader in a year, and the months of saltwater intrusion are readjusted because of the TGP. Thus, we need to find out the specific main period of time of saltwater intrusion after TGP.

As shown in Figure 11, by analyzing the probability of discharge at Datong in each month when it is less than 20000 m^3/s, 15000 m^3/s, 12000 m^3/s, and 10000 m^3/s, we can figure out that saltwater intrusion mainly concentrates on October to next year's May in phase-3 (see in Figure 11a, b), especially the period of water storage and release.

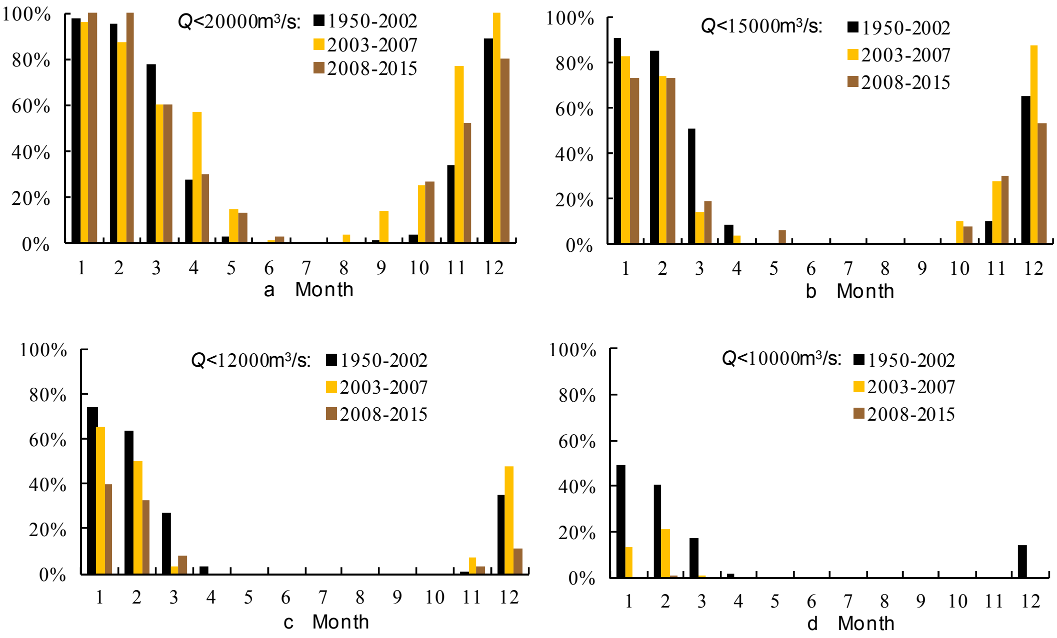

Figure 11. Probability of discharge at Datong in each month when it's less than (a)20000 m^3/s, (b)15000 m^3/s, (c)12000 m^3/s, (d)10000 m^3/s in three phases (phase-1:1950-2002; phase-2: 2003-2007; phase-3: 2008-2015).

Combining the analysis in Figure 9a that the significant saltwater intrusion in Yangtze River Estuary occurs when discharge at Datong is less than 20000 m^3/s, we marked the dates of these discharge points on the water level of TGP, as shown in Figure 12. It demonstrates that saltwater intrusion frequently occurs in the water storage and drain period of TGP since 2003.

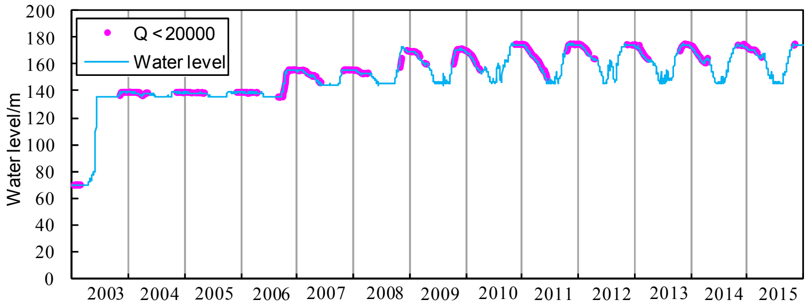

Figure 12. Water level of TGP (blue) and the point (pink) when averaged daily discharge at Datong is less than 20000 m^3/s from 2003 to 2015.

6.2 The relationship of discharge between Yichang and Datong in different periods

Comparing the multi-year monthly averaged discharge of Yichang and Datong, Figure 13 illustrates that although TGP changes the value of discharge in each month, with the peak in July cut down by 11% at Yichang and 9% at Datong, and increased by 52% at Yichang and 15% at Datong in February (see in Table 1), discharge of Datong is in concert with the change of Yichang.

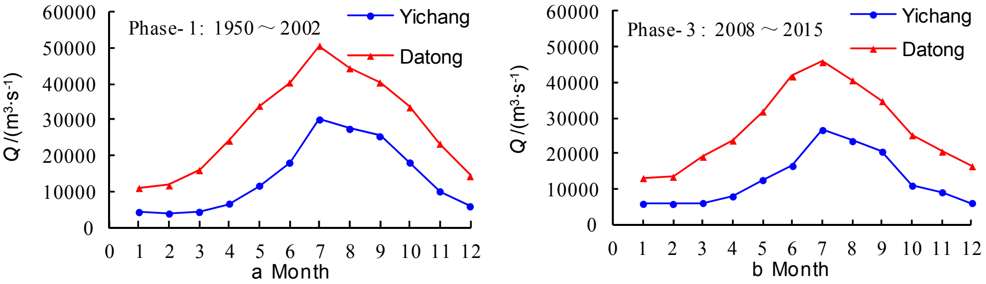

Figure 13. Multi-year monthly averaged discharge of (a) Yichang and Datong before the TGP (1950~2002), (b) after the formal impounding (2008~2015).

In section 4, we deduced that climate change has less impact on discharge of the Yangtze River, and the discharge change of Datong is mainly influenced by the TGP. The data in Table 1 shows that the discharge change of Yichang is in agreement with Datong from January to March and from June to October, and the magnitude and variation of discharge change at the two station are almost same. (1) In flood season, as we can see, the discharge change of Yichang and Datong are very close in July (Yichang: -3378 m^3/s; Datong: -4727 m^3/s), August (Yichang: -3866 m^3/s; Datong: -3594 m^3/s), September (Yichang: -4763 m^3/s; Datong: -5519 m^3/s), and November (Yichang: -7016 m^3/s; Datong: -8225 m^3/s). (2) In dry season, discharge of Datong is very sensitive to the discharge change of Yichang. The data indicate that when the discharge of Yicang increases by 5% in December, discharge of Datong increases 15%, and that is similar in January, February, and March. However, there exists some differences. For example, in January and March, both discharge at Datong increases by 20%, but it increases 39% (January) and 43% (March) at Yichang. Thus, it illustrates that the impact of discharge change at Yichang on Datong is limited. In February, when the discharge of Yichang increases by 52%, it just increases 15% at Datong. Furthermore, we need to know the reason that makes things so different.

Then, the discharge at Datong is mainly composed of two parts. One is the discharge coming from Yichang (Y) and the other is from the interval of Yichang to Datong (Y-D) (see in Figure 14a). As shown in Figure 14b and Table 2, we list the discharge proportion of Y and Y-D. It shows that the proportion of Y-D is significantly larger than Y in dry season, but less in flood season. Since saltwater intrusion of Yangtze River Estuary generally occurs in dry season, we focus on dry season. With the impounding of the TGP, the proportion of Y increases in January (+6%), February (+11%), March (+5%), April (+6%), and May (+5%), and decreases in September (-4%), October (-10%), December (-4%). On the contrary, the proportion of Y-D decreases in January (-6%), February (-11%), March (-5%), April (-6%), and May (-5%), and increases in September (+4%), October (+10%), December (+4%). Thus, it reveals that half of the discharge at Datong is from the interval of Y-D in dry season, but with the regulation of TGP, the proportion of Y increases from January to May.

/ ISSN 1562-6865 (Online) - ISSN 1063-7710 (Print)

Table 1. Multi-year monthly averaged discharge of Yichang and Datong during phase-1 and phase-3.

Month	**Yichang Hydrologic Station: $Q/(m^3 \cdot s^{-1})$**			**Month**	**Datong Hydrologic Station: $Q/(m^3 \cdot s^{-1})$**		
	1950~2002	**2008~2015**	**Change**		**1950~2002**	**2008~2015**	**Change**
1	4273	5923	1650 (+39%)	**1**	10979	13194	2215 (+20%)
2	3855	5860	2005 (+52%)	**2**	11706	13518	1812 (+15%)
3	4314	6149	1835 (+43%)	**3**	15952	19162	3210 (+20%)
4	6607	7980	1373 (+21%)	**4**	24119	23744	-375 (-2%)
5	11603	12588	985 (+8%)	**5**	33856	31878	-1978 (-6%)
6	17999	16540	-1459 (-8%)	**6**	40304	41773	1469 (+4%)
7	30024	26646	-3378 (-11%)	**7**	50540	45813	-4727 (-9%)
8	27404	23538	-3866 (-14%)	**8**	44274	40680	-3594 (-8%)
9	25341	20578	-4763 (-19%)	**9**	40332	34813	-5519 (-14%)
10	18046	11030	-7016 (-39%)	**10**	33429	25204	-8225 (-25%)
11	10021	9169	-852 (-9%)	**11**	23304	20615	-2689 (-12%)
12	5870	6136	266 (+5%)	**12**	14295	16508	2213 (+15%)

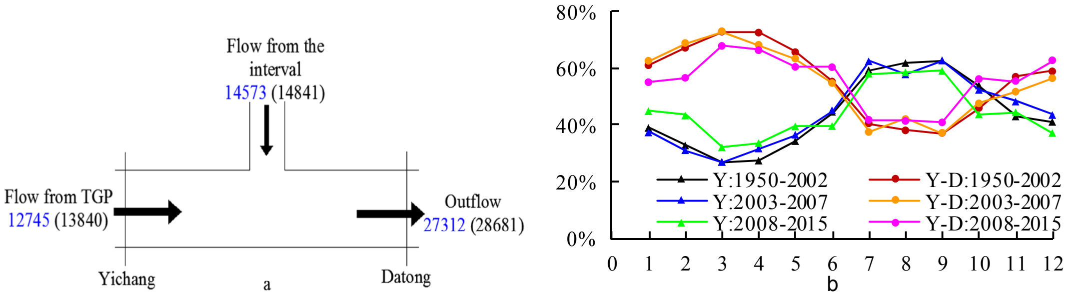

Figure 14. (a) Comparison of discharge balance items for Datong before (black: 1950~2002) and after (blue: 2008~2015) the TGP, (b) on monthly scale, the discharge proportion of Yichang (Y), and the interval of Yichang to Datong (Y-D) in each month.

Table 2. Discharge composition of Datong in three phases.

Period	**Location**	**Month**											
		1	**2**	**3**	**4**	**5**	**6**	**7**	**8**	**9**	**10**	**11**	**12**
Phase-1	A	0.39	0.33	0.27	0.27	0.34	0.45	0.59	0.62	0.63	0.54	0.43	0.41
(1950-2002)	B	0.61	0.67	0.73	0.73	0.66	0.55	0.41	0.38	0.37	0.46	0.57	0.59
Phase-2	A	0.37	0.31	0.27	0.32	0.37	0.45	0.62	0.58	0.63	0.52	0.48	0.44
(2003-2007)	B	0.63	0.69	0.73	0.68	0.63	0.55	0.38	0.42	0.37	0.48	0.52	0.56
Phase-3	A	0.45	0.43	0.32	0.34	0.39	0.40	0.58	0.59	0.59	0.44	0.44	0.37
(2008-2015)	B	0.55	0.57	0.68	0.66	0.61	0.60	0.42	0.41	0.41	0.56	0.56	0.63

A represents the discharge proportion of Yichang; B represents the discharge proportion of the interval of Yichang to Datong.

6.3 Discharge demand of saltwater intrusion control for the regulation of TGP

After getting the result of critical discharge at Datong for dampening saltwater intrusion (12000 m^3/s), we need to know how to regulate the released discharge of TGP to satisfy the demand to relieve severe saltwater intrusion. The problem is how many days the TGP needs to adjust discharge in advance, and how much discharge the TGP needs to release.

Then, we need to analyze the quantitative relationship between the averaged daily discharge at Yichang and Datong. Considering the different discharge proportion of Yichang in each month and the severe saltwater intrusion in Yangtze Estuary, we put emphasis on dry season (October to next year's May), and divide it into two cases (general case and extreme case). (1) In Figure 15, the correlation coefficient of daily discharge between Yichang and Datong is approximately 0.45. By regression analysis, we get a fitting formula, and if the discharge of Datong is 12000 m^3/s, discharge at Yichang should be at least 5778 m^3/s to avoid the severe saltwater intrusion. (2) Considering the extreme situation (the blue line in Figure 15), as saltwater intrusion mainly occurs once the discharge of Datong is below 25000 m^3/s, we extract the maximum of Yichang under different discharge of Datong. When the discharge of Datong is low, if the discharge of Datong is 12000 m^3/s, discharge at Yichang should be at least 7149 m^3/s to avoid severe saltwater intrusion.

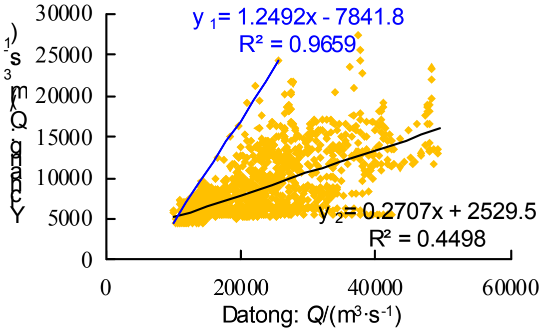

Figure 15. Relationship of daily discharge between Datong and Yichang in phase-3.

It needs about seven days for the discharge at Yichang to impact discharge at Datong by correlation analysis. According to the research of Chen (2014), it needs six days for the discharge at Datong to influence saltwater intrusion in Yangtze River Estuary. Therefore, to avoid severe saltwater intrusion, the Three Gorges Reservoir needs to release water at least thirteen days ahead.

7 CONCLUSIONS

Our findings indicate that, since the impounding of TGP, the characteristics of saltwater intrusion in the Yangtze River Estuary and the downstream discharge of TGP have considerable changes. (1) Saltwater intrusion is ahead of time, because of the water storage of TGP. The possibility of saltwater intrusion in September, October and November increases, but deceases from December to April of the next year. As the discharge of TGP increases during dry season, the peak of chlorinity reduces. Actually, the operation of TGP is helpful in avoiding extreme situation of saltwater intrusion, but it also increases the possibility of saltwater intrusion in each year. (2) Compared to the daily discharge before the TGP, seasonality of discharge is still obvious, but the distribution of discharge in a year is changing with the operation of TGP. The downstream discharges of Yichang and Datong are cut down in flood season, but increase in drought season. (3) Combining the existed studies and the observed data of chlorinity in the Yangtze River Estuary, we take 12000 m^3/s at Datong as the critical discharge for restraining saltwater after TGP. (4) By correlation analysis, to avoid serious saltwater intrusion, the Three Gorges Reservoir needs to release water at least thirteen days ahead. In general case, if the discharge of Datong is 12000 m^3/s, discharge at Yichang should be at least 5778 m^3/s to avoid the severe saltwater intrusion. In extreme situation, discharge of Yichang should be at least 7149 m^3/s to avoid the severe saltwater intrusion.

Although the discharge regulation of TGP is very important in dampening saltwater intrusion, there are many factors of saltwater intrusion, such as wind force and direction, sea level, estuarine topography, diversion projects, et cetera. Therefore, to get more accurate discharge for controlling saltwater intrusion, we still need to observe much more data in many respects.

REFERENCES

Chen, Q.J., Xu, J.Y., Zhu, J.R., Ruan, L.R., Zhao, S.W. & Tang, J.H. (2011). Determination of Critical Flow for Saline Water Intrusion into Water Source Area of Yangtze River Estuary and Guarantee Measures. *Yangtze River*, 42(18), 68-72.

Chen, L., Zhu, J.R. & Wang, B. (2013). The Statistical Model Study of Saltwater Intrusion of Chenghang Reservoir in the Yangtze Estuary. *Water & Wastewater Engineering*, 39(7), 162-165.

Chen, Z.J. (2014). Saltwater Intrusion into Water Source Zone in Yangtze Estuary in Post-Three Gorges Engineering Era and Countermeasures. *Water Resources Protection*, 30(3), 19-24.

Data of daily river discharge at Yichang and Datong from 1950 to 2015, the websites of Changjiang Water Resources Commission of the Ministry of Water Resources. Available at http://www.cjw.gov.cn/. [Accessed: 10 January 2017]

He, S.L., Ding, P.X. & Kong, Y.Z. (2006). The Change of Saltwater Intrusion in South Branch and the Saltwater Flowing into the South Branch from the North Branch in Yangtze Estuary. *Progress in Natural Science*, 16(5), 584-589.

Liu, W.P. (2016). Water Abstraction along the Yangtze River Downstream from Datong to Estuary and Its Impact on Water Discharge into Estuary, *MSc Thesis*. East China Normal University.

Mao, Z.C., Shen H.T. & Chen J.S. (2004). Measurement and Calculation of Net Salt Fluxes from the North Branch into South Branch in the Changjiang River Estuary. Oceanologia et Limnologia Sinica, 35(1), 30-34.

Savenijie, H.H.G. (1993). Predictive Model for Salt Intrusion in Estuaries. *Journal of Hydrology*, 148(1-4), 203-218.

Sun, B., Liu, S.G., Gu, J., Kuang, C.P. & Yu, W.W. (2008). Numerical Study on Impact of Water Regulation of TGP and South-to-North Water Diversion Project on Water Source Area of the Yangtze Estuary. *Yangtze River*, 39(16), 4-7.

Tang, J.H., Xu, J.Y., Zhao, W.S. & Liu, W.Y. (2011). Research on Saltwater Intrusion of the South Branch of the Changjiang Estuary Based on Measured Data. *Sources and Environment in the Yangtze Basin*, 20(6), 677-684.

Tao, Y.J., Ge, J.Z. & Ding, P.X. (2016). Design and Application of Saltwater Intrusion Forecasting System in the Yangtze Estuary. *Journal of East China Normal University (Natural Science),* (2), 128-143.

The water level and discharge data of TGP from 2003 to 2015, China Three Gorges Corporation. Available at http://www.ctgpc.com.cn/sxjt/sqqk/index.html. [Accessed: 12 January 2017].

Xiao, C.Y. & Sheng, H.T. (1998). The Analysis of Factors Affecting the Saltwater Intrusion in Changjiang Estuary. *Journal of East China Normal University* (*Natural Sciences*), (3), 74-80.

Zhao, S.W., Tang, J.H. & Xu, J.Y. (2012). Runoff Tendency of Yichang and Dating Hydrometric Stations from September to next April and A Preliminary Research on Their Runoff Relationship. *Resources and Environment in the Yangtze Basin*, 21(1), 134-139.

Zheng, X.Q., Xiao, W.J., Yu, Y. & Pan, L.Z. (2014). Statistical Prediction Study of Runoff and Tide on Changjiang River Saltwater Intrusion. *Marine Forecasts*, 31(4), 18-2.

Proceedings of the 37th IAHR World Congress
August 13 – 18, 2017, Kuala Lumpur, Malaysia

INTEGRATED NUMERICAL MODELING OF WAVE-POROUS STRUCTURE BY FINITE VOLUME METHOD (FVM)

PARAN POURTEYMOURI(1) & KOUROSH HEJAZI(2)

(1,2) Civil Engineering Department, K. N. Toosi University of Technology, Tehran, Iran
ppoorteymourie@mail.kntu.ac.ir; hejazik@kntu.ac.ir

ABSTRACT

This paper presents a non-hydrostatic two-dimensional vertical (2DV) numerical model for the simulation of wave-porous structure problems. The flow in both porous and pure fluid regions is described by the extended Navier-Stokes equations, in which the resistance to flow through a porous medium is considered by including the additional terms of drag and inertia forces. A fractional two-step projection method has been deployed to solve the governing equations in an arbitrary Lagrangian-Eulerian (ALE) description. The finite volume method (FVM) is employed to discretize the flow and transport equations, providing flexibility for defining control volumes in a staggered computational grid. The newly developed model is verified by comparing the numerical simulations with the analytical solutions of a small amplitude Stokes progressive wave and solitary wave propagation in a constant water depth shows excellent agreements for the pure fluid region. The numerical model is then employed to simulate the regular wave evolutions over a permeable rectangular submerged breakwater. The comparison of the results with the measured values reported in the literature shows good agreements of the integrated model predictions and the experimental values for free surface water displacements.

Keywords: Wave-porous structure interaction; submerged breakwater; extended navier-stokes equations; two-dimensional vertical (2DV); finite volume method (FVM).

1 INTRODUCTION

Permeable submerged (low-crested) breakwaters are widely used in coastal engineering problems for shoreline or harbor protection against wave attack and to prevent beach erosion. These underwater structures have many advantages over emerged (surface-piercing) breakwaters. Permeable submerged breakwaters provide lower construction costs, minimal impact on ship navigation, additional wave energy dissipation due to the flow friction within porous materials inside the structure, and the overtopping water generates a better water circulation and clearer seawater. Because these types of breakwaters are located beneath the sea surface and are very similar to natural reefs, they do not affect the aesthetic value of the coastal landscape. Also, fish passage through overtopping water provides more environmental benefits for local ecosystem than emerged ones.

In recent years, many numerical models have been developed to simulate the wave-porous structure problems. Sollitt and Cross (1972) studied wave interactions with a permeable breakwater of rectangular cross section. Their proposed model differs from steady Darcy law by including two additional terms of inertial and nonlinear resistance forces. Van Gent (1994) presented a one-dimensional hydraulic model coupled with a porous flow model for predicting flow properties and forces on and inside coastal permeable structures under wave motion. Sakakiyama and Kajima (1992) proposed extended Navier-Stokes equations including drag and inertia forces components to simulate the wave transformation interacting with a permeable breakwater. Huang et al. (2003) developed a numerical model to study the solitary wave interaction with a permeable submerged breakwater using two-dimensional Navier-Stokes type model equations for porous flows which were obtained by preserving the adjective and the viscous stress terms into the equations proposed by Sollitt and Cross (1972). Losada et al. (1997) conducted a set of experiments to investigate the porosity effect on the evolution of periodic waves propagating over a submerged breakwater under non-breaking conditions. Wu and Hsiao (2013) used a two-dimensional volume averaged Reynolds averaged Navier-Stokes model and laboratory experiments based on the particle image velocimetry (PIV) technique to investigate free surface evolutions and velocity fields around a submerged permeable breakwater under non-breaking solitary wave forcing. Hur et al. (2011) investigated the effect of the slope gradient of submerged breakwaters on the wave fields using modified Navier-Stokes equations proposed by Hur and Mizutani (2003).

In this study, a non-hydrostatic numerical model presented by Hejazi et al. (2013) has been deployed and the model has been further developed to simulate the wave force action on a porous structure. In the numerical model, the flow motion in both pure fluid region and inside the porous medium is described by the two-dimensional extended Navier-Stokes equations while the effect of the porous medium is considered in terms of drag and inertia forces. The results from the newly developed numerical model are compared with

/ ISSN 1562-6865 (Online) - ISSN 1063-7710 (Print)

analytical solutions to demonstrate the validity of the model. The model is also employed to study the non-breaking regular wave evolutions overtopping a permeable rectangular submerged breakwater.

2 GOVERNING EQUATIONS

The two-dimensional extended Navier-Stokes equations proposed by Sakakiyama and Kajima (1992) were adopted to describe the flow motion in both porous and pure fluid regions. The fluid resistance in porous medium was considered by including the components of drag and inertia forces into the conventional continuity and Navier-Stokes equations. The extended continuity and Navier-Stokes equations in their conservative ALE form are expressed as follows:

$$\frac{\partial(\gamma_x u)}{\partial x}+\frac{\partial(\gamma_z w)}{\partial z}=0 \qquad [1]$$

$$\lambda_v\frac{\partial u}{\partial t}+\frac{\partial(\lambda_x u^2)}{\partial x}+\frac{\partial(\lambda_z uw)}{\partial z}=-\gamma_v\frac{\partial p^*}{\partial x}+\frac{\partial}{\partial x}(\gamma_x \nu_T\frac{\partial u}{\partial x})+\frac{\partial}{\partial z}(\gamma_z \nu_T\frac{\partial u}{\partial z})-(\frac{\rho}{\rho_r})R_x \qquad [2]$$

$$\lambda_v\frac{\partial w}{\partial t}+\frac{\partial(\lambda_x wu)}{\partial x}+\frac{\partial(\lambda_z w^2)}{\partial z}=-\gamma_v\frac{\partial p^*}{\partial z}+\frac{\partial}{\partial x}(\gamma_x \nu_T\frac{\partial w}{\partial x})+\frac{\partial}{\partial z}(\gamma_z \nu_T\frac{\partial w}{\partial z})-\gamma_v(\frac{\rho-\rho_r}{\rho_r})g-(\frac{\rho}{\rho_r})R_z \qquad [3]$$

where *u* and *w* are the horizontal and vertical velocity components in the Cartesian coordinate system (*x*,*y*), *t* is the time, *g* is the gravitational acceleration, *ρ* is the local density, ν_T is the turbulent dynamic viscosity, p^* is defined as $\Delta p/\rho_r$; where Δp is the dynamic pressure which equals the reduction of the hydrostatic pressure from the total instantaneous pressure $(\Delta p = p_t - p_g)$, ρ_r is the reference density, γ_v is the volume porosity, and γ_x and γ_z are the components of surface porosity in the *x* and *z* directions, respectively. The parameters λ_v, λ_x and λ_z are defined as follows:

$$\lambda_i=\gamma_i+(1-\gamma_v)C_M \qquad [4]$$

where C_M denotes the inertia coefficient. The variables, R_x and R_z in Equation. [2 and 3] represent the horizontal and vertical drag force components and are modeled by the following equations (Sakakiyama and Kajima, 1992):

$$R_x=\frac{1}{2}\frac{C_D}{\Delta x}(1-\gamma_x)u\sqrt{u^2+w^2} \qquad [5]$$

$$R_z=\frac{1}{2}\frac{C_D}{\Delta z}(1-\gamma_z)w\sqrt{u^2+w^2} \qquad [6]$$

where C_D is the drag coefficient.

3 STAGGERED GRID SYSTEM IN ALE DESCRIPTION

Finite volume method (FVM) with a non-orthogonal curvilinear staggered grid system in an arbitrary Lagrangian-Eulerian (ALE) description had been deployed for the computational discretization of the governing equations. In ALE description, each individual node on the boundaries and interfaces of the computational mesh may be followed by the associated fluid particle to precisely track the boundaries and interfaces, while the nodes of the computational mesh inside the domain can move in an arbitrary manner to optimize the shapes of volumes. Therefore, the ALE description accommodates significant distortions of the computational mesh than would be allowed by a purely Lagrangian method and preserves more flexible geometry than that afforded by a purely Eulerian approach. The configuration of the staggered mesh, the locations of the scalar and vector quantities and their associated control volumes on the vertical *x-z* reference plane are illustrated in Figure 1. The computational domain consists of a constant number of vertical layers, where scalar variables including pressure, density and dynamic viscosity were defined at the cell centers and the velocity components were defined at the faces of each control volume. The bed level and water surface elevation were considered to be given and calculated at the center of the lower and upper side of the corresponding volumes of the water columns, respectively.

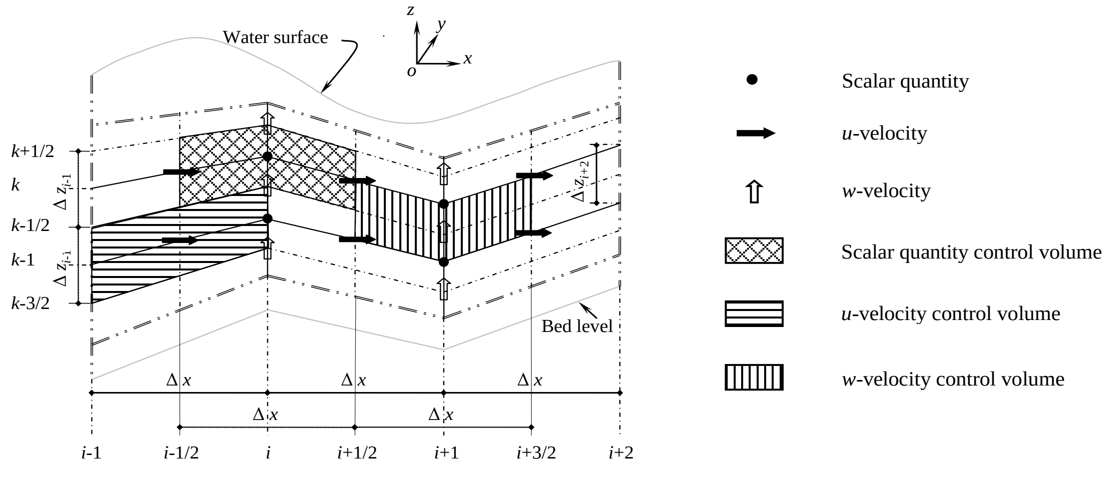

Figure 1. Grid configuration, locations of the scalar and vector variables and their control volumes on the vertical *x-z* reference plane.

The volume porosity (γ_v) and the surface porosities (γ_x, γ_z) are located at the center and the faces of each computational cell in the *x* and *z* directions, respectively as shown in Figure 2, and are calculated by the fraction of the cell open to fluid and the total porosity of porous medium after each time step as indicated in Eq. [7 and 8].

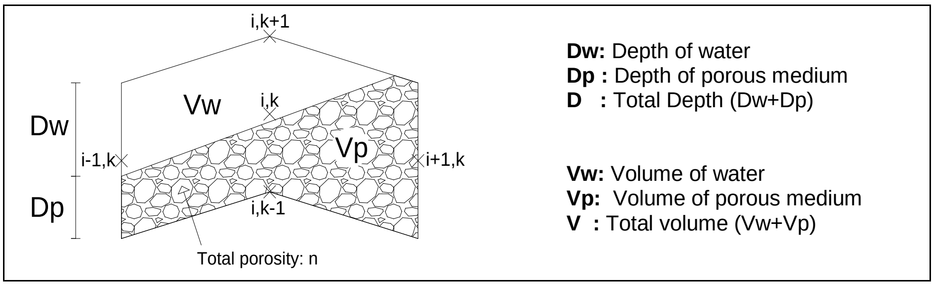

Figure 2. Definition of the volume and surface porosities of each computational cell.

$$(\gamma_x)_{i-1,k} = \frac{D_w}{D} + n\frac{D_p}{D} \qquad [7]$$

$$(\gamma_v)_{i,k} = \frac{V_w}{V} + n\frac{V_p}{V} \qquad [8]$$

The arrangement illustrated in Figure 2 shows that for a control volume full of porous medium the volume and surface porosities are equal to total porosity ($\gamma_v = \gamma_x = \gamma_z = n$), while for a control volume full of water the volume and surface porosities are set to one ($\gamma_v = \gamma_x = \gamma_z = 1$).

4 NUMERICAL SOLUTION

4.1 Solution method

A projection method was utilized to discretize the extended Navier-Stokes equations in two major fractional time steps. In the first step, the momentum equations, in the absence of pressure field, were solved to compute an intermediate velocity (u^* and w^*) which did not satisfy the continuity constraint. The first step was further split into three fractional steps which allowed the use of most suitable approximations for advective, diffusive and drag force components as follows:

$$\lambda_v \frac{u^* - u^n}{\Delta t} + \frac{\partial(\lambda_x u^2)}{\partial x} + \frac{\partial(\lambda_z uw)}{\partial z} = \frac{\partial}{\partial x}(\gamma_x \nu_T \frac{\partial u}{\partial x}) + \frac{\partial}{\partial z}(\gamma_z \nu_T \frac{\partial u}{\partial z}) - (\frac{\rho}{\rho_r})R_x \qquad [9]$$

$$\lambda_v \frac{w^* - w^n}{\Delta t} + \frac{\partial(\lambda_x wu)}{\partial x} + \frac{\partial(\lambda_z w^2)}{\partial z} = \frac{\partial}{\partial x}(\gamma_x \nu_T \frac{\partial w}{\partial x}) + \frac{\partial}{\partial z}(\gamma_z \nu_T \frac{\partial w}{\partial z}) - (\frac{\rho}{\rho_r})R_z \qquad [10]$$

Advective fluxes were determined by a fifth-order-accurate numerical scheme and the Crank-Nicholson method was deployed to solve the diffusive terms of transport equation.

The second fractional step consisted of bringing the pressure terms, back into the equations and calculating the pressure field by solving the extended continuity equation and the momentum equations excluding advective and diffusive terms and drag force components as follows:

$$\frac{\partial(\gamma_x u^{n+1})}{\partial x} + \frac{\partial(\gamma_z w^{n+1})}{\partial z} = 0 \qquad [11]$$

$$\lambda_v \frac{u^{n+1} - u^*}{\Delta t} = -\gamma_v \left(\varphi \left(\frac{\partial p^*}{\partial x} \right)^{n+1} + (1-\varphi) \left(\frac{\partial p^*}{\partial x} \right)^n \right) \qquad [12]$$

$$\lambda_v \frac{w^{n+1} - w^*}{\Delta t} = -\gamma_v \left(\varphi \left(\frac{\partial p^*}{\partial z} \right)^{n+1} + (1-\varphi) \left(\frac{\partial p^*}{\partial z} \right)^n \right) \qquad [13]$$

φ is the implicit weighting factor, where $\varphi = 1$ presents a fully implicit solution and $\varphi = 0$ provides a fully explicit solution. The Gauss divergence theorem was adopted for computing the pressure derivatives on the horizontal and vertical velocity locations. Substituting approximations of the pressure derivatives into Eqs. [12 and 13], and subject to the continuity constraint, Eq. [11], the pressure Poisson equation was obtained. The solution of the pressure Poisson equation led to a linear system of equations in the form of a block tri-diagonal matrix with the pressures as unknowns. The pressure for each computational cell was obtained by solving the block tri-diagonal matrix with a direct solver of Thomas algorithm where the second step was then completed by computing the updated velocity values, u^{n+1} and w^{n+1}, from the Eqs. [12 and 13].

4.2 Free surface treatment

The free surface equation was obtained by integrating the continuity equation over the entire water column with the kinematic boundary conditions at the impermeable bed and free surface, as follows:

$$\frac{\partial \eta}{\partial t} - \frac{\partial z_b}{\partial t} + \frac{\partial}{\partial x} \int_{z_b}^{\eta} \gamma_x u dz = 0 \qquad [14]$$

where η is the free surface elevation above mean water level and z_b is the bed elevation above the reference datum. The mass continuity for the *i*th column may be written in the following form:

$$\frac{\eta_i^{n+1} - \eta_i^n}{\Delta t} + \frac{1}{\Delta x} \sum_{k=1}^{nk} \left[\gamma_{x_{i+1,k}} u_{i+1,k}^{n+1} \Delta z_{i+1} - \gamma_{x_{i-1,k}} u_{i-1,k}^{n+1} \Delta z_{i-1} \right] = 0 \qquad [15]$$

where *nk* is the number of layers. Substituting Eq. [12] into Eq. [15] gives the pressure equation of the upper layer. Therefore the new free surface elevation was computed at each time step and the mesh was then regenerated.

4.3 Boundary conditions

In the present numerical model, two types of boundary conditions, namely Dirichlet and Neumann boundary conditions were required to solve the governing equations. The Dirichlet boundary condition was set to zero for normal velocities at impermeable bottom (Eq. 16) and the Neumann boundary condition was assumed zero for normal gradient of the tangential velocities at impermeable bed and the left side of the computational domain (Eq. [17]). At open boundaries, where required, by setting the dynamic pressure equal to zero at the end of the numerical domain, a free exit for the water was considered.

$$w\big|_{z=0} = 0 \qquad [16]$$

$$\left.\frac{\partial u}{\partial z}\right|_{z=0} = 0 \quad \text{and} \quad \left.\frac{\partial w}{\partial x}\right|_{x=0} = 0 \qquad [17]$$

5 RESULTS AND DISCUSSIONS

Firstly, the validation of the newly developed model in the absence of porous medium was confirmed by comparing the evolution of the numerical and analytical wave heights of a Stokes progressive wave and a solitary wave propagating in a constant water depth. If the volume and surface porosities are set to one $(\gamma_v = \gamma_x = \gamma_z = 1)$, the governing equations become identical to the conventional Navier-Stokes equations for flow in pure fluid region. This may be used for the verification of the proposed model which is presented in next sections. After verifying the accuracy of the numerical model for pure fluid region, the regular wave evolutions over permeable rectangular submerged breakwater under non-breaking conditions was investigated and discussed.

5.1 Stokes progressive wave in deep water

The capability of the model for predicting the transformation of an in viscid non-linear wave train in deep water, is presented herein. A progressive wave with a wave height of *H*=0.5 m and a wave period of *T*=5 s propagates in a constant water depth of *h*=15 m. The computational domain with the length of *L*=1500 m was discretized with horizontal grid size of Δ*x*=1 m in the *x*-direction and 15 layers in the *z*-direction. A time step of Δ*t*=0.05 s was used and the simulation was carried out for 140 seconds. The water surface displacement and the velocity components under the second-order stokes wave are given analytically as follows (Dean and Dalrymple, 1991):

$$\eta = \frac{H}{2}\cos\left(kx - \sigma t\right) + \frac{H^2 k}{16}\frac{\cosh kh}{\sinh^3 kh}(2 + \cosh 2kh)\cos 2(kx - \sigma t) \qquad [18]$$

$$u = \frac{Hgk}{2\sigma}\frac{\cosh kz}{\cosh kh}\cos(kx - \sigma t) + \frac{3H^2\sigma k}{16}\frac{\cosh 2kz}{\sinh^4 kh}\cos 2(kx - \sigma t) \qquad [19]$$

$$w = \frac{Hgk}{2\sigma}\frac{\sinh kz}{\cosh kh}\sin(kx - \sigma t) + \frac{3H^2\sigma k}{16}\frac{\sinh 2kz}{\sinh^4 kh}\sin 2(kx - \sigma t) \qquad [20]$$

where *z* is the elevation above the datum, *σ=2π/T* is the angular frequency of the wave, *k=2π/L* is the wave number and *L* is the wave length. For second order Stokes waves, the linear dispersion equation relating *σ* to *k* remains valid, giving a wave number equal to *k*=0.16344 rad/m and the celerity of the wave *c=L/T= σ/k* was calculated to be 7.689 m/s. Figure 3 compares the numerically predicted free surface elevation with the analytical solution after 140 seconds.

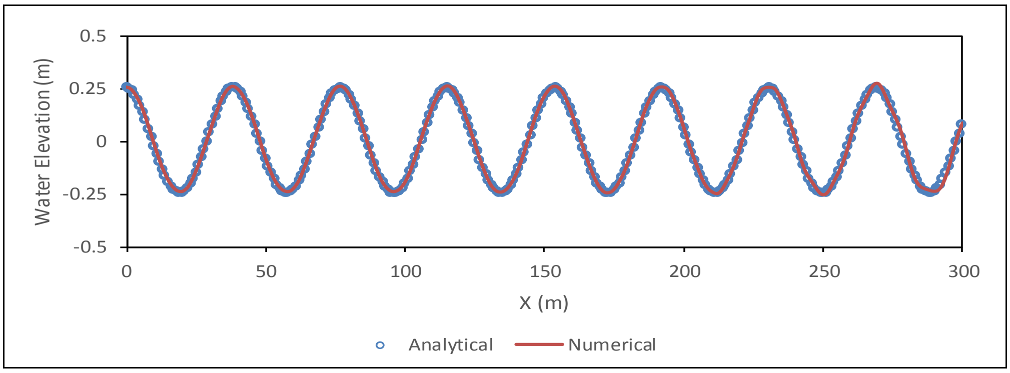

Figure 3. Comparison of the free surface elevation between numerical model predictions and analytical solution for a progressive wave train in deep water at *t*=140 s.

5.2 Solitary wave propagation in a constant water depth

The solitary wave height was *H*=1 m and the constant water depth was considered to be *h*=10 m. The computational domain consisted of 1000 grid cells equal to Δ*x*=2 m and 10 vertical layers. The calculations were performed with time intervals of Δ*t*=0.1 s within a total simulation time of 180 seconds. By application of the Boussinesq theorem of solitary waves for velocity components at upstream boundary and assuming the left inflow boundary to be at *x*=-300 m, the free surface will start at the highest point of the desired solitary wave. For an in viscid flow, the analytical solitary wave profile and velocity components derived from the Boussinesq equations are given as follows (Lee et al., 1982):

$$\eta = H\,\mathrm{sech}^2\left(\sqrt{\frac{3}{4}\frac{H}{h^3}}X\right) \quad ; \quad X=(x-ct) \qquad [21]$$

$$u=\sqrt{gh}\,\frac{\eta}{h}\left[1-\frac{1}{4}\frac{\eta}{h}+\frac{h}{3}\frac{h}{\eta}\left(1-\frac{3}{2}\frac{z^2}{h^2}\right)\frac{d^2\eta}{dX^2}\right] \qquad [22]$$

$$w=-\sqrt{gh}\,\frac{z}{h}\left[\left(1-\frac{1}{2}\frac{\eta}{h}\right)\frac{d\eta}{dX}+\frac{1}{3}h^2\left(1-\frac{1}{2}\frac{z^2}{h^2}\right)\frac{d^3\eta}{dX^3}\right] \qquad [23]$$

where z is the elevation above reference datum and $c=\sqrt{g(h+H)}$ is the solitary wave celerity; approximately equal to 10.388 m/s. The comparisons between computational results and analytical solutions for free surface elevation and velocity components are illustrated in Figures 4 and 5, respectively. The numerical results were almost identical with the analytical solutions, confirming the capability of the present numerical model to correctly simulate the solitary wave propagation in a constant water depth.

5.3 Regular wave propagation over a permeable submerged breakwater

Regular wave evolutions over a permeable rectangular submerged breakwater under non-breaking conditions were simulated for the validation of the new integrated model. The numerical results were compared with the experimental measurements of Losada et al. (1997). The experiments were conducted in a wave flume of 69 m long, 2 m high and 2 m wide. The permeable submerged breakwater was reported to be 0.8 m long, 0.385 m high and 1 m wide, and was located at a distance of 44 m from the wave maker. The porous materials were stone with a mean grain size of D_{50}=2.09 cm and a porosity of *n*=0.521. The incident Stokes waves with wave period of *T*=1.8 s and wave height of *H*=4.29 cm propagated in a constant water depth of *h*=0.475 m. A schematic diagram of the numerical wave tank used in this study is shown in Figure 6. The computational domain was discretized by Δ*x*=0.04 m grids and 25 layers in the horizontal and vertical directions, respectively. The time step was set Δ*t*=0.001 s and the simulation advanced for *t*=120 seconds. Inertia and drag force coefficients in the governing equations were determined to be C_M =0.5 and C_D =3, from a series of numerical calibrations against available experimental measurements for free surface elevations. The front wall of the submerged breakwater was considered to be located at *x*=0, and the time histories of free surface water displacements were recorded at positions *x*=-4, 4, 44 and 68 cm. The comparisons between the numerical results and the experimental measurements reported by Losada et al. (1997) are illustrated in Figure 7.

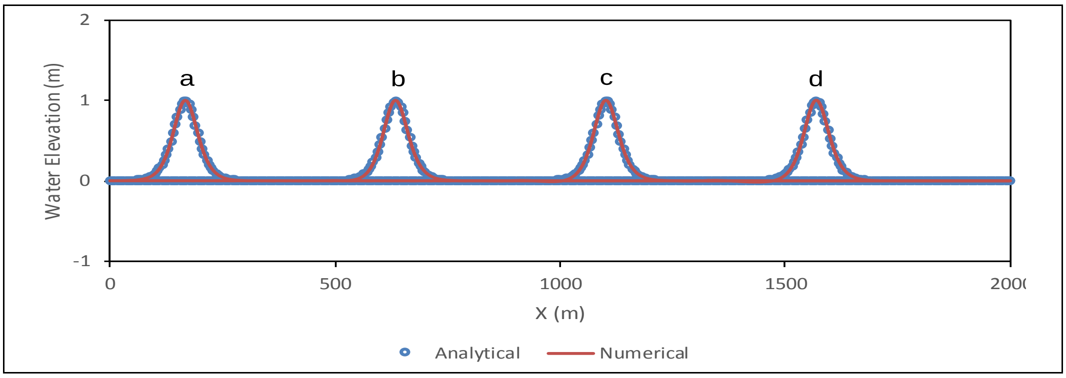

Figure 4. Comparison of water elevations between numerical results and analytical solutions for a solitary wave propagation in a constant water depth at times equal to *a*) *t*=45 s, *b*) *t*=90 s, *c*) *t*=135 s and *d*) *t*=180 s.

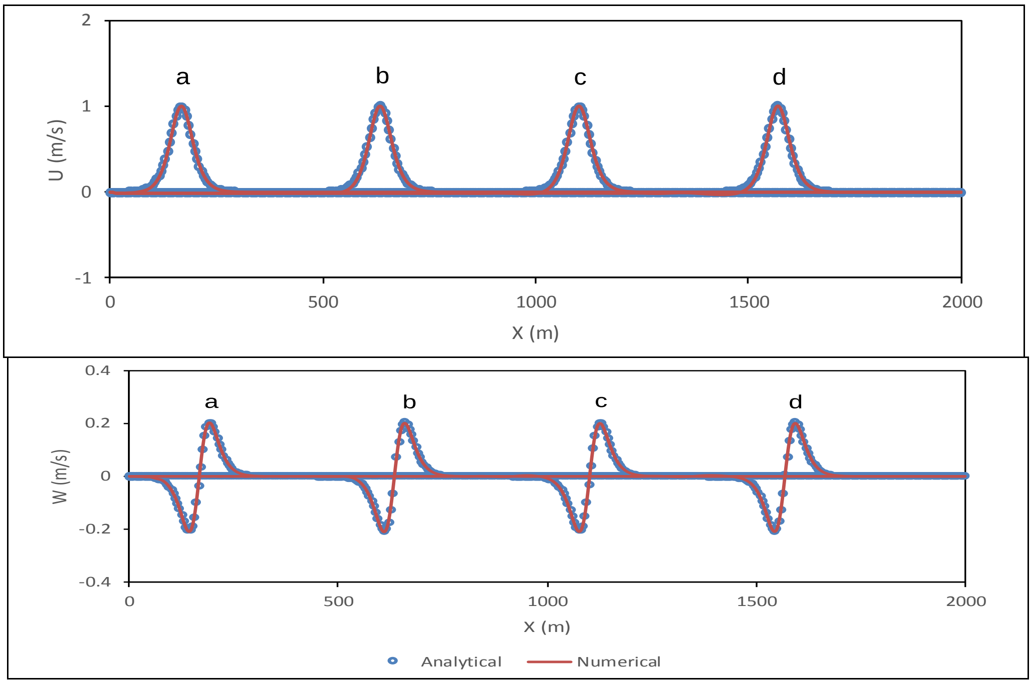

Figure 5. Comparison of velocity components between numerical results and analytical solutions for a solitary wave propagation in a constant water depth at times equal to *a*) *t*=45 s, *b*) *t*=90 s, *c*) *t*=135 s and *d*) *t*=180 s.

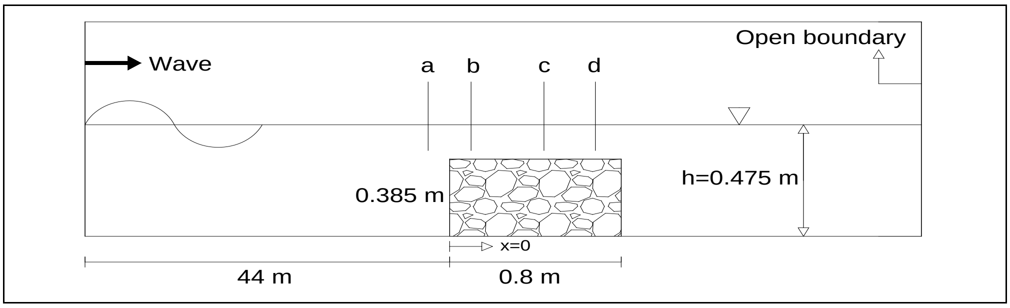

Figure 6. Sketch of the numerical wave tank.

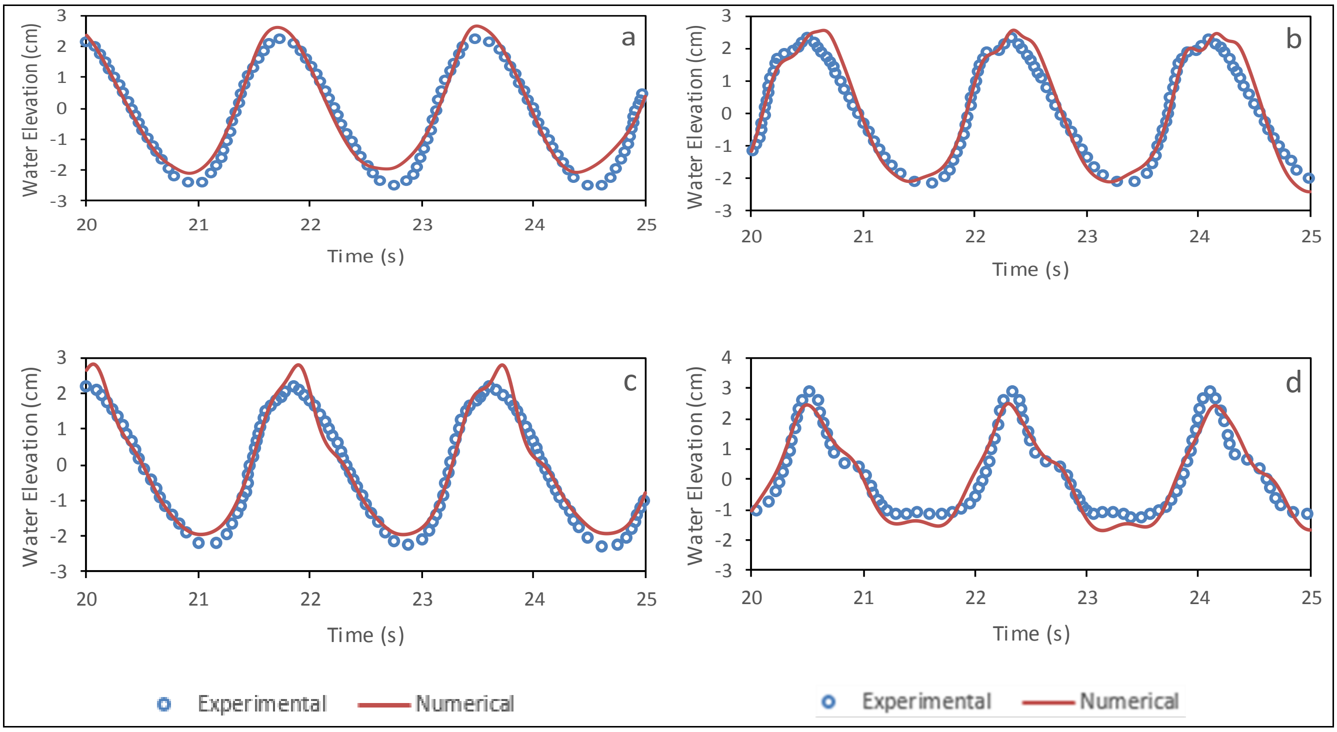

Figure 7. Time histories of the numerical free surface elevations compared with experimental measurements at positions *a*) *x*=-4 cm, *b*) *x*=4 cm, *c*) *x*=44 cm and *d*) *x*=68 cm.

As shown in Figure 7, the newly developed model predictions present good agreements with the experimental measurements of the free surface water displacements.

Figure 8 shows numerical snapshot of free surface elevation and velocity field, and velocity profiles from *x*=-0.4 m to *x*=1.2 m with an interval of 0.2 m. At the same time, the Stokes wave passes over the permeable submerged breakwater, where x=0 indicates the leading edge of the breakwater. Based on the numerical results, when the Stokes wave front reaches the offshore side of the submerged breakwater, due to the hydraulic jump formation, the flow was separated from the top of the obstacle and a small counter-clockwise vortex was generated at the leading edge of the breakwater. As the wave passes over the breakwater, the primary vortex grows in size and penetrates into the deeper layers of water. It was also seen that, due to the drag and inertia resistance forces of the porous medium, the velocity inside the permeable breakwater was noticeably smaller than that on the top of the breakwater. Velocity profiles also demonstrate that the velocity at the onshore side of the breakwater was smaller than the velocity inside the breakwater, which was due to the energy dissipation through porous medium.

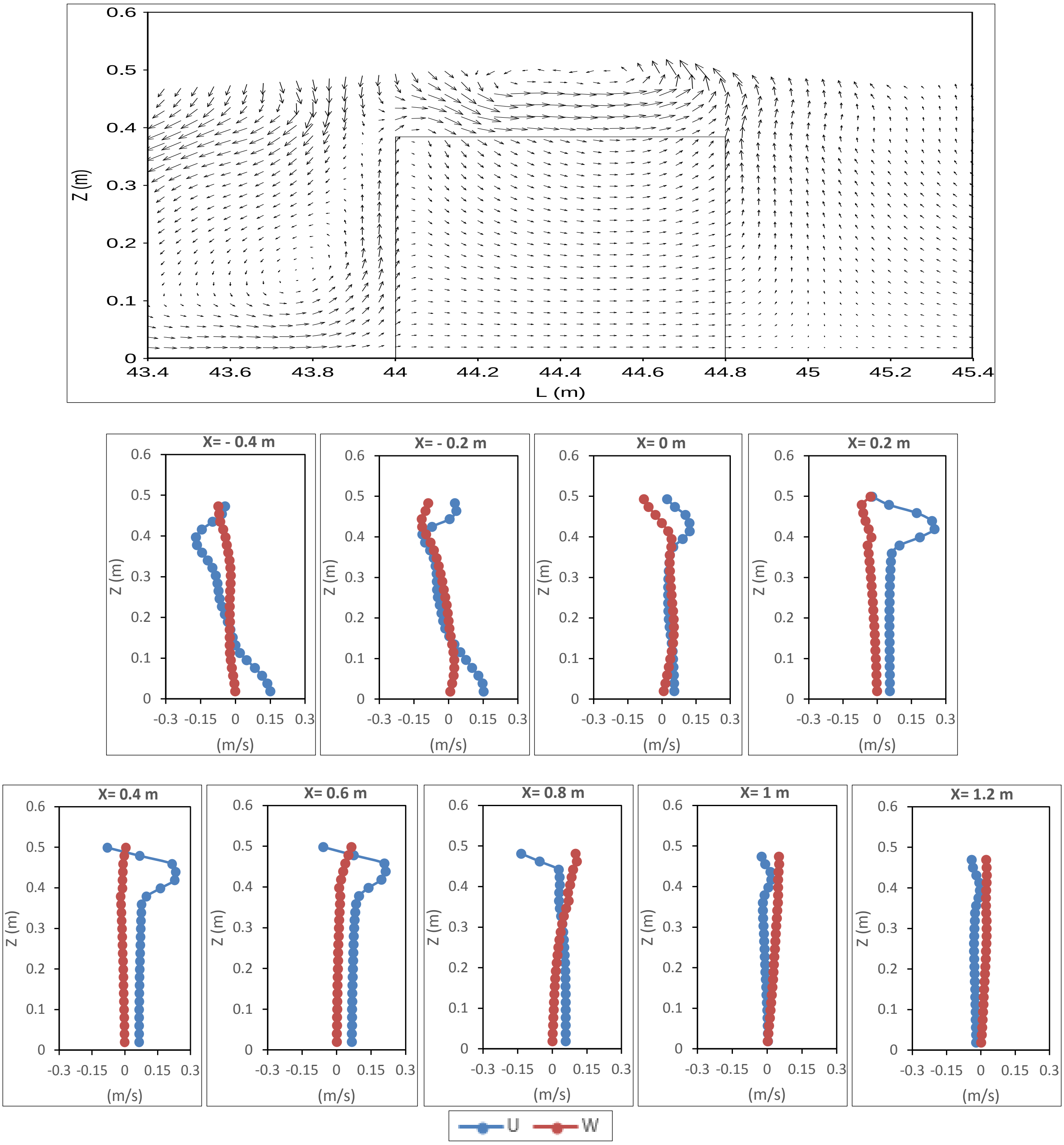

Figure 8. Simulated free surface elevation and velocity field, and horizontal and vertical velocity profiles before, inside and after the submerged breakwater, when the Stokes wave passes over the breakwater.

6 CONCLUSIONS

In this paper, the two-dimensional vertical (2DV) extended Navier-Stokes equations with non-hydrostatic pressure distribution were solved numerically in both porous and pure fluid regions to simulate wave-porous structure problems. The resistance to flow through a porous medium is considered in terms of additional drag and inertia forces in the governing equations. Application of a fractional two-step method to extended Navier-Stokes equations, led to the solution of the pressure Poisson equation in the form of a block tri-diagonal matrix with the pressures as unknowns. A direct double sweep algorithm is used to solve the block tri-diagonal matrix and the finite volume method in an arbitrary Lagrangian-Eulerian (ALE) description is employed to discretize the governing equations. The volume and surface porosity components at each computational cell are calculated by considering the portion of cells open to fluid and the total porosity of a porous medium and updating the porosity values at each time-step. The newly developed model in the absence of the porous medium is validated against the analytical solutions of a Stokes progressive wave train in deep water. Solitary wave propagation in a constant water depth, confirmed the accuracy of the model for the pure fluid region. The model was then employed to investigate the regular wave evolutions over permeable rectangular submerged breakwater under non-breaking conditions. Comparisons between numerical results and experimental measurements showed the capability of the integrated numerical model to simulate the wave-porous structure problems.

REFERENCES

Dean, R.G. & Dalrymple, R.A. (1991). W*ater Wave Mechanics for Engineers and Scientists* (Vol. 2). World Scientific Publishing Co Inc, 1-368.

Hejazi, K., Soltanpour, M. & Sami, S. (2013). Numerical Modeling of Wave–Mud Interaction Using Projection Method. *Ocean Dynamics*, 63(9-10), 1093-1111.

Huang, C.J., Chang, H.H. & Hwung, H.H. (2003). Structural Permeability Effects on the Interaction of a Solitary Wave and a Submerged Breakwater. *Coastal engineering*, 49(1), 1-24.

Hur, D.S., Lee, K.H. & Choi, D.S. (2011). Effect of the Slope Gradient of Submerged Breakwaters on Wave Energy Dissipation. *Engineering Applications of Computational Fluid Mechanics*, 5(1), 83-98.

Hur, D.S. & Mizutani, N. (2003). Numerical Estimation of the Wave Forces Acting on a Three-Dimensional Body on Submerged Breakwater. *Coastal Engineering*, 47(3), 329-345.

Lee, J.J., Skjelbreia, J.E. & Raichlen, F. (1982). Measurement of Velocities in Solitary Waves. *Journal of the Waterway Port Coastal and Ocean Division*, 108(2), 200-218.

Losada, I.J., Patterson, M.D. & Losada, M.A. (1997). Harmonic Generation Past a Submerged Porous Step. *Coastal Engineering*, 31(1-4), 281-304.

Sakakiyama, T. & Kajima, R. (1992). Numerical Simulation of Nonlinear Wave Interacting with Permeable Breakwaters. *Coastal Engineering Proceedings*, 1(23).

Sollitt, C.K. & Cross, R.H. (1972). Wave Transmission Through Permeable Breakwaters. *Coastal Engineering Proceedings*, 1(13).

van Gent, M.R. (1994). The Modelling of Wave Action on and in Coastal Structures. *Coastal Engineering*, 22(3-4), 311-339.

Wu, Y.T. & Hsiao, S.C. (2013). Propagation of Solitary Waves over a Submerged Permeable Breakwater. *Coastal Engineering*, 81, 1-18.

/ ISSN 1562-6865 (Online) - ISSN 1063-7710 (Print)

Proceedings of the 37th IAHR World Congress
August 13 – 18, 2017, Kuala Lumpur, Malaysia

SPH MODELING OF TSUNAMI PROPAGATION AND HIGHEST RUN-UP: CASE STUDY - OKUSHIRI ISLAND TSUNAMI

AHMED M. ABDELRAZEK(1), ICHIRO KIMURA(2) & YASUYUKI SHIMIZU(3)

(1,2,3) Hydraulic Research Laboratory, Graduate School of Engineering, Hokkaido University, Japan,
(1) Irrigation Eng. & Hydraulic Department, Faculty of Engineering, Alexandria University, Egypt,
ahmedmrazek@yahoo.com; i-kimu2@eng.hokudai.ac.jp; yasu@eng.hokudai.ac.jp

ABSTRACT

This paper discusses the advantages of the smoothed particle hydrodynamics (SPH) method based on shallow water equation (SWE) to simulate flood inundation owing to rapidly varying flow, such as dam breaks and tsunamis. The open boundary condition with buffer zones at the inflow and outflow boundaries using Riemann invariants was implemented in the SPH-SWE model. The SPH-based SWE model is used to simulate the laboratory observations of the 1993 Okushiri Tsunami. The numerical results obtained from the SPH model are compared with the experimental data. The comparisons indicated that the model has the capability to simulate free-surface flows in areas with complicated bathymetry and irregular coastline.

Keywords: Hydrodynamics; SPH method; okushiri tsunami; shallow water; simulation.

1 INTRODUCTION

Flood events have caused huge damages to human health, environment, and infrastructures. In particular, tsunami induced coastal floods are heavily represented as both the deadliest flood events and costliest disasters ever.

In order to reduce such damages, and construct effective protection structures economically, it is important to establish an effective prediction method for analyzing the tsunami in order to predict the occurrence conditions, flow behavior and the maximum run-up.

Due to the advent of computer technology and numerical methods, numerical models have been widely used in modeling and predictions of various phenomena in the ocean, such as tsunamis.

There are several models that have achieved a significant level of succeeding in solving such kind of problems; most of them are mesh-based numerical model. The main advantage of the mesh-based numerical models is its computational efficiency and it is easy to treat the solid and open boundaries. However, these kinds of models have significant disadvantages due to the use of mesh. For example, the connectivity of the mesh can be difficult to maintain over complicated geometries and regions with deformable boundaries.

Recently a new class of numerical methods has been developed called mesh-free methods. Mesh-free methods do not require Eulerian grids and they deal with a number of particles in a Lagrangian framework. They are considered to be more effective than traditional methods in dealing with problems involving large deformations. The key idea of these methods is to provide an accurate and a stable numerical solution of the partial differential equations using a set of distributed particles in the domain without using any grid. Many mesh-free methods have been developed in the last decades, among these methods; the Smoothed Particle Hydrodynamics (SPH) method is widely used.

SPH method is a mesh-free Lagrangian particle method. It was originally invented to solve astrophysical problems (Lucy, 1977; Gingold and Monaghan, 1977); then it has been extended to solve a huge range of applications such as, the dynamic response of material strength (Libersky and Petschek, 1991), free surface fluid flow (Monaghan, 1994; Abdelrazek et al., 2014), incompressible fluid flow (Cummins and Rudman, 1999; Gotoh et al., 2014), multi-phase flow (Monaghan and Kocharyan, 1995), turbulence flow (Monaghan, 2002), snow avalanching (Abdelrazek et al., 2014), and gravity granular rapid flow (Abdelrazek et al., 2015; 2016). In SPH method, each particle in the domain carries all field variable information such as density, pressure, velocity and it moves with the material velocity. The governing equations in the form of partial differential equations are converted to the particle equations of motion, and then they are solved by a suitable numerical scheme.

In this study, the advantages of SPH-based SWE model will be exploited to simulate the laboratory observations of the Okushiri tsunami. This tsunami was caused by a large earthquake that occurred in Japan Sea (Hokkaido Nansei-Oki earthquake) on 12th July 1993. Most of the damage was concentrated around Okushiri Island, located west of Hokkaido.

2 SPH SIMULATION METHOD

The SPH method is a continuum-scale numerical method. The material properties $f(x)$, at any point x in the simulation domain were calculated according to an interpolation theory over its neighboring particles which were within its influence domain ***Ω*** as shown in Figure 1, through the following formula:

$$\langle f(x)\rangle = \int_{\Omega} f(x')W(x-x',h)dx' \qquad [1]$$

where h is the smoothing length defining the inflence domain of the kernel estimate and $W(x-x',h)$ is the smoothing function, which must satisfy three conditions (Liu and Liu, 2003): the first condition is the normalization:

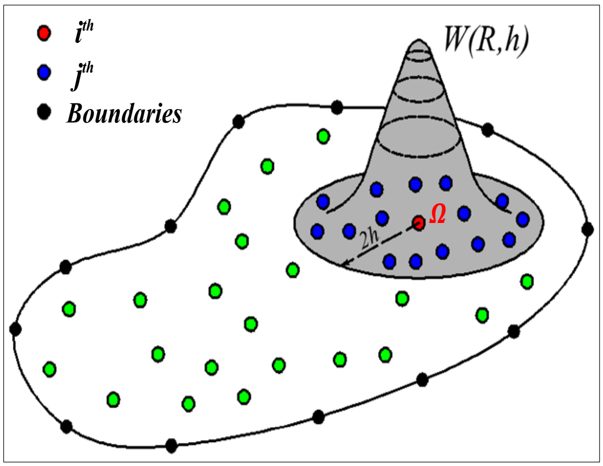

Figure 1. Particle approximation based on kernel function W in influence domain ***Ω*** with radius kh.

$$\int_{\Omega} \mathrm{W(x-x',h)dx'} = 1 \qquad [2]$$

the second one is the Delta function condition:

$$\lim_{h\to 0} W(x-x',h) = \delta(x-x') \qquad [3]$$

and the third condition is the compact condition:

$$W(x-x',h) = 0 \quad \text{when } |x-x'| > kh \qquad [4]$$

where k is a constant depending on the type of smoothing function. There are many possible types of smoothing functions, which can satisfy the aforementioned conditions. The most known function, among them, is the cubic spline interpolation function, and the Quantic Wendland kernel. In this study, we used the Quantic Wendland kernel function which was proposed by Wendland, (1995), and it is defined as:

$$W(R,h) = \alpha_d\left(1-\frac{R}{2}\right)^4 (2R+1) \quad 0 \le R \le 2 \qquad [5]$$

where $\alpha_d = \frac{7}{4\pi h^2}$ in 2D space, and $R = \frac{(x-x')}{h}$.

In the SPH method, the calculation domain is represented by a finite number of particles, which carry mass and the field variable information such as density, stress, etc. (Liu and Liu, 2003). Accordingly, the continuous integral representation for $f(x)$ is approximated in the following form:

$$\langle f(x)\rangle = \int_{\Omega} f(x')W(x-x',h)dx' \approx \sum_{j=1}^{N} f(x_j)\, W(x-x',h)\frac{m_j}{\rho_j} \qquad [6]$$

Using Eq [6], the approximation function of each particle *i* can be written as:

$$\langle f(x_i)\rangle = \sum_{j=1}^{N} \frac{m_j}{\rho_j} f(x_j)\, W_{ij} \qquad [7]$$

where $W_{ij} = W(x - x', h)$

Eq. [7] states that the value of the function at particle *i* is approximated using a weighted average of those values of the function at all other particles in the influence domain of particle *i*. Following the same argument, the particle approximation of the spatial derivative of a function at any particle *i* is:

$$\langle \nabla . f(x_i)\rangle = \sum_{j=1}^{N} \frac{m_j}{\rho_j} f(x_j)\, \nabla_i W_{ij} \qquad [8]$$

3 SPH-BASED SWE MODEL

The shallow water equations were derived from the Navier-Stokes equations, described the evolution of the liquid surface given by a 2D height field. The Lagrangian form of the shallow-water equation (SWE) can be written as:

$$\frac{Dd}{Dt} = -d\, \nabla . v \qquad [9]$$

$$\frac{Dv}{Dt} = -g\, \nabla(d) + g\, (\nabla b + S_f) \qquad [10]$$

where v is the velocity, d is the water depth, *g* =9.81 m/s^2 is the acceleration due to gravity, b is the bottom elevation and S_f is the bed friction source term, and can be calculated from the following formula:

$$S_f = -\frac{n^2 v\, |v|}{d^{4/3}} \qquad [11]$$

where n is the Manning coefficient.

In order to derive the numerical approximation for SWEs, we follow the variation formulation of the SWEs done by (Rodriguez-Paz and Bonet, 2005). In this formulation, the continuum was considered as a Hamiltonian system of particles and the equations of motion were derived in a Lagrangian frame. In this SPH formalism, each particle *i* represent a column of water with a total mass, m_i. Each particle carries their mass and it is unchanged during the motion; hence, the total mass is exactly conserved (Vacondio et al., 2011).

The SPH approximation for the density of the i^{th} particle ρ_i:

$$\rho_i = \sum_{j=1}^{N} m_j\, W_{ij} \qquad [12]$$

In the SWEs, the density may vary enormously due to the changing water depth; thus, a variable smoothing length h is necessary in order to maintain the accuracy of the solution. In general, h is connected to the density with:

$$h_i = h_0 \left(\frac{\rho_0}{\rho_i}\right)^{1/D_m} \qquad [13]$$

whereρ_0, h_0 are the initial density and smoothing length for the i^{th} particle and D_m is the number of space dimensions. Simple Newton—Raphson iteration is adopted in order to solve this system of two Eq. [12] and [13].

Using the SPH approximation the acceleration of particle I (water column) can be expressed as follows:

$$\frac{Dv_i}{Dt} = -g \sum_{j=1}^{N} V_j\, \nabla_i W_{ij} - -g \sum_{j=1}^{N} \frac{V_j}{d_j} (b_j - b_i) \nabla_i W_{ij} - g \frac{n^2 v\, |u|}{d^{\frac{4}{3}}} \qquad [14]$$

where V_j is the volume of neighboring particle *j*.

The total water depth in the SPH-based SWE was calculated based on the modified formula suggested by Xia et al. (2013):

$$d_i = \sum_{j=1}^{N} V_j W_{ij} - \sum_{j=1}^{N} \frac{V_j}{d_j}(b_j - b_i) W_{ij} \qquad [15]$$

In this study the open boundary condition was considered in the SPH method by removing outgoing particles from the outflow (downstream) buffer zones and addition of new particles into the inflow (or upstream) buffer zones by neglecting the reflection of the open boundary conditions. The variables of the particles in the buffer zones were specified by the characteristic open boundary condition by neglecting the reflection at the OBCs.

4 RESULTS AND DISCUSSIONS

4.1 Model description

The Okushiri tsunami in 1993 produced flooding on the coast near Monai, Japan, and this phenomenon was later reproduced by a physical model built to 1/400 scale with dimensions of 5:448 × 3:402 m in the Central Research Institute of Electric Power Industry (Masafumi and Hiroyoshi, 2001). During the real event, the tsunami generated a very high run-up of 31.7 m (0.079 m in the scale model), which was shown by debris and this caused numerous fatalities.

The experimental data were available until the reflected wave reaches the paddle (22.5 s after the beginning of the experiment). The registered datasets were available at the Third International Workshop on Long-Wave Run-up Models (website:http://isec.nacse.org/workshop/2004_cornell/bmark2.html.), including the bathymetry, gauge positions, and the water surface elevation BCs.

4.2 Numerical simulation

The simulation of the benchmark test was carried out using the proposed SPH model. The Manning coefficient was set as equal to 0.025 $m/s^{1/3}$, and the total number of the fluid particles used in this simulation was 85299 over a Cartesian grid with initial distance equalling 1.4 cm.

Figure 2 shows the water depth maps at different time steps. As shown from the figure, the SPH based model reproduces the drawdown of water levels between the island and the coast before the arrival of the tsunami which caused a partial drying of the ridge behind the island (t = 12 Sec). The tsunami reaches the shore and the shock wave induced by the topography (t = 16 Sec), and the run-up and the reflection of the tsunami wave from the coast almost completely submerged the island (t = 20 Sec).

In our simulation, the maximum run-up was 0.082 m, which corresponds to the value of 32.8 m which almost equals the maximum real tsunami run-up (31.7 m).

Figure 3 shows a quantitative comparison between the simulation results (SPH simulation) and field measurement as well as the results obtained by Delis et al. (2008) using a state-of-the-art finite-volume scheme in terms of water level elevations at three gauges off the western coast of Okushiri. The model shows a good quantitative agreement with the experiment, both in the water level height during the simulation time.

The results shown in Figure 3 indicated that the SPH-based SWE model and the finite-volume scheme are able to simulate the tsunami process over the complicated topography, also it showed a reasonable agreement in terms of measured levels; in particular, the maximum run-up was predicted well.

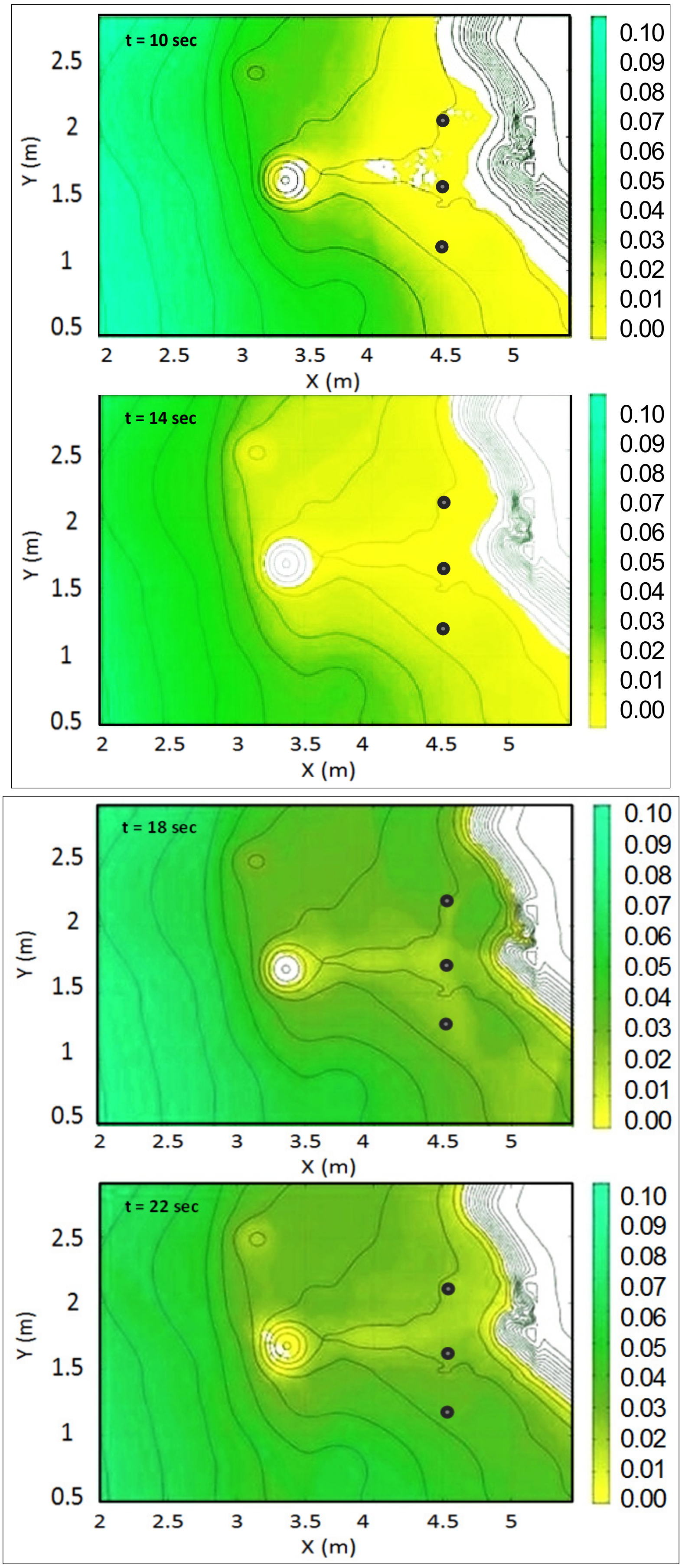

Figure 2. Plan view of total water depths at times 10, 14, 18, and 22 Sec (Black dots mark the locations of three gauges).

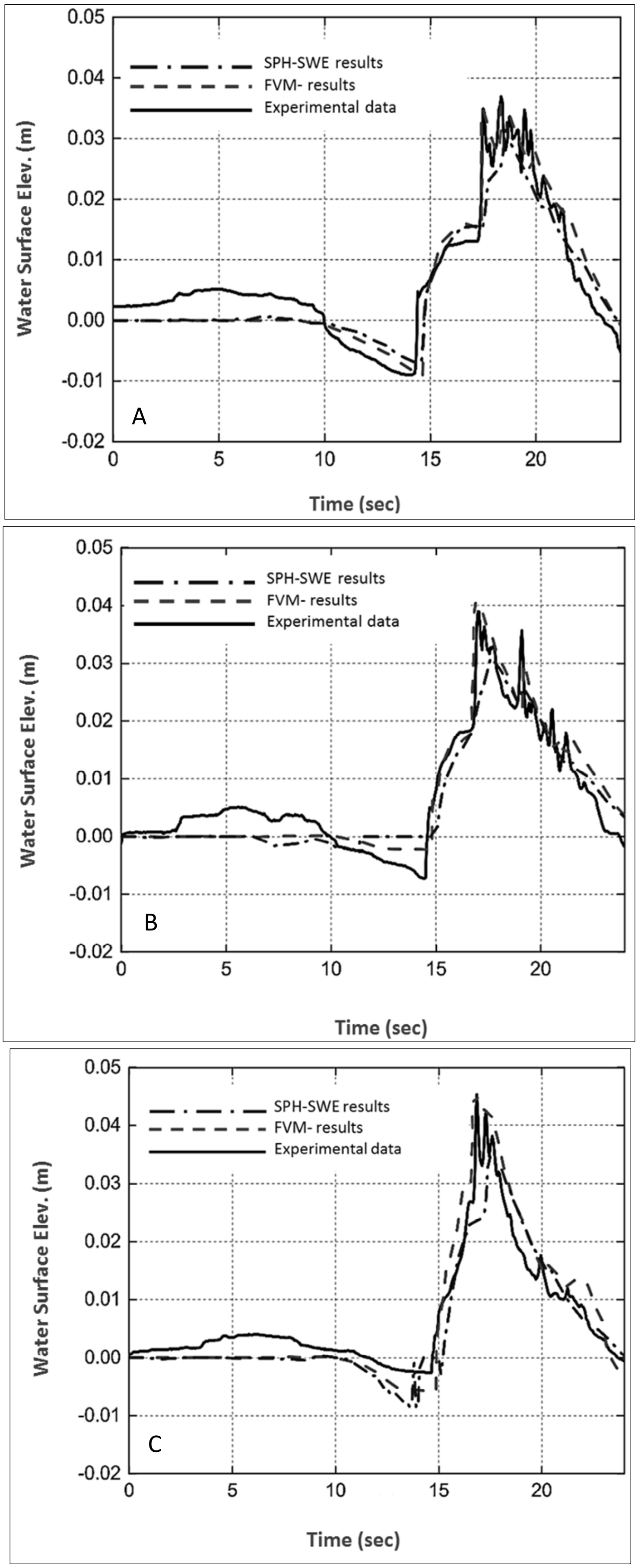

Figure 3. Time series of observed and simulated water level elevations at gauge located at A: (4.521 m, 1.196 m), B: (4.521 m, 1.696 m), and C: (4.521 m, 2.196 m).

5 CONCLUSIONS

The development of an improved smoothed particle hydrodynamics model based on shallow water equation (SWE) to simulate to the laboratory observations of the Okushiri tsunami has been described through this study. The results from these comparisons showed a reasonable agreement with the measured levels without any special treatment in simulating the free-surface flow in regions with complex topography of wetting and drying fronts. Also, the maximum run-up is predicted well. This study demonstrates the capability of the SPH-based SWE model to simulate free surface flows in regions with complicated bathymetry and irregular shoreline.

ACKNOWLEDGEMENTS

This work is supported JSPS KAKENHI Grant Number 15F15369.

REFERENCES

Abdelrazek, A.M., Kimura, I. & Shimizu, Y. (2014). Comparison between SPH and MPS Methods for Numerical Simulations of Free Surface Flow Problems. *Journal of Japan Society of Civil Engineers, Ser. B1 (Hydraulic Engineering)*, 70 (4), 67-72.

Abdelrazek, A.M., Kimura, I. & Shimizu, Y. (2014). Numerical Simulation of Snow Avalanches as a Bingham Fluid Flow Using SPH method. *Proceedings of river flow*, *7th international conference on fluvial hydraulics, Lausanne, Switzerland*, CRC Press, Taylor & Francis Group, 1581–1587.

Abdelrazek, A.M., Kimura, I. & Shimizu, Y. (2014). Numerical Simulation of a Small-Scale Snow Avalanche Tests Using Non-Newtonian SPH Model. *Journal of Japan Society of Civil Engineers, Ser. A2 (Applied Mechanics (AM))*, 70(2), 681-690.

Abdelrazek, A.M., Kimura, I. & Shimizu, Y. (2015). Numerical Simulation of Granular Flow Past Simple Obstacles using the SPH Method. *Journal of Japan Society of Civil Engineers, Ser. B1 (Hydraulic Engineering)*, 71(4), 199-204.

Abdelrazek, A.M., Kimura, I. & Shimizu, Y. (2016). Simulation of Three-Dimensional Rapid Free-Surface Granular Flow Past Different Types of Obstructions using the SPH Method. *Journal of Glaciology*, 62, 335-347.

Cummins, S.J. & Rudman, M. (1999). A SPH Projection Method. *Journal of Computational Physics,* 152, 584–607.

Delis, A. I., Kazolea M. & Kampanis, N. A. (2008) A Robust Highresolution Finite Volume Scheme for the Simulation of Long Waves Over Complex Domains. *International Journal for Numerical Methods Fluids*, 56, 419–452

Gingold, R.A. & Monaghan, J. J. (1977). Smoothed Particle Hydrodynamics: Theory and Application to Nonspherical Stars. *Monthly Notice of the Royal Astronomical Society,* 181, 375–389.

Gotoh, H., Khayyer, A., Ikari, H., Arikawa, T. & Shimosako, K. (2014). On Enhancement of Incompressible SPH Method for Simulation of Violent Sloshing Flows. *Applied Ocean Research*, 46, 104–115.

Libersky, L. D. & Petschek, A.G. (1991). Smoothed Particle Hydrodynamics with Strength of Materials. *In Proceedings of the Next Free Lagrange Conference*, 395, Springer: New York, 248–257.

Liu G.R. & Liu M. B. (2003). *Smoothed Particle Hydrodynamics: a Mesh-Free Particle Method*. World Scientific, 1-472.

Lucy, L. (1977). A Numerical Approach to Testing the Fission Hypothesis. *Astronomical Journal,* 82, 1013–1024.

Masafumi, M. & Hiroyoshi, T. (2001). An Experimental Study of the Highest Run-Up Height in the 1993 Hokkaido Nansei-Oki Earthquake Tsunami. *Proceedings of International Tsunami Symposium; Seattle, U.S.A.,* 879-889.

Monaghan, J.J. (1994). Simulating Free Surface Flows with SPH. *Journal of Computational Physics*, 110, 399–406.

Monaghan, J.J. and Kocharyan, A. (1995). SPH Simulation of Multiphase Flow. *Computer Physics. Communication*, 87, 225-235.

Monaghan, J.J. (2002). SPH Compressible Turbulence. *Monthly Notice of the Royal Astronomical Society*, 335(3), 843-852.

Rodriguez-Paz, M. & Bonet, J. (2005). A Corrected Smooth Particle Hydrodynamics Formulation of the Shallow-Water Equations. *Computer Structure*, 83(17–18), 1396–1410.

Vacondio, R., Rogers, B. D. & Stansby, P. K. (2011). Accurate Particle Splitting for Smoothed Particle Hydrodynamics in Shallow Water with Shock Capturing. *International Journal Numerical Methods Fluids,* 69(8), 1377-1410.

Wendland, H. (1995). Piecewiese Polynomial, Positive Definite and Compactly Supported Radial Functions of Minimal Degree, *Advances in computational* Mathematics, 4 (1), 389- 396.

Xia, X., Q. Liang, M. Pastor, W. Zou & Y. Zhuang. (2013). Balancing the Source Terms in a SPH Model for Solving the Shallow Water Equations. *Advances in Water Resources*, 59, 25–38.